

University of Alberta

LUMINOSITY MEASUREMENT AT THE LARGE HADRON COLLIDER

by

Bryan Lawrence Caron



A thesis submitted to the Faculty of Graduate Studies and Research in partial fulfillment of the requirements for the degree of **Doctor of Philosophy**.

Department of Physics

Edmonton, Alberta
Spring 2006



Library and
Archives Canada

Bibliothèque et
Archives Canada

Published Heritage
Branch

Direction du
Patrimoine de l'édition

395 Wellington Street
Ottawa ON K1A 0N4
Canada

395, rue Wellington
Ottawa ON K1A 0N4
Canada

Your file *Votre référence*
ISBN: 0-494-13944-7
Our file *Notre référence*
ISBN: 0-494-13944-7

NOTICE:

The author has granted a non-exclusive license allowing Library and Archives Canada to reproduce, publish, archive, preserve, conserve, communicate to the public by telecommunication or on the Internet, loan, distribute and sell theses worldwide, for commercial or non-commercial purposes, in microform, paper, electronic and/or any other formats.

The author retains copyright ownership and moral rights in this thesis. Neither the thesis nor substantial extracts from it may be printed or otherwise reproduced without the author's permission.

AVIS:

L'auteur a accordé une licence non exclusive permettant à la Bibliothèque et Archives Canada de reproduire, publier, archiver, sauvegarder, conserver, transmettre au public par télécommunication ou par l'Internet, prêter, distribuer et vendre des thèses partout dans le monde, à des fins commerciales ou autres, sur support microforme, papier, électronique et/ou autres formats.

L'auteur conserve la propriété du droit d'auteur et des droits moraux qui protègent cette thèse. Ni la thèse ni des extraits substantiels de celle-ci ne doivent être imprimés ou autrement reproduits sans son autorisation.

In compliance with the Canadian Privacy Act some supporting forms may have been removed from this thesis.

Conformément à la loi canadienne sur la protection de la vie privée, quelques formulaires secondaires ont été enlevés de cette thèse.

While these forms may be included in the document page count, their removal does not represent any loss of content from the thesis.

Bien que ces formulaires aient inclus dans la pagination, il n'y aura aucun contenu manquant.


Canada

To my family,
for always believing in me even when I didn't.

Abstract

Two novel methods of measuring the luminosity delivered to the ATLAS Experiment at the CERN Large Hadron Collider experiments are presented. The production of $\mu^+\mu^-$ pair via two photon interactions and single W^\pm/Z^0 boson production are evaluated as methods for the measurement and monitoring of the proton-proton luminosity at the LHC.

The characteristics of the $\mu^+\mu^-$ pairs from coherent $\gamma\gamma$ interactions are examined for both matrix element and equivalent photon based monte carlo generators with subsequent simulation of the ATLAS detector effects. The application of specific kinematic and vertex fit requirements is shown to offer a strong method of isolating signal from background and in turn yield an accurate offline measurement of the delivered luminosity via the pure QED process. The choice of kinematic cuts is shown to reduce the overall uncertainty in the method by limiting the size of corrections to the two photon interaction cross section to the level of 1%. Based upon these developed criteria, the results of a first search for the exclusive production of $\mu^+\mu^-$ events from two photon interactions at CDF and the Fermilab Tevatron are presented, providing preliminary evidence for the first observation of two photon process at a hadron collider.

The observation of single gauge boson production is also reviewed as a promising method for online luminosity monitoring at the LHC. The theoretical and experimental considerations are examined. Event selection criteria, efficiencies and rates are outlined based upon the trigger conditions of the

ATLAS experiment. The combined effect of recent theoretical developments in the computation of higher order QCD corrections and parton distribution function (PDF) error sets are incorporated into simulation studies performed for the LHC. An implementation of new PDF reweighting method by which it is possible to calculate the effective uncertainty on physically measurable quantities, without requiring the repeated simulation of identical events with separate PDF error sets as input, is described. The error in acceptance for the observation of $Z^0 \rightarrow e^+e^-$ due to the most recent CTEQ PDF error set is shown to be less than 1%.

Acknowledgements

First I would like to thank my thesis supervisor Professor James Pinfold for his continued support and enthusiasm for the work presented here. I would also like to specifically thank the members of my thesis advisory and examination committees, Dr. Vincent Hedberg, Dr. Faqir Khanna, Dr. John Macdonald, Dr. Sharon Morsink, Dr. Lorenz Sigurdson, and Dr. Richard Sydora for their ongoing support of my research and naturally for the review of the thesis document itself.

I would like to thank Dr. Doug Gingrich and the rest of the CSR faculty and staff for a great work environment. It is never a dull moment. Thanks especially go to Audrey Schapmann, Suzette Chan and Viola Kuhn for keeping the CSR running on a day to day basis while the thesis and other work come and go. The same thanks go to Jim Mackinnon and Jay Haverstock from the Physics department who look after the computing and have been with me on the 'SysAdmin' team that helped with the wide variety of computing issues (both good and bad) that come up over the years.

I would like to thank the members of the ATLAS Standard Model Working Group and the ATLAS Luminosity Working Group for their constructive feedback regarding the thesis work. In particular kudos go to Maarten Boonekamp, Stefan Tapprogge, Joey Huston, Peter Loch and Michael Dittmar who over the years have either knowingly or unknowingly given great suggestions and taught me a lot about physics. Other ATLAS folk that I would like to thank include Marc Dobson and Catalin Meirosu.

I certainly have to thank my CDF colleagues for their helping me learn once again what it means to be part of an experiment that is collecting data. Thanks to Andrew Hamilton for being the man on the ground at Fermilab, as well as to Mike Albrow for his continuous feedback of the work we are doing.

I know I've missed many people off the above list that deserve to be included but to thank everyone who deserves credit would mean a whole bunch more pages that you would never read. So in the end, you know who you are!

Finally, more than anyone else I would like to thank my family. Anastasia, Jordan and Fiona, along with my parents Mary and Rejean, have put up with me over the many years that I've spent working on this thesis and so many other projects. They have always been there for me and I'll never forget that. I love you.

Contents

1	Introduction	1
2	The Large Hadron Collider and the ATLAS Experiment	3
2.1	The Standard Model of Particle Physics	3
2.2	The Large Hadron Collider	5
2.3	The ATLAS Experiment	8
2.3.1	Inner Detector	9
2.3.2	Calorimetry	12
2.3.3	Muon Spectrometer	16
2.3.4	Trigger and Data Acquisition	19
2.3.5	ATLAS Computing Model	21
2.4	Physics at the LHC and ATLAS	22
3	Luminosity Measurement at Hadron Colliders	25
3.1	Luminosity Measurement using Dedicated Running Scenarios .	26
3.1.1	van der Meer method	26
3.1.2	Elastic Scattering	27
3.2	Beam Instrumentation for Luminosity Determination	28
3.2.1	Beam Luminosity Monitors	28
3.2.2	Dedicated sub-detectors	29
3.3	Dedicated Experiment Sub-detectors for In-situ Luminosity Mea- surement	30
3.3.1	CDF Run II Cherenkov Luminosity Monitor	30
3.3.2	D0 Run II Luminosity Monitor	31
3.3.3	ATLAS LUCID detector	31
4	Physics Processes for Luminosity Monitoring at the LHC	34
4.1	Two Photon Interactions at Hadron Colliders	34
4.1.1	Theoretical Models	35
4.1.2	Monte Carlo Simulations	40
4.2	Single Gauge Boson Production at the LHC	41
4.2.1	Parton Distribution Functions	44
4.2.2	Monte Carlo generators	48

5	Luminosity Measurement via Two Photon Interactions	53
5.1	Muon pair production	53
5.1.1	Event characteristics	53
5.1.2	Trigger Definitions and efficiencies	54
5.1.3	Event selection, efficiency, and rate	57
5.1.4	Background Identification and Estimation	64
5.1.5	Absolute Luminosity calculation and uncertainty	70
5.2	Electron pair production	72
6	Two Photon Interactions at CDF	74
6.1	The Tevatron	74
6.1.1	The CDF Detector	77
6.2	Search for Two Photon Production of Exclusive $\mu^+\mu^-$ Events	84
6.2.1	Simulation Results	85
6.2.2	Data Results	91
6.3	Electron pair production	101
7	Luminosity Measurement and Monitoring via Single Gauge Boson Production	107
7.1	W and Z Production	108
7.1.1	Trigger Criteria and Event Selection	108
7.1.2	Operational Considerations	110
7.1.3	PDF Errors and W/Z Production beyond Leading Order	111
7.1.4	The PDF Reweighting Technique	116
7.1.5	Simulation Results with PDF Reweighting	123
8	Conclusion	131
	Bibliography	136

List of Tables

2.1	Fundamental fermions of the Standard Model.	4
2.2	Fundamental bosons of the Standard Model.	4
2.3	Design parameters of the LHC accelerator system.	8
2.4	Inner Detector components and their corresponding typical measurement resolutions.	12
4.1	Available PDF error sets and their associated number of eigenvectors and $\Delta\chi^2$ from the Hessian approach.	46
5.1	Efficiency of the ATLAS Level-1 muon trigger at the low p_T threshold of 6 GeV/c for various regions of coverage.	55
5.2	General kinematic selection criteria applied for the selection of $\mu^+\mu^-$ pairs from two photon interactions at the LHC.	58
5.3	Expected cross sections at the LHC for two photon production of $\mu^+\mu^-$ pairs as well as several background processes, for the application of loose initial kinematic selection criteria.	68
5.4	Signal and background after the application of kinematic and vertex cuts.	70
5.5	Signal and background cross sections from LPAIR after the application of the cut requiring $p_T(\mu^+\mu^-) < 50$ MeV/c so as to appropriately neglect the rescattering correction.	71
6.1	Accelerator parameters of the Fermilab Tevatron.	77
6.2	Measured energy resolutions for the electromagnetic and hadronic calorimetry system of CDF.	80
6.3	Trigger conditions applied in order to produce the <i>gdf0d</i> dataset.	91
7.1	ATLAS Level 1 and 2 trigger definitions implemented for the selection of W^\pm and Z^0 events at the LHC. The symbols MU and EM represent muon and electromagnetic objects, respectively, with the following number indicative of the p_T threshold for the Level 1 trigger. At Level-2 EM objects can be further refined into electron (e) objects. The symbols I(i) indicate a requirement of isolation around the object.	108
7.2	Predicted rates for the observation of W^\pm and Z^0 events at the LHC which survive the selection cuts.	110

7.3	Method by which the errors in acceptance uncertainty are calculated for each of the error PDF sets.	125
-----	---	-----

List of Figures

2.1	Schematic of the CERN LHC and injector accelerator system.	6
2.2	Layout of the LHC underground areas including the experimental halls and service access points.	6
2.3	Photograph of the LHC dipole magnet cryostat.	7
2.4	3-Dimensional cut-out view of the ATLAS detector.	10
2.5	3-Dimensional view of the ATLAS Inner detector system.	11
2.6	3-Dimensional cut-out view of the ATLAS Calorimeter system which is approximately 13.3 m in length and 8.5 m in height.	13
2.7	Readout granularity for each sampling layer of the barrel EM calorimeter.	15
2.8	3-Dimensional view of the ATLAS Muon spectrometer system.	18
2.9	Schematic of the ATLAS Trigger and data collection system.	19
2.10	Schematic of the LHC Computing Grid (LCG) tiered structure.	23
2.11	The ATLAS Canada computing model.	23
3.1	Schematic representation of the crossing colliding beams for luminosity measurement using the van der Meer method.	27
3.2	Example distribution of the observed rate in a beam monitor during luminosity measurement using the van der Meer method.	28
3.3	Beam luminosity figure.	29
3.4	Schematic of a possible secondary emission counter luminosity monitor at the LHC.	29
3.5	Photograph of one module of the CDF Run II Cherenkov Luminosity Counter monitor.	30
3.6	Schematic view of the D0 Run II luminosity monitor.	31
3.7	3-Dimensional view the location of LUCID relative to the ATLAS endcap region and the associated shielding in that region.	32
3.8	Cutaway view of the location of LUCID and the associated support cone around the LHC beampipe.	33
4.1	Effective two photon luminosities at the LHC and LEP for different ion species including pp collisions as a function of the two photon invariant mass.	36
4.2	Feynman diagrams for the production of a) elastic, b) semi-inelastic, and c) fully inelastic lepton pair production via two photon collisions at the LHC.	40

4.3	Feynman diagram for inelastic proton-proton rescattering effects during lepton pair production via two photon collisions at the LHC.	40
4.4	Feynman diagram for lepton pair production from double pomeron exchange as simulated with DPEMC.	41
4.5	Feynman diagrams for the production of W and Z bosons via Drell-Yan at Leading Order QCD.	42
4.6	Cross section for hard scattering, including the production of W and Z , as a function of \sqrt{s} at the Tevatron and LHC.	43
4.7	Kinematic map of Q^2 as a function of x for the production of a particle of mass M at rapidity Y at the LHC.	45
4.8	Hessian method description.	47
4.9	Plot of the CTEQ61E PDF error set distributions for each parton at $Q^2 = 10^4 \text{ GeV}^2$ (top) and the corresponding percentage uncertainty relative to the best fit PDF member (bottom).	49
4.10	Plot of the MRST 2001 PDF error set distributions for each parton at $Q^2 = 10^4 \text{ GeV}^2$ (top) and the corresponding percentage uncertainty relative to the best fit PDF member (bottom).	50
4.11	Plot of the Alekhin02 NLO PDF error set distributions for each parton at $Q^2 = 10^4 \text{ GeV}^2$ (top) and the corresponding percentage uncertainty relative to the best fit PDF member (bottom).	51
4.12	Plot of the ZEUS 2005 PDF error set distributions for each parton at $Q^2 = 10^4 \text{ GeV}^2$ (top) and the corresponding percentage uncertainty relative to the best fit PDF member (bottom).	52
5.1	Schematic representation of the ATLAS muon detector system and the measure of the acoplanarity angle ϕ for $\mu^+\mu^-$ pair production at the LHC.	56
5.2	The ATLAS Level-1 muon trigger system.	56
5.3	Cross section as a function of acoplanarity angle ϕ for the muon pair produced from $\gamma\gamma$ interactions in ATLAS. Shown are the distributions for elastic (black), semi-inelastic (blue), and fully inelastic (red) production via LPAIR, and elastic (green) and double pomeron exchange background (pink) from DPEMC.	59
5.4	Two dimensional histogram demonstrating the relative cross sections in the acoplanarity angle ϕ versus transverse momentum ratio parameter space. Shown are the distributions for elastic (red), semi-inelastic (green), and fully inelastic (blue) production via the LPAIR generator.	60
5.5	Cross section as a function of $p_T(\mu^+)/p_T(\mu^-)$ for the muon pair produced from $\gamma\gamma$ interactions in ATLAS. Shown are the distributions for elastic (black), semi-inelastic (blue), and fully inelastic (red) production via LPAIR, and elastic (green) and double pomeron exchange background (pink) from DPEMC.	61

5.6	Scatter plot demonstrating the measured acoplanarity angle ϕ as a function of the ratio $p_T(\mu^+)/p_T(\mu^-)$ measured in ATLAS. Shown are the distributions for elastic (black), semi-inelastic (blue), and fully inelastic (red) production via LPAIR, and elastic (green) and double pomeron exchange background (pink) from DPEMC.	62
5.7	Cross section as a function of the total $\mu^+\mu^-$ pair p_T for the muon pair produced from two photon interactions in ATLAS. Shown are the distributions for elastic (black), semi-inelastic (blue), and fully inelastic (red) production via LPAIR, and elastic (green) and double pomeron exchange background (pink) from DPEMC.	63
5.8	Cross section as a function of $p_T(\mu^+) - p_T(\mu^-)$ for the muon pair produced from $\gamma\gamma$ interactions in ATLAS. Shown are the distributions for elastic (black), semi-inelastic (blue), and fully inelastic (red) production via LPAIR, and elastic (green) and double pomeron exchange background (pink) from DPEMC.	64
5.9	Cross section as a function of $\mu^+\mu^-$ invariant mass from $\gamma\gamma$ interactions in ATLAS. Shown are the distributions for elastic (black), semi-inelastic (blue), and fully inelastic (red) production via LPAIR, and elastic (green) and double pomeron exchange background (pink) from DPEMC.	65
5.10	Cross section as a function of $p_T(\mu^\pm)$ from $\gamma\gamma$ interactions in ATLAS. The distributions are for elastic (black), semi-inelastic (blue), and fully inelastic (red) production via LPAIR, and elastic (green) and double pomeron exchange background (pink) from DPEMC.	66
5.11	Scatter plot demonstrating the degree of correlation between the measured μ^+ and μ^- p_T measured in ATLAS. Shown are the distributions for elastic (black), semi-inelastic (blue), and fully inelastic (red) production via LPAIR, and elastic (green) and double pomeron exchange background (pink) from DPEMC.	67
5.12	Relative cross section as a function of $p_T(\mu^\pm)$ (left) and total $\mu^+\mu^-$ pair p_T (right). Shown are the distributions for the signal elastic (black), and backgrounds from Drell-Yan production of $\mu^+\mu^-$ (red) and $\tau^+\tau^-$ (green) with muonic decays. Only kinematic and no vertex fit criteria have been applied.	68
5.13	Definition of the impact parameter d_0 and Z_0 based upon the track helix parameters.	69
5.14	Cross section as a function of acoplanarity angle ϕ for the muon pair produced from $\gamma\gamma$ interactions in ATLAS requiring $p_T(\mu^+\mu^-) < 0.050$ GeV/c in order to suppress the rescattering correction to the cross section. Shown are the distributions for elastic (black), semi-inelastic (blue), and fully inelastic (red) production via LPAIR.	72

6.1	Schematic representation of the accelerator complex at Fermilab which provides the proton antiproton collisions to the Tevatron experiments CDF and D0.	76
6.2	Cross sectional elevation view of one half of the CDF detector at FNAL. The other half of the detector is mirror symmetric to the shown layout.	78
6.3	Schematic of the CDF tracking system.	79
6.4	Schematic of the CMU chambers at the outer edge of each Central Calorimeter Wedge.	81
6.5	Schematic of the beam shower counter (BSC) locations on the West side of CDF. The BSC arrangement on the East side is mirror symmetric but does not include BSC-4 or the Roman Pots.	82
6.6	Cross section as a function of transverse momentum of the produced muons (top) and invariant mass (bottom) of the $\mu^+\mu^-$ pair from two photon interactions in CDF. Shown are the distributions for elastic (black), semi-inelastic (blue), and fully inelastic (red) events simulated with LPAIR.	87
6.7	Cross section as a function of the acoplanarity angle ϕ (top) and the ratio of the muon transverse momentum values (bottom) from two photon interactions at CDF. Shown are the distributions for elastic (black), semi-inelastic (blue), and fully inelastic (red) events simulated with LPAIR.	88
6.8	Cross section as a function of p_T difference between muons (top) and a scatter plot demonstrating the predicted correlation between the transverse momenta of the produced muons (bottom) from two photon interactions in CDF. Shown are the distributions for elastic (black), semi-inelastic (blue), and fully inelastic (red) events simulated with LPAIR.	89
6.9	Cross section as a function of pair transverse momentum $p_T(\mu^+\mu^-)$ (top) along with the relationship between the acoplanarity angle ϕ and the ratio of the muon transverse momentum (bottom) from two photon interactions in CDF. Shown are the distributions for elastic (black), semi-inelastic (blue), and fully inelastic (red) events simulated with LPAIR.	90
6.10	(Step 1) Reconstructed acoplanarity angle between the two measured muons.	94
6.11	(Step 1) Magnitude of the vector sum of the muon pair transverse momenta.	95
6.12	(Step 1) Reconstructed invariant mass of the observed muon pairs.	95
6.13	(Step 1) Reconstructed acollinearity of the two measured muons. Values of acollinearity near 180 degrees are characteristic of cosmic rays traversing CDF.	96
6.14	(Step 3) Reconstructed invariant mass of the observed muon pairs.	97

6.15	(Step 3) Magnitude of the vector sum of the muon pair transverse momenta.	98
6.16	(Step 3) Reconstructed invariant mass of the observed muon pairs.	98
6.17	(Step 3) Reconstructed acollinearity of the two measured muons. Values of acollinearity near π radians are characteristic of cosmic rays traversing CDF.	99
6.18	Reconstructed invariant mass and width of the di-muon pair around the mass of the J/ψ meson.	99
6.19	(Step 4) Reconstructed acoplanarity angle between the two measured muons for data and simulation.	101
6.20	(Step 4) Magnitude of the vector sum of the muon pair transverse momenta for data and simulation.	102
6.21	(Step 4) Reconstructed invariant mass of the observed muon pairs for data and simulation.	102
6.22	$R\phi$ view transverse to the beam-line (top) and R-Z view (bottom) of a candidate two photon to muon pair event observed at CDF.	103
6.23	$R\phi$ view transverse to the beam-line (top) and R-Z view (bottom) of a candidate two photon to muon pair event observed at CDF.	104
6.24	Distributions of the observed acoplanarity angle (top) and p_T (bottom) of the electron-positron pair from CDF data (dots) and simulation with LPAIR (histogram).	106
7.1	Exponential decay of the colliding beam luminosity at the LHC as a function of the expected beam lifetime τ_{lumi}	111
7.2	Feynman diagrams for the NLO QCD corrections to the production of W and Z bosons.	112
7.3	Feynman diagrams for the NNLO QCD corrections to the production of W and Z bosons.	113
7.4	Predicted cross sections for the production of Z^0 bosons at LO, NLO and NNLO for the LHC. The error bands represent the uncertainties associated with variations in μ_F and μ_R between $M_Z/2$ and $2M_Z$, and significantly reduce at higher orders. . .	114
7.5	W^+ production cross section at the LHC at NLO using the CTEQ6.1 PDF set including the PDF uncertainties (green). .	116
7.6	Fractional difference of the best-fit CTEQ6.1 PDF set from the sum eigenvector set uncertainties as a function of W^+ boson rapidity.	117
7.7	Fractional difference of the best-fit CTEQ6.1 PDF set from each eigenvector set uncertainty as a function of W^+ boson rapidity.	118
7.8	W^- production cross section at the LHC at NLO using the CTEQ6.1 PDF set including the PDF uncertainties (green). .	119

7.9	Fractional difference of the best-fit CTEQ6.1 PDF set from the sum eigenvector set uncertainties as a function of W^- boson rapidity.	120
7.10	Fractional difference of the best-fit CTEQ6.1 PDF set from each eigenvector set uncertainty as a function of W^- boson rapidity.	121
7.11	Z^0 production cross section at the LHC at NLO using the CTEQ6.1 PDF set including the PDF uncertainties (green). .	122
7.12	Fractional difference of the best-fit CTEQ6.1 PDF set from the sum eigenvector set uncertainties as a function of Z^0 boson rapidity.	123
7.13	Fractional difference of the best-fit CTEQ6.1 PDF set from each eigenvector set uncertainty as a function of Z^0 boson rapidity.	124
7.14	Calculated values for the contribution toward the overall PDF weight for each eigenvector set before the application of Z^0 event selection criteria (solid triangle) and after event selection (open square).	127
7.15	Calculated PDF reweighting terms for the acceptance of $Z^0 \rightarrow e^+e^-$ events in ATLAS for each member of the CTEQ6.1 error PDF set.	128
7.16	Distribution of the ATLAS Rome monte carlo sample of $Z^0 \rightarrow e^+e^-$ as a function of e^+ (top) and e^- (bottom) pseudorapidity. The statistical uncertainty introduced by the limited sample size of the dataset is visible from extent of the error bars. . . .	129
7.17	Calculated theoretical positive (up triangle) and negative (down triangle) percentage uncertainties due to PDF reweighting for the ATLAS Rome sample of $Z^0 \rightarrow e^+e^-$ as a function of the e^+ (top) and e^- (bottom) pseudorapidity η	130

List of Symbols

Acronyms

ALICE	A Large Ion Collider Experiment
ADC	Analog to Digital Converter
AOD	Analysis Object Data
ATLAS	A Toroidal LHC Apparatus
BMU	Barrel Muon Detector
BNL	Brookhaven National Laboratory
BSC	Beam Shower Counter
CERN	European Laboratory for Particle Physics
CDF	Collider Detector at Fermilab
CMP	Central Muon Detector Upgrade
CMU	Central Muon Detector
CMS	Compact Muon Solenoid
CMX	Central Muon Extended
CSC	Cathode Strip Chambers
CSR	Centre for Subatomic Research, University of Alberta
CTEQ	Coordinated Theoretical-Experimental Project on QCD
DC	Data Challenge
D0	D Zero Experiment at Fermilab
DPEMC	Double Pomeron Exchange Monte Carlo
EF	Event Filter
EM	Electromagnetic
FCAL	Forward Calorimeter
FNAL	Fermi National Accelerator Laboratory
HEC	Hadronic Endcap Calorimeter
IP	Interaction Point
LAr	Liquid Argon
LCG	LHC Computing Grid
LHAPDF	Les Houches Accord Parton Distribution Functions
LHC	Large Hadron Collider
LO	Leading Order
LUCID	Luminosity Cerenkov Detector
MDT	Muon Drift Tube
MRST	Martin, Roberts, Stirling, and Thorne
NLO	Next Leading Order
NNLO	Next to Next Leading Order

Acronyms

PDF	Parton Distribution Function
PS	Proton Synchrotron
QCD	Quantum Chromodynamics
QED	Quantum Electrodynamics
RHIC	Relativistic Heavy Ion Collider
RMS	Root Mean Square
ROD	Read-Out Driver
ROI	Region Of Interest
RPC	Resistive Plate Chamber
SC	Super Conducting
SCT	Silicon Central Tracker
SUSY	Supersymmetry
TAG	Event tags, short event summaries for event selection
TGC	Thin Gap Chamber
TPHIC	Two Photon generator for Heavy Ion Collisions
TRT	Transition Radiation Tracker

Symbols

A	Amperes (unit of current)
Hz	Unit of frequency (cycles per second)
J	Joules
K	Kelvin
L	integrated Luminosity
L	instantaneous Luminosity
LVL	Level
M	Invariant Mass
MB	MegaBytes
Q	momentum transfer
T	Tesla
W	Watt
Y	rapidity
barn	Unit of cross section equivalent to 10^{-24}cm^{-2}
eV	electron Volt
η	pseudo-rapidity
ϕ	azimuthal or acoplanarity angle
σ	cross section (or resolution)
\sqrt{s}	center of mass collision energy

Chapter 1

Introduction

The luminosity of a collider facility is by definition is a measure of the intensity of an accelerator's colliding beams and indicates the interaction rate per unit cross section. The luminosity can be specified as either an instantaneous or integrated measurement both of which are important to all physics studies and results, as well as the overall accelerator performance. To obtain the experimental cross sections for the observed physics processes an absolute luminosity measure is needed. Relative luminosity monitoring is also necessary in order to determine the partial luminosity for each physics run, once a correspondence to an absolute luminosity for each run can be determined.

In order to take advantage of the high luminosity available at the LHC it is important that the uncertainty in the absolute luminosity measure be known to approximately the same value as the uncertainty expected from the theoretical cross sections. The uncertainties in the cross section predictions are primarily associated with higher-order QCD corrections and the parton distribution functions. In addition to dedicated hardware devices located directly around the collision point or integrated within the detectors themselves, alternative approaches to luminosity measurement include the use of well understood physics processes. In this thesis two such physics processes for luminosity monitoring are described.

First, an overview of lepton pair production from two photon interactions will be given focusing on the observation of a $\mu^+\mu^-$ pairs for proton-proton collisions at the LHC. Potential backgrounds will be discussed along with the

event variables which I have identified as strong measures by which the signal process can be distinguished from the backgrounds. Based upon the predicted cross sections and the developed event selection criteria I have estimated the uncertainty in delivered luminosity for this process at the LHC with a realistic simulation of the ATLAS detector. It will be shown that the $\gamma\gamma \rightarrow \mu^+\mu^-$ process is a viable candidate method to provide an accurate measurement of the delivered luminosity at the LHC.

Subsequently the detailed results of a preliminary search I have performed for the exclusive production of $\mu^+\mu^-$ pairs from two photon interactions at the CDF Run II experiment of the Fermilab Tevatron will be described. The first set of candidate events from this search are used to perform a direct comparison between simulation and data.

Secondly the production of W and Z bosons as a luminosity monitor will be reviewed. The trigger and event selection criteria to be applied at ATLAS will be discussed along with the operational issues which I have identified as necessary considerations when using this process as a real-time monitoring tool. I have incorporated recent parton distribution function (PDF) error sets together with existing numerical codes which calculate higher order QCD corrections, thereby providing a first time view of the combined effects of these calculations upon the predicted rates for W and Z production at the LHC. In particular the method of PDF reweighting which I have implemented will also be discussed in detail. PDF reweighting will be shown as an accurate method by which the uncertainties associated with the various PDF error sets can be translated into uncertainties of physically observable quantities without resorting to the more traditional brute force and time consuming approach of generating separate simulation datasets for each of the available PDF error set members.

Chapter 2

The Large Hadron Collider and the ATLAS Experiment

2.1 The Standard Model of Particle Physics

Within the Standard Model, all matter is composed of spin - 1/2 particles known as fermions. The fermions of the Standard Model are categorized into quarks and leptons, and come in three families. Leptons can interact via the electroweak interaction but not the strong interaction. Quarks can interact via the electroweak and strong interactions.

Although experiments have verified the accuracy of the Standard Model to high precision, it is still unable to answer some fundamental questions in a number of areas. For example, the fundamental question of why there are only three families of quarks and leptons is unanswered. Also, the other fundamental force, gravity, has yet to be incorporated within the Standard Model. Finally, the mechanism by which mass is generated, the Higgs mechanism, has yet to be experimentally verified.

The Standard Model although accurate, has 19 free parameters comprised of 3 gauge coupling constants (g_e, g_w, g_s), 2 parameters of the Higgs potential (m_H, m_W), 9 fermion masses ($m_u, m_d, m_c, m_s, m_b, m_t, m_e, m_\mu, m_\tau$), 3 mixing angles ($\theta_{12}, \theta_{23}, \theta_{13}$) and 1 phase angle δ in the Cabibbo-Kobayashi-Maskawa matrix, and 1 vacuum parameter of QCD (θ_{CP}). The fundamental fermions and bosons of the Standard Model are listed in Tables 2.1 and 2.2, respectively.

The foundations of the Standard Model are based upon the theories of

Fundamental Fermions (Spin-1/2)					
Quarks			Leptons		
Flavour	Charge	Mass [MeV/c ²]	Flavour	Charge	Mass [MeV/c ²]
Up (u)	+2/3	1.5 to 4.5	Electron neutrino (ν_e)	0	$< 1.5 \times 10^{-6}$
Down (d)	-1/3	5 to 8.5	Electron (e^-)	-1	0.511
Charm (c)	+2/3	$1.0 \text{ to } 1.4 \times 10^3$	Muon neutrino (ν_μ)	0	$< 1.9 \times 10^{-4}$
Strange (s)	-1/3	80 to 155	Muon (μ^-)	-1	105.7
Top (t)	+2/3	$170 \text{ to } 179 \times 10^3$	Tau neutrino (ν_τ)	0	< 18.2
Bottom (b)	-1/3	$4.1 \text{ to } 4.4 \times 10^3$	Tau (τ^-)	-1	< 1777.1

Table 2.1: Fundamental fermions of the Standard Model.

Fundamental Bosons (Spin-1)				
Interaction	Name	Gauge Group	Charge	Mass [MeV/c ²]
Electromagnetic	Photon (γ)	U(1)	0	0
Weak	W boson (W)	SU(2)	1	80.4
Weak	Z boson (Z)	SU(2)	0	91.2
Strong	Gluon (g)	SU(3)	0	0

Table 2.2: Fundamental bosons of the Standard Model.

Quantum Electrodynamics (QED), the Electro-weak interactions from the Glashow-Weinberg-Salam model [1–3] and the description of the weak force via the exchange of massive vector bosons, and Quantum Chromodynamics which describes the strong colour field interactions of the quarks. Both QED and QCD are gauge theories. The Standard Model gauge group is the product group $SU_C(3) \times SU_L(2) \times U_Y(1)$ associated with the colour (c), weak and hypercharge (Y) symmetries. The subscript L indicates that the charged weak interaction involves couplings only to the chiral-left handed component of the fermion. Within the Standard Model one or more gauge bosons mediate each of the forces. The $SU_C(3)$ strong force mediated by 8 massless gluons, while the $SU_L(2)$ weak force is mediated by the three massive bosons W^+ , W^- and Z^0 . Finally the $U_Y(1)$ electromagnetic force is mediated by the massless photon. However the gauge bosons must be massless in gauge theories.

Therefore the question arises as to how can the W and Z acquire mass while still satisfying the requirement of local gauge invariance. The Higgs mechanism requires the spontaneous symmetry breaking of the local $SU_L(2) \times U_Y(1)$ gauge

symmetry, and in the process is the mass generation mechanism for the weak gauge bosons and the massive quarks and leptons. The mechanism postulates the existence of a massive scalar particle known as the Higgs boson which has yet to be discovered. The discovery of the Higgs is the principle goal of the Large Hadron Collider (LHC) at CERN.

2.2 The Large Hadron Collider

The Large Hadron Collider (LHC) ring is 27 km in circumference along the border between Switzerland and France and was previously utilized for the LEP (Large Electron Positron) Collider until 2001 [4]. Counter circulating proton beams are accelerated to beam energies of 7 TeV for a centre of mass collision energy of 14 TeV, higher than any other accelerator facility. Figure 2.1 demonstrates the layout of the CERN accelerator complex that generates and progressively accelerates the proton beams to their final energy of 7 TeV.

At the LHC the first collisions of proton-proton beams is expected in 2007, with two high luminosity experiments under construction at Point 1 (ATLAS) and Point 5 (CMS) around the ring. Two further large experiments are under development for Point 2 (ALICE) and Point 8 (LHCb). Figure 2.2 indicates the locations of the access points and experiments around the LHC ring. The ultimate luminosity of the LHC is $2.3 \times 10^{34} \text{ cm}^{-2} \text{ s}^{-1}$ to be delivered to both ATLAS and CMS. The initial first year of operation will be $2 \times 10^{33} \text{ cm}^{-2} \text{ s}^{-1}$. In both cases the lifetime of the proton beams within the main accelerator is expected to be approximately 13 hours, with collisions occurring every 25 ns, as determined by the bunch spacing within the accelerator.

Initially protons are produced and accelerated in the CERN linear accelerators (linacs) to an energy of 50 MeV, and subsequently transferred through the PS (Proton Synchrotron) Booster to 1.4 GeV, PS (Proton Synchrotron) to 26 GeV, and the SPS (Super Proton Synchrotron) to 450 GeV. The proton beams are then injected into the main LHC ring from which point they are accumulated and accelerated to the final beam energy. Table 2.3 summarizes the characteristics of the LHC at full design configuration.

Accelerator chain of CERN (operating or approved projects)

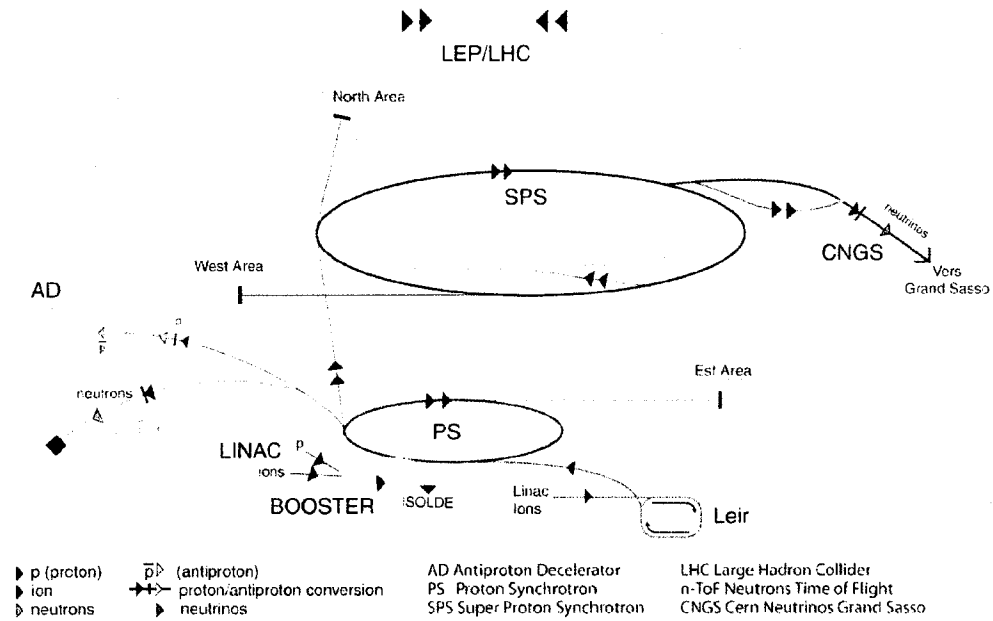


Figure 2.1: Schematic of the CERN LHC and injector accelerator system.

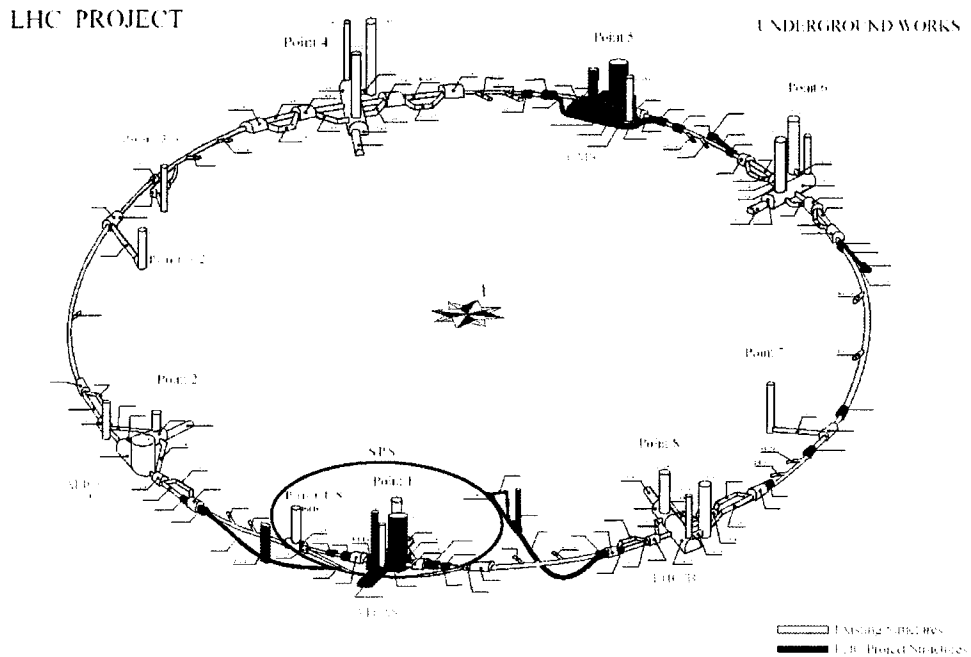


Figure 2.2: Layout of the LHC underground areas including the experimental halls and service access points.

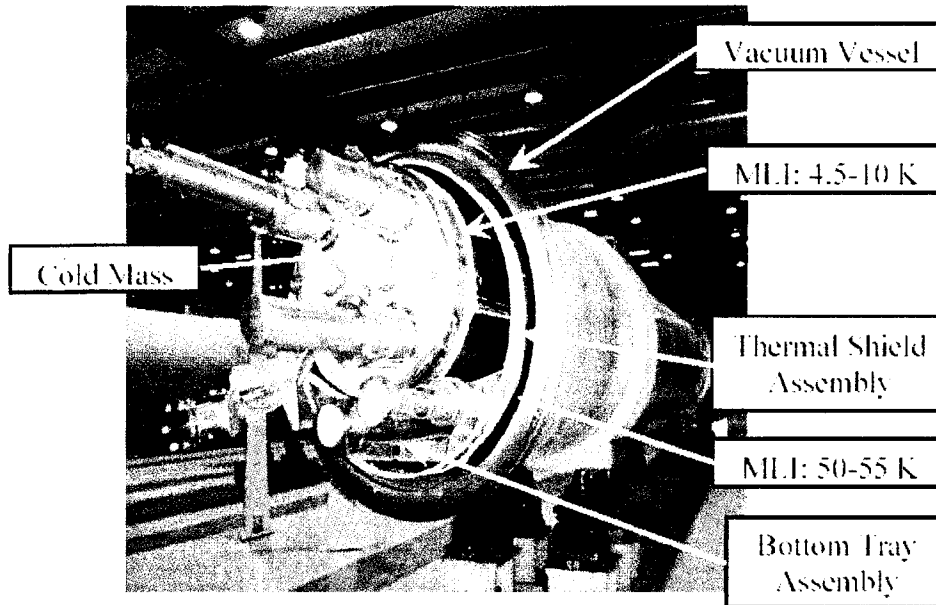


Figure 2.3: Photograph of the LHC dipole magnet cryostat.

The LHC ring consists of 1232 super conducting main dipole magnets (to bend the proton beams) and 392 super conducting quadrupole magnets (to focus the beams). Each of the main dipole magnets is 14.3 m in length with an overall cold mass weight of 23.8 tonnes, providing a field strength of 8.33 T while operating at a temperature of 1.9K. A 400 MHz Radio Frequency (RF) system operating at 16 MV is used to accelerate the proton beams. The dipole magnet cold mass is uniquely designed to accommodate both circulating proton beams within a single common cryostat, thereby saving on the amount of space needed within the LHC tunnel. The dipole magnet cold mass consists of 2 coils per aperture clamped around the cold bores by a common steel collar surrounded by an iron yoke and a shrinking cylinder. Figure 2.3 shows the open end of a LHC dipole magnet. Beam focussing around the LHC ring is achieved by the use of the super conducting quadrupole magnets operating at 1.9 K and providing a peak field strength of 6.86 T. Each of the quadrupole magnets is 3.10 m in length with an overall cold mass weight of 6.5 tonnes.

The LHC and CERN accelerator complex will also be utilized for the acceleration and collision of heavy ions, such as Lead (Pb), to be observed with the

Parameter	Value
Number of experiments	2 high luminosity
Energy	7 TeV
Number of particles per bunch	1.67×10^{11}
Number of bunches	2808
Filling time per ring	4.3 min
Bunch spacing	24.95 ns
Number of long range interactions per experiment	30
Total number of particles	4.7×10^{14}
DC beam current	0.85 A
Stored energy per beam	531 MJ
Maximum transverse beam size in the arc at 7 TeV	0.3 mm
Transverse beam size at IP (r.m.s.) at 7 TeV	$15.9 \mu\text{m}$
Transverse rms beam divergence at IP	$31.7 \mu\text{rad}$
Luminosity	$2.3 \times 10^{34} \text{ cm}^{-2}\text{s}^{-1}$
Events per crossing	44
Total crossing angle	$400 \mu\text{rad}$
Total cross section	100 mbarn
Luminosity lifetime	13.0 hours
Energy loss per turn	7 keV
Total radiated power per beam	5.5 kW
RMS bunch length at 7 TeV	7.55 cm
Relative rms energy spread at 7 TeV	1.129×10^{-4}

Table 2.3: Design parameters of the LHC accelerator system.

ALICE, ATLAS, and CMS experiments. While operating in Pb-Pb collision mode the energy per nucleon will be 2.76 TeV, colliding at a centre of mass energy of 1148 TeV and luminosity of $1 \times 10^{27} \text{ cm}^{-2} \text{ s}^{-1}$. Each ion bunch will be separated by 100 ns yielding an overall beam lifetime of approximately 7.3 hours. The LHC is scheduled to operate in heavy ion mode for 25% of the time, and will provide collisions in excess of 5 times greater than presently available at the RHIC (Relativistic Heavy Ion Collider) facility at BNL (Brookhaven National Laboratory) in Upton, N.Y., United States.

2.3 The ATLAS Experiment

The ATLAS detector is to be situated 100 m underground at Point 1 along the LHC tunnel system. Figure 2.4 presents a 3-dimensional cut-out view of

the ATLAS detector. ATLAS is a multi-purpose detector designed for the observation of proton-proton collisions at the LHC. Heavy ion collisions will also form a portion of the annual running for the LHC facility, and therefore is a further component of the ATLAS physics program. There are over 200 collaborating institutes contributing to ATLAS with over 2000 physicists, scientists and engineers as ATLAS members.

2.3.1 Inner Detector

The ATLAS Inner Detector (ID) combines high-resolution detectors at the inner radii and continuous tracking elements at the outside radii [5–7]. The desired physics performance, in terms of momentum and vertex resolution, dictates that the ATLAS ID system consists of fine-granularity detectors so as to provide high precision measurements. Around the vertex region the highest granularity is achieved using semi-conductor pixel detectors. A straw tube tracker (TRT) at the outer radii provides continuous tracking at a lower cost and material introduced compared to the Pixel and SCT detectors.

Entirely contained within the 2 T central solenoidal magnetic field, the outer radius of the ID cavity is 115 cm with a total length of 7 m. The ID consists of three mechanical units as shown in Figure 2.5: a barrel part extending over ± 80 cm, and two identical end-cap sections providing the remaining coverage. The precision tracking elements of the Pixel and SCT are contained within a radius of 56 cm, surrounded by the continuous tracking segments of the detector. Uniform η coverage is provided over the full detector acceptance by having the final TRT wheels located at high z extend inwards to a lower radius than the other TRT end-cap wheels.

In the barrel region the pixel and SCT detector layers are arranged on concentric cylinders around the beam axis. The endcap detectors are mounted on disks perpendicular to the beam axis. The pixel layers are segmented in $R - \phi$ and z , while the SCT detector uses stereo strips angled at 40 mrad to measure both of these coordinates. One set of strips in each layer of the SCT measures the value of ϕ . The surrounding barrel TRT straws are parallel to the beam direction. Within the endcaps all tracking elements are situated in

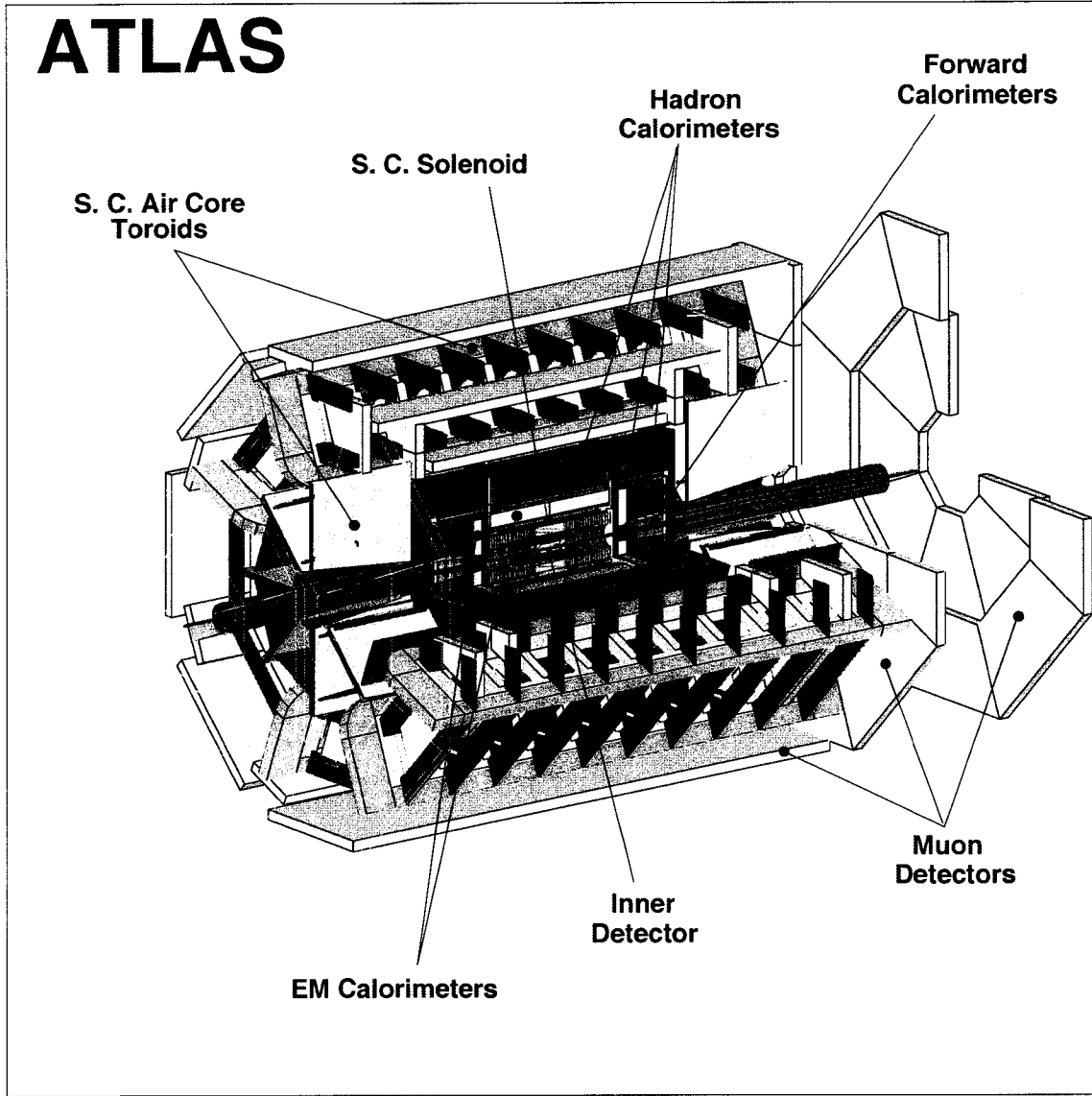


Figure 2.4: 3-Dimensional cut-out view of the ATLAS detector.

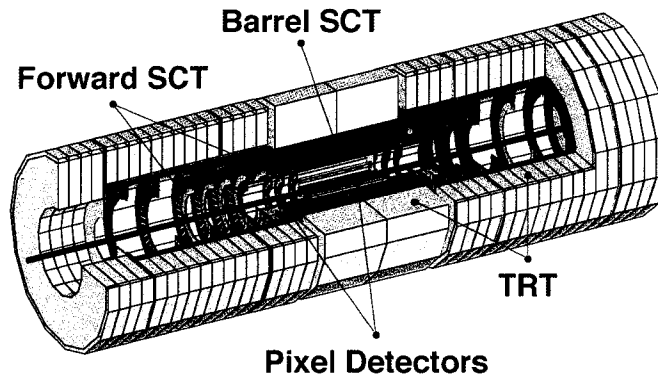


Figure 2.5: 3-Dimensional view of the ATLAS Inner detector system.

planes perpendicular to the beam axis. The continuous tracking elements of the TRT are arranged into wheels consisting of radial straws.

Each track typically traverses three pixel layers and eight strip layers. Subsequent passage through the TRT yields typically 36 space points per track. Together, the two techniques yield robust pattern recognition and position measurement in θ and z coordinates to high precision. This includes impact parameter measurement and vertexing for heavy-flavour quark and τ tagging. The measurement of secondary vertices is enhanced by the innermost layer of pixels, located at a radius of approximately 4 cm, which is as close as practically possible to the beam pipe. Due to the high radiation environment, the mechanical design of the pixel system has been made so as to allow the replacement of the innermost pixel layer over the course of the experiment's lifetime.

System	Position	Area (m ²)	Resolution $\sigma(\mu\text{m})$	Channels (10 ⁶)	coverage $ \eta $
Pixels	1 removable barrel layer	0.2	$R\phi = 12, z = 66$	16	2.5
	2 barrel layers	1.4	$R\phi = 12, z = 66$	81	1.7
	5 end-cap disks per side	0.7	$R\phi = 12, R = 77$	43	1.7 - 2.5
SCT	4 barrel layers	34.4	$R\phi = 16, z = 580$	3.2	1.4
	9 end-cap wheels per side	26.7	$R\phi = 16, R = 580$	3.0	1.4 - 2.5
TRT	axial barrel straws		170 (per straw)	0.1	0.7
	radial end-cap straws		170 (per straw)	0.32	0.7 - 2.5

Table 2.4: Inner Detector components and their corresponding typical measurement resolutions.

2.3.2 Calorimetry

In order to achieve its ambitious physics goals, the ATLAS calorimetry [8,9] was designed with the following performance requirements:

- Jet energy resolution $\frac{\sigma(E)}{E} = \frac{50\%}{\sqrt{E}} \oplus 3\%$ within the central rapidity region $|\eta| < 3$;
- Energy resolution $\frac{\sigma(E_T)}{E_T} < 10\%$ for $E_T > 100$ GeV clusters in the forward region $3 < |\eta| < 5$;
- 1% precision in the measurement of the absolute jet energy scale;
- jet tagging efficiency greater than 90%;
- granularity of $\delta\eta \times \delta\phi = 0.1 \times 0.1$ within the central region, $|\eta| < 3$, adapted to the lateral hadron shower size.

A 3-dimensional view of the calorimeter system is presented in Figure 2.6. Hadron calorimetry is present in the barrel (Hadronic Tile), end-cap (Hadronic Liquid Argon End-cap) and forward (Hadronic Liquid Argon Forward) regions of the detector.

Barrel and End-cap Electromagnetic Calorimeters

The ATLAS electromagnetic calorimeter is a LAr detector with accordion-shaped Kapton electrodes and lead absorber plates. The accordion geometry

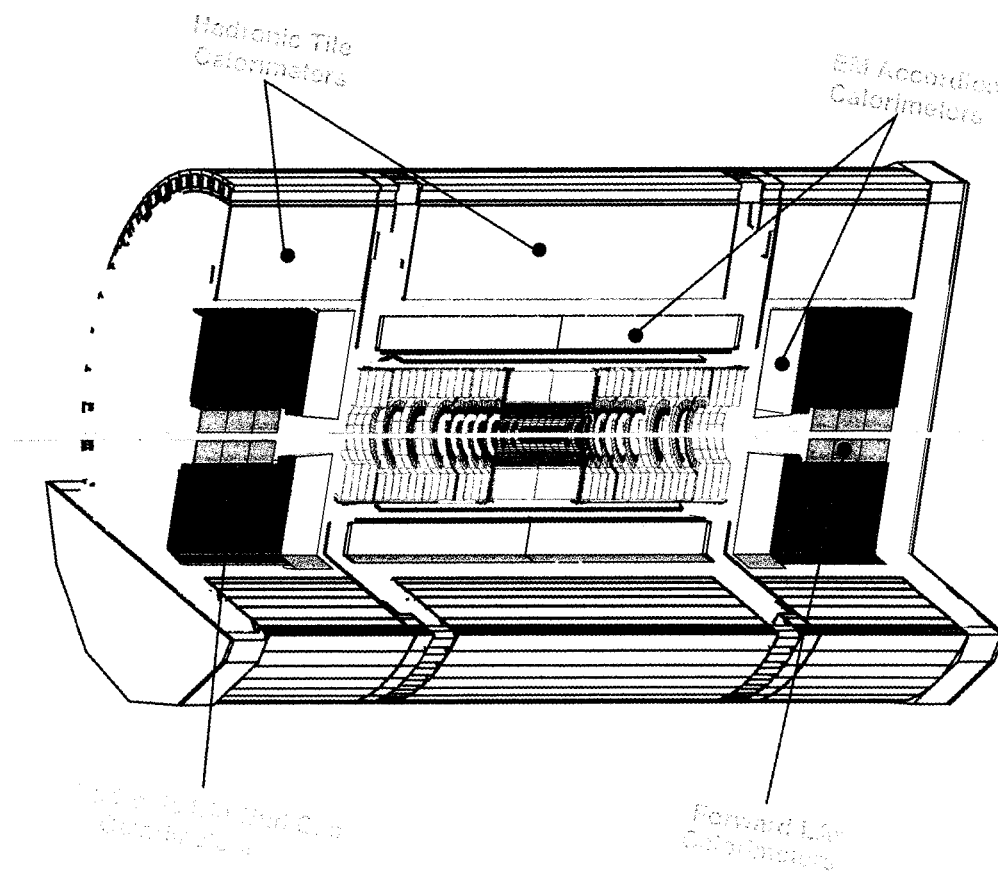


Figure 2.6: 3-Dimensional cut-out view of the ATLAS Calorimeter system which is approximately 13.3 m in length and 8.5 m in height.

provides complete ϕ symmetry without any azimuthal cracks. The thickness of the lead absorber plates has been optimised as a function of η in terms of the measured EM energy resolution performance. The EM calorimeter is divided into both barrel and end-cap regions providing coverage of $|\eta| < 1.475$ and $1.375 < |\eta| < 3.2$, respectively. Within the barrel region the size of the LAr gap is fixed at 2.1 mm. However, within the end-caps the absorbers have constant thickness with an increasing size of LAr gap when moving to larger values of radius. Within $|\eta| < 2.5$ the EM calorimeter contributes to precision physics measurements and is segmented into three longitudinal sections as shown in Figure 2.7. The first layer is the strip section equipped with narrow strips with a pitch of 4 mm in the η direction, approximately 0.0025×0.1 in $\Delta\eta \times \Delta\phi$ in size, that act as a preshower detector and provides precision position measurements in η . The middle sampling is segmented into towers of size $\Delta\eta \times \Delta\phi = 0.025 \times 0.025$. Over the full η coverage the EM calorimeter cells point back toward the interaction region. The signals from the EM calorimeters are extracted at the inner and outer faces of the detector and sent to preamplifiers located outside the LAr cryostat. The total number of EM calorimeter readout channels is approximately 190000.

Hadronic Tile Calorimeter

The Hadronic Tile Calorimeter consists of modules of iron absorber and scintillator tile readout with a granularity of $\Delta\eta \times \Delta\phi = 0.1 \times 0.3$. There are three longitudinal samplings, providing coverage over the region of $|\eta| < 1.7$.

Hadronic Liquid Argon End-cap Calorimeter

The Hadron Liquid Argon (LAr) End-cap Calorimeter consists of copper absorbers arranged in a parallel plate geometry. A total of four longitudinal samplings provide coverage down to $|\eta| < 3.2$. The granularity of the samplings varies with the region of coverage, with $\Delta\eta \times \Delta\phi \approx 0.1 \times 0.1$ within $1.5 < |\eta| < 2.5$, and $\Delta\eta \times \Delta\phi \approx 0.2 \times 0.2$ within $2.5 < |\eta| < 3.2$.

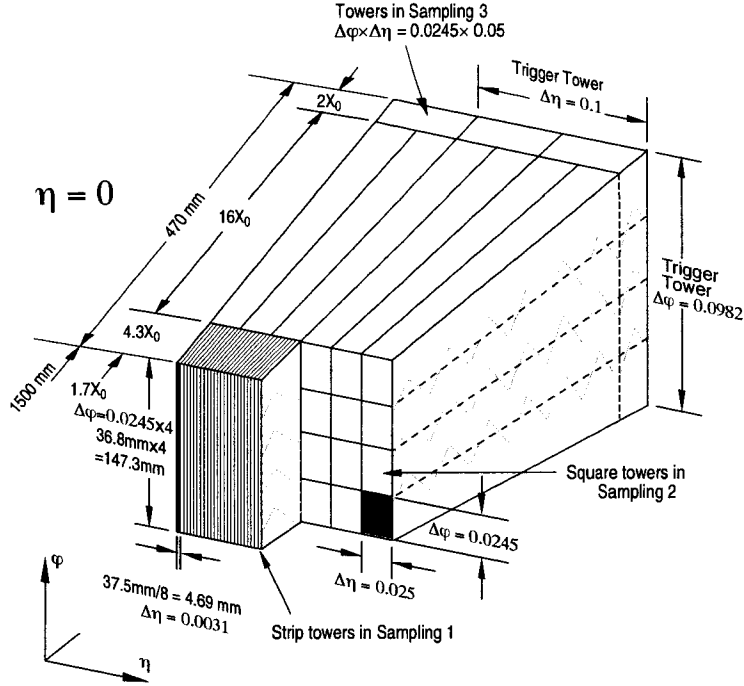


Figure 2.7: Readout granularity for each sampling layer of the barrel EM calorimeter.

Hadronic Liquid Argon Forward Calorimeter

The Hadronic LAr Forward Calorimeter consists of 3 modules. The electromagnetic module is closest to the interaction point and consists of copper absorber. The two remaining hadronic modules use tungsten as the absorber material. The modules are each 28, 91, and 89 radiation lengths in depth and provide nearly 2.7, 3.7, and 3.6 hadronic interaction lengths. The principal coverage provided by the Forward Calorimeter is between $3.1 < |\eta| < 4.9$ with non-projective read-out cells covering an area of approximately $\Delta\eta \times \Delta\phi = 0.2 \times 0.2$. The Forward Calorimeter is fully integrated into the rest of the ATLAS calorimetry system, aiding to minimize any cracks in calorimeter coverage. This is a premium feature for physics measurements with the ATLAS Calorimetry.

2.3.3 Muon Spectrometer

Figure 2.8 provides a three dimensional view of the ATLAS Muon Spectrometer system [10]. Four difference chamber technologies are utilized within the ATLAS Muon Spectrometer system. The chambers are arranged such that particles coming from the interaction point traverse at least three stations of chambers, and the position of the chambers are optimised to provide full coverage and momentum resolution.

In the barrel region the chambers are arranged into three concentric cylinders centered around the beam axis at radii of 5, 7.5 and 10 m and provide coverage over the range of $|\eta| < 1$. A small opening is present in the central $R - \phi$ plane at $\eta = 0$ to allow for the passage of cables and services for the Inner Detector, central solenoid and calorimeters. The inner, middle and outer stations of chambers are arranged into projective towers. Within a given projective tower the chambers are optically connected by alignment rays so as to monitor their relative positions. The endcap chambers provide coverage over the region of $1 < |\eta| < 2.7$ and are arranged into four disks in each endcap at distances of 7, 10, 14 and 21-23 m from the interaction point. For both the barrel and endcaps the chambers are arranged into a 16-fold azimuthal segmentation, matching the eight-fold azimuthal symmetry of the ATLAS magnet structure. Large chamber sectors provide coverage between the barrel toroid coils, while smaller chamber sectors cover the regions directly around the barrel toroid coils.

The Muon Spectrometer trigger is provided by three RPC (Resistive Plate Chamber) stations in the barrel, and three stations of TGCs (Thin Gap Chambers) in the end-cap regions. Precision measurement of the muon tracks through the Spectrometer are provided by the CSC (Cathode Strip Chambers) and MDT (Monitored Drift Tube) chambers.

The MDT chambers consist of aluminium tubes of 30 mm diameter and 400 μm thickness with a 50 μm diameter central W-Re wire. The length of the aluminium tubes varies from 70 to 630 cm. The gas mixture of 93% Ar and 7% CO_2 at an absolute pressure of 3 bar provide for a maximum drift time of

approximately 700 ns and a single-wire resolution of $80\ \mu\text{m}$. In order to achieve a chamber measurement resolution better than the single-wire limit the MDT chambers are constructed from 2×4 and 2×3 monolayers of drift tubes for the inner and middle/outer stations, respectively. Each of the MDT chambers are attached to the spectrometer through kinematic supports and have their position monitored by an in-plane optical measurement system. The CSC are multi-wire proportional chambers with a segmented cathode strip readout providing position measurements with a resolution better than $60\ \mu\text{m}$ from the avalanche formed on the anode wire. The CSC are arranged in 2×4 layers and use a mixture of Ar, CO_2 and CF_4 gas yielding electron drift times of approximately 30 ns and a time resolution of 7 ns.

The RPC is a gaseous detector constructed without wires from two detector layers and four readout strip panels. Both η and ϕ strips parallel and perpendicular to the MDT chamber wires provide two coordinate measurements, and typically provide space and time resolutions of 1 cm and 1 ns, respectively. The narrow gas gap is formed by two parallel resistive bakelite plates separated by 2 mm thick insulating spacers. Operating with a gas mixture of $\text{C}_2\text{H}_2\text{F}_4$ the ionization electrons are multiplied into avalanche mode by a uniform electric field of 4.5 kV/mm.

Finally, the TGCs are similar in design to multiwire proportional chambers except that the anode wire pitch is larger than the anode-cathode separation. The anode wires and readout strips are arranged parallel and orthogonal, respectively, to the MDT wires and provide both spatial and trigger information. The TGCs are operated with a mixture of 55% CO_2 and 45% *n*-pentane in saturation mode enabling the detector to be only slightly sensitive to mechanical deformations while providing short electron drift times and good time resolution. Constructed in sets of two or three chambers, between 4 and 20 anode wires from the TGCs are grouped together to form a trigger signal depending upon the desired granularity as a function of η .

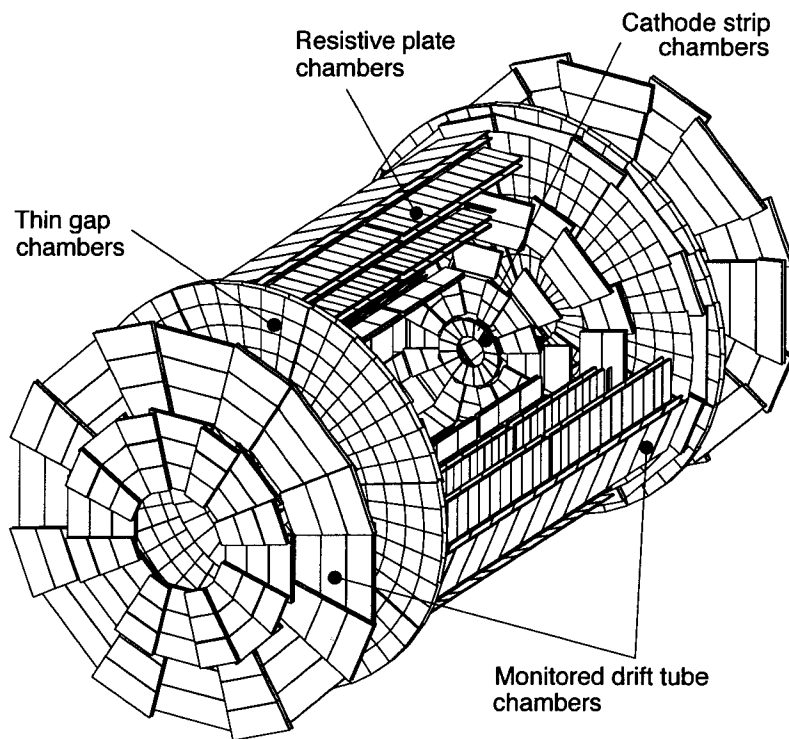


Figure 2.8: 3-Dimensional view of the ATLAS Muon spectrometer system.

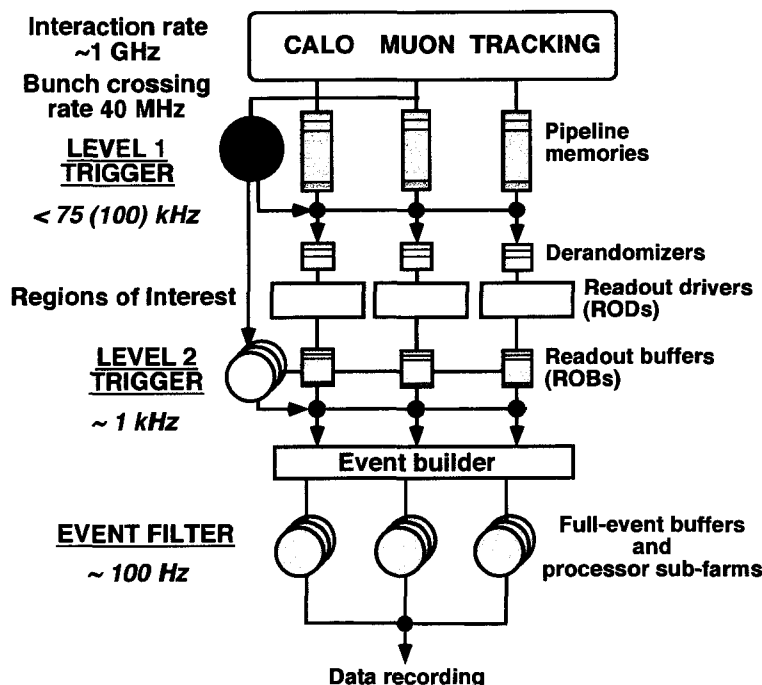


Figure 2.9: Schematic of the ATLAS Trigger and data collection system.

2.3.4 Trigger and Data Acquisition

The ATLAS trigger and Data Acquisition system is based on the three levels of online event selection, where each trigger level refines the decisions made at the previous level, and as needed applies further selection criteria. Figure 2.9 presents a schematic representation of the ATLAS Trigger and data collection system along with the anticipated event rates at the input and output of each stage of the trigger [11, 12].

The Level-1 (LVL1) trigger makes an initial selection using reduced granularity information from a subset of detectors. For example, high p_T muons are identified only using the RPC (barrel) and TGC (end-cap) trigger chambers. The LVL1 trigger is required to uniquely identify the bunch crossing of interest. The latency of the LVL1 trigger is measured as the time from the proton-proton collision until the LVL1 trigger decision is made available to the front-end electronics. The design latency of the LVL1 system is $2.0 \mu\text{s}$. During this latency information from all the detector channels is stored in pipeline memories built from custom integrated circuits and situated close to

the detector. The total number of detector channels exceeds 10^7 .

Once an event has been selected by the LVL1 trigger, all detector channels are readout to readout drivers (RODs) and then into readout buffers (ROBs). All the detector data are stored in the ROBs either until the event is either accepted or rejected the the LVL2. If accepted, the process of moving data from the ROBs to the Event Filter (EF), known as event building, begins. It is at this point the full event is stored in a single memory accessible by an EF processor.

The LVL2 reduces the LVL1 rate from 75 kHz to approximately 1 kHz. The latency of the LVL2 system is variable and expected to be in the range of 1 to 10 ms. The LVL2 trigger makes use of information provided by the LVL1 trigger known as “regions of interest” (RoI). Such RoI information can include the position in (η, ϕ) and p_T of candidate objects, such as high p_T muons, electrons, photons, hadrons, and jets, as well as values for missing E_T vector and scalar sums. Using the RoI information provided by the LVL1 trigger, the LVL2 system selectively accesses data from the ROBs. Additionally, secondary RoIs, typically for low p_T objects, that did not contribute to the selection of the event are also made available to the LVL2 trigger from the LVL1.

The Event Filter (EF) is the third and final stage of the online trigger system and immediately follows the LVL2. The EF will reduced the LVL2 rate by an order of magnitude to approximately 100 to 200 Hz. The EF will employ offline algorithms and methods, specifically adapted for the ATLAS online environment, and utilize the most up to date calibration and alignment information. The EF system has the advantage of being able to running complex analyses on the data which, due to processing time limitations, cannot be executed at LVL2. Such algorithms would include vertex and track fitting using bremsstrahlung recovery for electrons. The final selection of physics events is made by the EF, which subsequently dispatches the events to mass storage for later offline analysis using the full ATLAS software framework. Event sizes are expected to be on the order of 1 to 2 MegaBytes, thereby requiring the use of a mass storage system capable of sustaining in excess of 100 to 200 MegaBytes/second.

2.3.5 ATLAS Computing Model

In order to reconstruct, reprocess and analyse the PetaBytes of data expected from ATLAS it was necessary for the ATLAS Collaboration to develop a distributed Grid-based computing model. The necessity of such a model was based upon the realization that traditional single-site computing and data storage centres would not sufficiently support the broad scope of analysis activities.

The ATLAS computing model is based upon the typical LHC Computing Grid structure of a multi-tiered architecture [13]. Figure 2.10 shows a schematic of the Tier levels associated with the computing model. Successive levels of Data Challenges (DC) have been undertaken within ATLAS since 2000 to develop and test the ATLAS Computing Model in preparation for the commencement of data-taking in 2007 [14].

Distributed globally are a series of Tier-1 facilities which are responsible for the storage of the raw and the associated production of the Event Summary Data (ESD) format corresponding to this raw data. Several times per year the Tier-1 facilities will reprocess the collected raw data samples in order to produce and update the necessary calibration data and subsequently propagate this information in to an offline database that can be accessed by physics groups and individual users. There will be 8 Tier-1 facilities distributed globally for ATLAS, including the Canadian Tier-1 centre based at the TRIUMF laboratory in Vancouver.

Sitting below the Tier-1s are the Tier-2 facilities which within ATLAS are responsible for production of the entire simulation data samples that will be used by the collaboration. It is also at the Tier-2 sites that all access to the Analysis Object Data (AOD) will be provided for both the centrally coordinated physics group activities as well as for individual user analysis. At each of the Tier-2 facilities a large portion of the AOD sample will be available. Furthermore, the entire set of TAG data will be available at each Tier-2.

Typically two Tier-2 centres are each associated with a particular Tier-1 centre. Within Canada Tier-2 facilities have been proposed to be situated

Western and Central Canada, and will provide a number of functions including: the resources to the entire ATLAS collaboration as required by signed Memorandum of Understanding; computing resources and support to Canadian ATLAS physicists for their specific research and analysis needs. Overlaying the Tiered architecture of hardware is a Grid-based computing infrastructure that is under development to provide the necessary resource and data management functionalities to enable ATLAS users to collect and analyse the data.

Within the overall ATLAS computing model individual countries, including Canada, have the flexibility to interface the LHC Computing Grid to their specific multi-purpose multi-user facilities that are in themselves accessible through standard Grid interfaces. For example, Figure 2.11 shows the planned relationship between the LCG and the Grid computing infrastructure at the ATLAS Canada institutes. The end result will be a system that allows the Canadian ATLAS institutes to flexibly provide the necessary computing and storage resources to the collaboration while at the same time enabling Canadian physicists to take leading roles in the analysis of the LHC data.

2.4 Physics at the LHC and ATLAS

The LHC will provide the opportunity for a wide range of physics studies ranging from precision measurements of the Standard Model parameters to the search for the Higgs boson and for physics beyond the Standard Model. The most pressing question is in regards to the origin of mass. In the Standard Model mass is generated via the Higgs mechanism. The result of this mechanism is the production of a particle known as the Higgs boson. Direct and indirect searches at current and previous experiments have excluded the existence of the Higgs below approximately $114 \text{ GeV}/c^2$ [15]. However theory requires that the mass of the Higgs not be greater than $1 \text{ TeV}/c^2$ and as such the entire allowable mass range will be accessible at the LHC.

Another of the major objectives of the LHC is to search for evidence of physics beyond the Standard Model. At present one of the best theoretically motivated sources of beyond the Standard Model physics is supersymmetry. If

LHC Grid

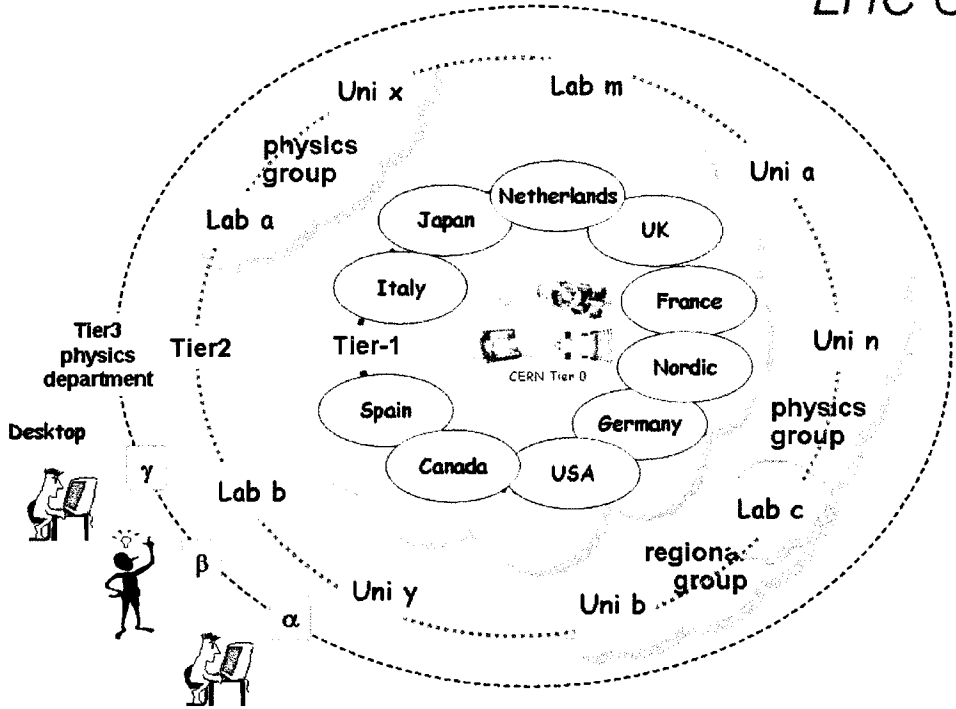


Figure 2.10: Schematic of the LHC Computing Grid (LCG) tiered structure.

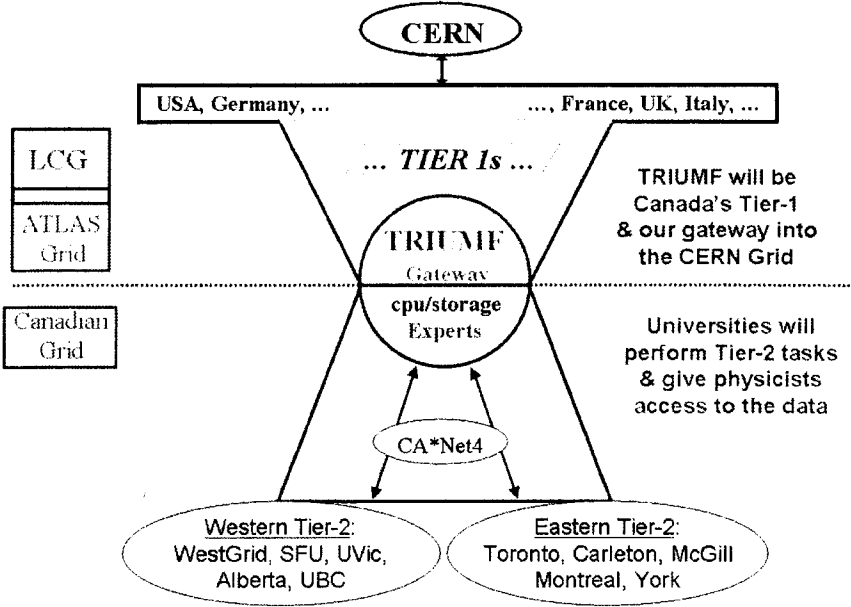


Figure 2.11: The ATLAS Canada computing model.

supersymmetry exists at the electroweak scale then large amounts of squarks and gluinos, as of yet unseen, can be expected at the LHC. Given the kinematic reach available to the LHC, if supersymmetry is found to exist then ATLAS and the LHC experiments will be poised to make precision measurements of the properties of supersymmetric particles.

The LHC will also be an important tool for precision Standard Model physics. Copious amounts of top quark and gauge bosons will be produced at the LHC allowing for the precise mass measurements of the top quark, W and Z . Approximately 8 million $t\bar{t}$ events are expected per year at a luminosity of $10^{33}\text{cm}^{-2}\text{s}^{-1}$, including nearly 300 million single W events. With such large statistics the challenge will be to understand the sources of systematic error that will enable a W mass measurement with a precision less than $20\text{ MeV}/c^2$. Finally, there will be a wide variety of QCD studies that can be carried out at the LHC including precise constraints on the parton distribution functions. A complete description of the physics topics foreseen for ATLAS at the LHC can be found at [16, 17].

Chapter 3

Luminosity Measurement at Hadron Colliders

Luminosity is defined as the intensity of the accelerator colliding beams, or the interaction rate per unit cross section. Both instantaneous and integrated luminosity are values of interest. The absolute luminosity is needed to calculate the experimental cross sections of the observed physics processes. The relative luminosity is needed to be determined for each physics run so as to provide a measure of the absolute luminosity on a run-by-run basis. The accuracy to which the absolute luminosity must be measured in order to take advantage of the LHC is related to the errors associated with the theoretical cross section predictions.

On the timescale for LHC startup in 2007 an overall theoretical error of approximately 5% is estimated taking into account factors such as higher order QCD corrections, parton distribution functions, choice of energy scale, and renormalization scheme. Therefore the goal is to measure the delivered luminosity to an equivalent accuracy of approximately 5%.

It is important to monitor the luminosity over shorter time intervals than available to the absolute luminosity measurement methods. Options include:

- Hodoscopes, constructed from scintillator, at small polar angles to the beam could be used to measure the total non-diffractive cross section. However this is typically appropriate for ≤ 1 interactions per bunch crossing only, and not for the LHC conditions in which the average number of bunch crossings is $\gg 1$. Furthermore, the radiation environment

in the forward region is very harsh, and scintillator material is very susceptible to radiation damage

- Measure event rates in small solid angle sub-detector such that the average number of particles intersecting the detector per bunch crossing is ≤ 1 .
- Monitor the integrated particle flux via the current in an ionization chamber.

Various methods have been deployed at previous and current hadron colliders. A brief discussion of some of the current and future hardware techniques are discussed below.

3.1 Luminosity Measurement using Dedicated Running Scenarios

3.1.1 van der Meer method

The luminosity of a two-ring collider can be described as [18]:

$$L = \frac{I_1 I_2}{c e^2 h_{eff}^2 \tan(\alpha/2)} \quad (3.1)$$

$$h_{eff} = \frac{\int_{-\infty}^{+\infty} \rho_1 dz \int_{-\infty}^{+\infty} \rho_2 dz}{\int_{-\infty}^{+\infty} \rho_1 \rho_2 dz} \quad (3.2)$$

where ρ is the particle distribution in the beam in the plane other than the crossing plane, and α is the beam crossing angle. The currents I_1 I_2 of the circulating beams are accurately measured using beam transformers.

The largest uncertainty comes from the calculation of the transverse beam size at the interaction point. The vertical distance between the centres of the beam distributions at the crossing must be known in order to find h_{eff} .

The van der Meer method requires that the beams are steered vertically with the rate observed in a beam monitor. By constructing a plot of the rate as a function of relative vertical separation h of the two beams, it is then possible to calculate the value of h_{eff} as:

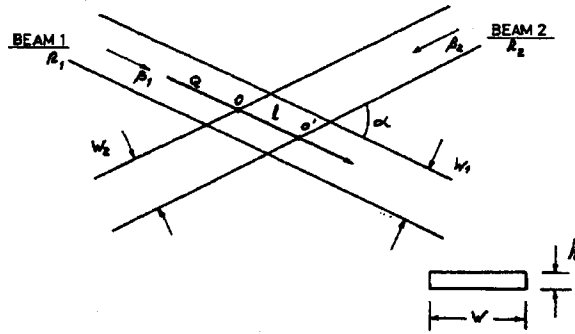


Figure 3.1: Schematic representation of the crossing colliding beams for luminosity measurement using the van der Meer method.

$$h_{eff} = \frac{(\text{Area under the curve})}{(\text{Rate at } h = 0)} \quad (3.3)$$

In order to measure the luminosity with an accuracy of 5% at the LHC using the van der Meer method requires that the height (z) of the beams must be known to an accuracy of approximately $4 \mu\text{m}$. However, the typical resolution of beam position monitors is approximately $16 \mu\text{m}$. Therefore it would be difficult to achieve a luminosity measurement with a precision of better than 5 to 10% using the van der Meer method. Furthermore, the van der Meer method could not be operated at the design luminosity and beam parameters, and would require dedicated runs at luminosities less than $10^{30} \text{cm}^{-2} \text{s}^{-1}$.

3.1.2 Elastic Scattering

It is possible to obtain a measurement of the absolute luminosity via elastic scattering. In this procedure the total cross section is deduced from the simultaneous measurement of the differential cross section $d\sigma/dt$ of elastic scattering at small angles, and the total interaction rate [19]. This procedure requires the use of far forward detectors close to the beam-line to measure the small angle scattering, in conjunction with the existing sub-detectors to provide the total interaction rate. With this method it is difficult to measure the luminosity to a precision much better than 5 to 10%.

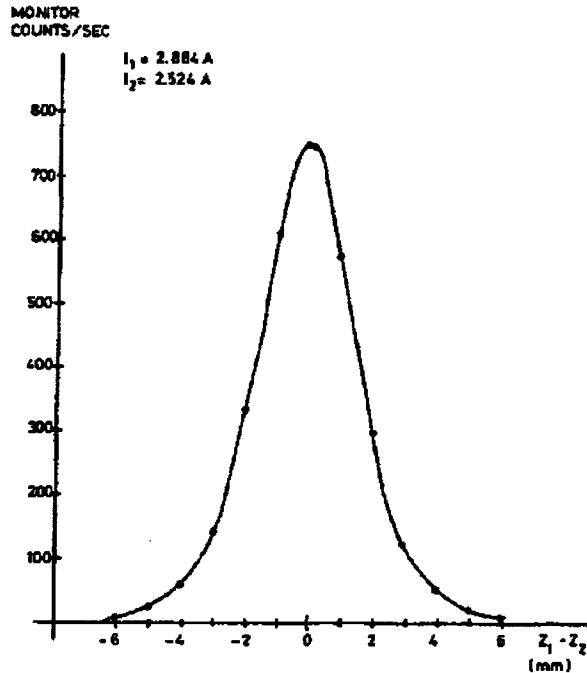


Figure 3.2: Example distribution of the observed rate in a beam monitor during luminosity measurement using the van der Meer method.

3.2 Beam Instrumentation for Luminosity Determination

3.2.1 Beam Luminosity Monitors

The LHC beam luminosity monitor is based on the following principle [20]. The neutrals that originate in LHC at every pp interaction develop showers of minimum ionizing particles in the absorbers placed in front of the separation dipoles. The shower energy, measured by suitable detectors in the absorbers is proportional to the number of neutral particles and, therefore, to the luminosity. The principle lends itself to a luminosity measurement on a bunch-by-bunch basis. However, to make such a measurement feasible, the system must comply with extremely stringent requirements. The speed of the monitor operation must match the 40 MHz bunch repetition rate of LHC. Besides, the detector must be able to withstand extremely high radiation doses.

Figure 3.3: Beam luminosity figure.

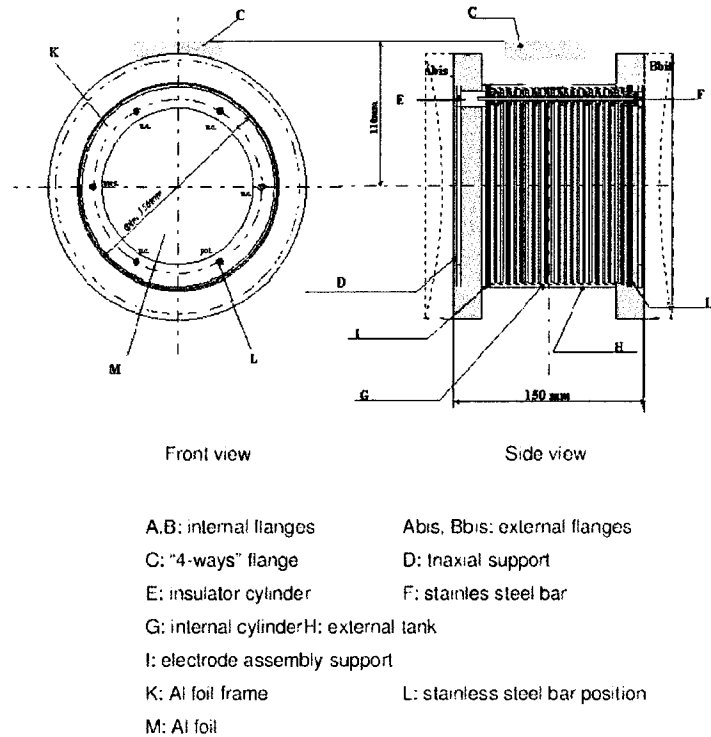


Figure 3.4: Schematic of a possible secondary emission counter luminosity monitor at the LHC.

3.2.2 Dedicated sub-detectors

The Large Hadron Collider (LHC) nominal luminosity is $10^{34} \text{ cm}^{-2}\text{s}^{-1}$, but special runs at $10^{28} \text{ cm}^{-2} \text{ s}^{-1}$ are also foreseen. In order to cover a luminosity dynamic range of six orders of magnitude, a new concept of luminosity monitor shown in Figure 3.4 has been designed based on a double mode detector, working as a secondary emission counter at the highest luminosity and as an ionisation chamber at lower levels [21].

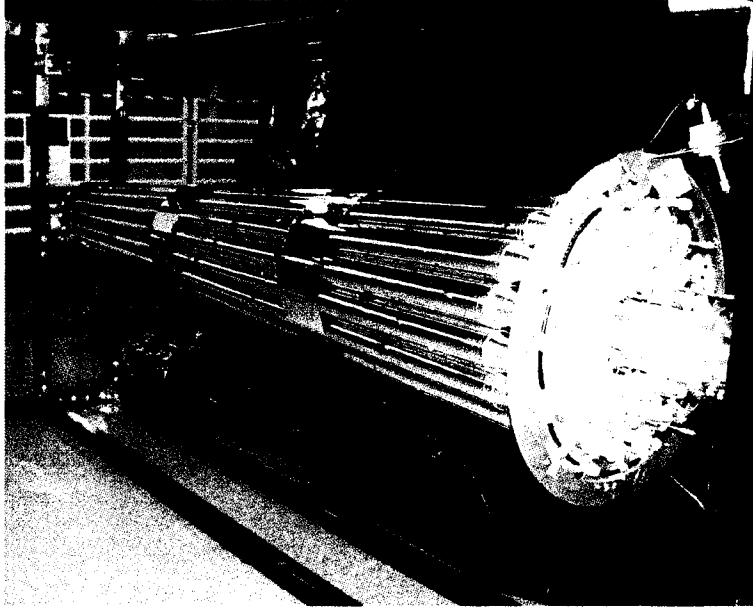


Figure 3.5: Photograph of one module of the CDF Run II Cherenkov Luminosity Counter monitor.

3.3 Dedicated Experiment Sub-detectors for In-situ Luminosity Measurement

3.3.1 CDF Run II Cherenkov Luminosity Monitor

We describe the initial performance of the CLC detector used for the luminosity measurement in the CDF experiment in Run II at the Tevatron [22]. Shown in Figure 3.5 the detector consists of low-mass gaseous Cherenkov counters with high light yield (100 photo-electrons) and monitors the process of inelastic $p\bar{p}$ scattering. It allows for several methods of precise luminosity measurements at peak instantaneous luminosities of $2 \times 10^{32} \text{ cm}^{-2} \text{ s}^{-1}$, corresponding to an average of six $p\bar{p}$ interactions per bunch crossing. With the CLC a linear relationship is observed between the luminosity and the corresponding number of tracks counted in the detector. Furthermore with a time resolution of approximately 140 ps it is possible to follow the collision of bunches in real-time.

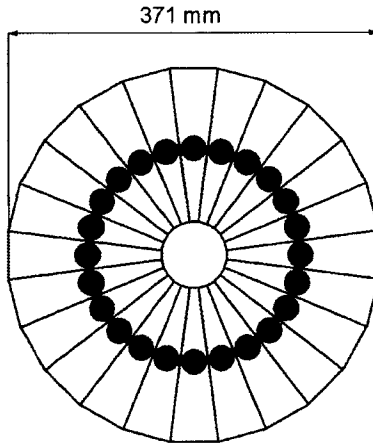


Figure 3.6: Schematic view of the D0 Run II luminosity monitor.

3.3.2 D0 Run II Luminosity Monitor

The D0 Run II Luminosity Monitor consists of plastic scintillation detectors with fine-mesh photomultiplier readout that cover the range $2.7 < |\eta| < 4.4$ in pseudorapidity [23]. A schematic view of the D0 Run II luminosity monitor is shown in Figure 3.6. The detector is designed to provide a precise measurement of the rate for non-diffractive inelastic collisions that is used to calculate the Tevatron luminosity at D0. Excellent time-of-flight resolution allows a clean separation between beam-beam interactions and the principal background from beam halo. In addition, timing is used to measure the position of the primary interaction vertex and to detect multiple interactions. Accurate correction for multiple $p\bar{p}$ interactions in a single beam crossing is essential for an accurate luminosity determination. Associated electronics provide a single-interaction trigger term for the D0 Level 1 trigger, and readout of the photomultiplier timing and pulse-height measurements.

3.3.3 ATLAS LUCID detector

In ATLAS a purpose built luminosity Cherenkov imaging detector named LUCID is planned for installation in 2007 [24]. The technological choices behind LUCID are based upon the successful deployment of the CLC detector at CDF discussed in Section 3.3.1. LUCID will consist of two detectors, one

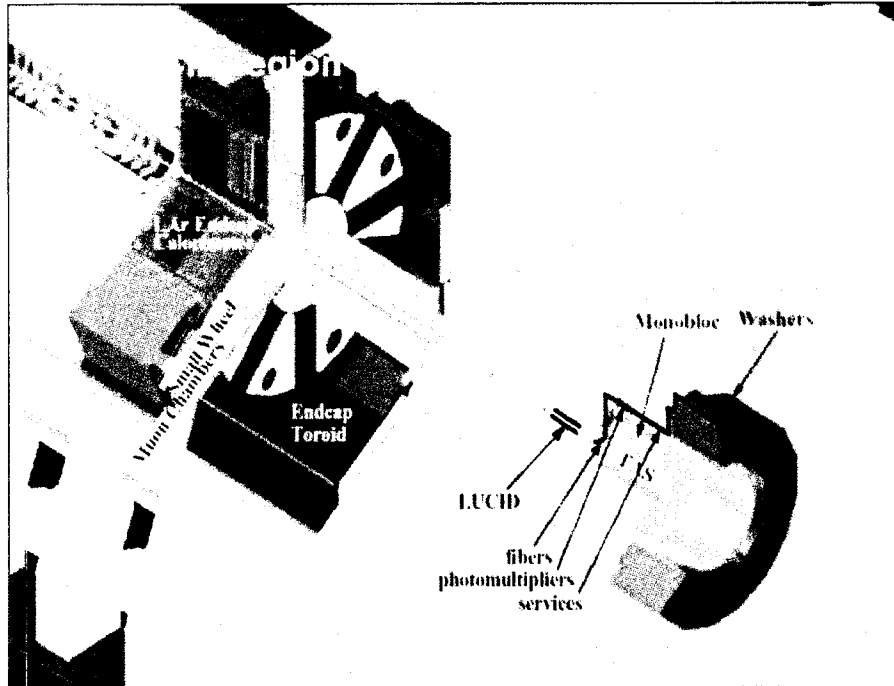


Figure 3.7: 3-Dimensional view the location of LUCID relative to the ATLAS endcap region and the associated shielding in that region.

per endcap of ATLAS, each consisting of 168 Aluminium tubes filled either with C_4F_{10} or Isobutane at a pressure of between 1 and 2 Bar. The tubes are arranged into 4 layers of 42 tubes per layer with a Winston cone at the end of the tubes that transmits the generated Cherenkov light onto a bundle of 7 quartz fibers for each tube that lead to a multi-anode photomultiplier tube installed in the nearby nose shielding. As shown in Figure 3.7 the front-face of each LUCID end is situated approximately 17 m from the interaction point within the forward cylindrical shielding and provides coverage in the range of $5.4 < |\eta| < 6.1$. The expected annual radiation dose within the LUCID region is approximately 7Mrad at the LHC design luminosity of $10^{34} \text{cm}^{-2} \text{s}^{-1}$. In addition to the primary purpose of luminosity measurement, it will also be possible to integrate LUCID with the ATLAS trigger system so as to provide input for a rapidity gap trigger for diffractive physics. A cutaway view of the LUCID detector and the associated support cone structure are shown in Figure 3.8.

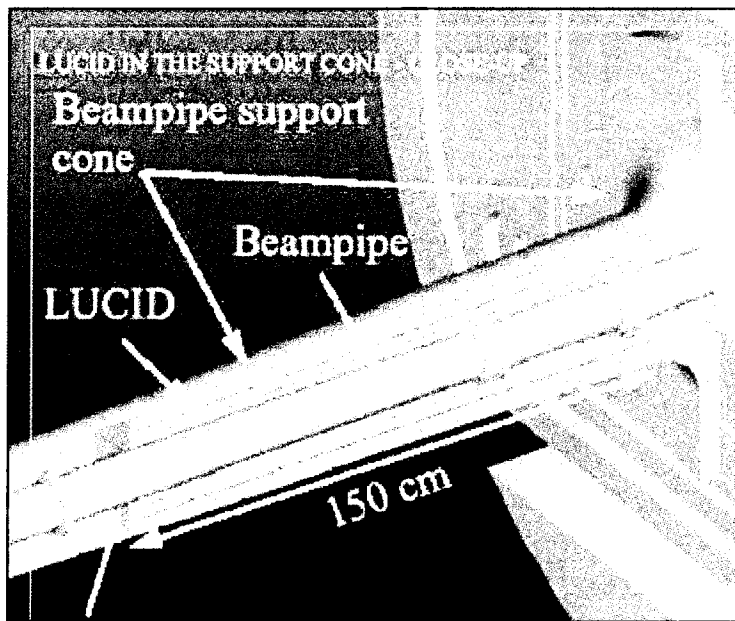


Figure 3.8: Cutaway view of the location of LUCID and the associated support cone around the LHC beampipe.

Chapter 4

Physics Processes for Luminosity Monitoring at the LHC

In order to utilize physics processes as a tool for the measurement of luminosity at the LHC it is necessary for the theoretical description, which underlies the particular physics of interest, to be well understood and to high levels of accuracy. In this chapter the two primary physics processes proposed as luminosity measurement (or monitoring) methods will be reviewed. The processes of two photon interactions at hadron colliders and single gauge boson production at the LHC, provide unique and complimentary methods by which the luminosity delivered to the ATLAS experiment can be measured, in addition to the measurements that will be provided by dedicated purpose-built luminosity measurement detectors.

4.1 Two Photon Interactions at Hadron Colliders

In addition to hard scattering processes that are typically studied at hadron colliders such as the LHC, it is also possible to utilize these facilities as a photon-photon collider. In this situation the collisions are of virtual photons arising from the electromagnetic field of the incoming proton beams. Two methods are typically used to describe the process by which the photons are emitted from the incoming hadron beams, and as such contribute to the over-

all calculation of the cross section of the two photon process. These method are the equivalent photon approximation and the direct matrix element calculation. The exclusive lepton pair production via photon-photon fusion process

$$p(\bar{p}) \rightarrow p + l^+ l^- + \bar{p} \quad (4.1)$$

was proposed as the signature process for a luminosity monitor and was first described in [25].

4.1.1 Theoretical Models

The equivalent photon approximation (EPA) [26,27] can be written as the factorized product of the the equivalent photon flux from each incoming beam times the direct cross section for the two photon collision which produces the lepton pair.

The cross section for the two photon process can be factorized into the $\gamma\gamma$ luminosity function $L_{\gamma\gamma}$ and the cross section of the photon-photon interaction process $\gamma\gamma \rightarrow X_f$.

$$d\sigma = \sigma_{\gamma\gamma \rightarrow l^+ l^-} dn_1 dn_2 \quad (4.2)$$

$$\sigma = \int \frac{dw_1}{w_1} n(w_1) \int \frac{dw_2}{w_2} n(w_2) \sigma_{\gamma\gamma \rightarrow X_f}(\sqrt{4w_1 w_2}) \quad (4.3)$$

$$(4.4)$$

Here $\sigma_{\gamma\gamma}$ is the cross section for the corresponding subprocess, $n(w_i)$ are the equivalent photon spectra from the incoming beams, w_i are the energies of the incoming photon beams and $W = \sqrt{4w_1 w_2}$ is the invariant mass of the outgoing X_f system. A formulation of the equivalent photon flux based upon the semiclassical impact parameter space description of the interaction can be written as [28, 29]

$$n(w) = \frac{2\alpha Z^2}{\pi\xi} \left[\frac{\xi}{\xi_0} K_0\left(\frac{\xi}{\xi_0}\right) K_1\left(\frac{\xi}{\xi_0}\right) - \frac{1}{2} \left(\frac{\xi}{\xi_0}\right)^2 \left(K_1^2\left(\frac{\xi}{\xi_0}\right) - K_0^2\left(\frac{\xi}{\xi_0}\right) \right) \right] \quad (4.5)$$

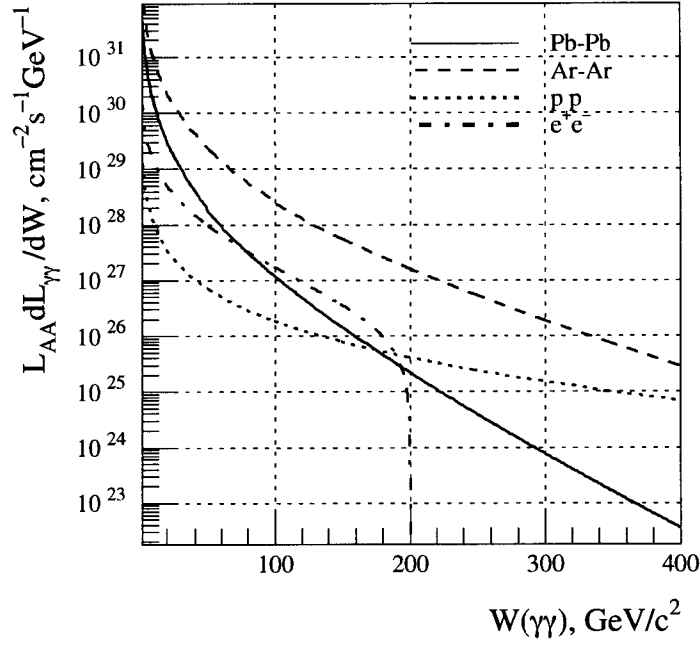


Figure 4.1: Effective two photon luminosities at the LHC and LEP for different ion species including pp collisions as a function of the two photon invariant mass.

where $K_{0,1}(\xi/\xi_0)$ are the Bessel functions, such that $\xi_0 = 1/(RM_N) = wR/\gamma\beta$ and ξ is the fraction of the total momentum of each nucleus carried by the photons. The variables R and M_N represent the radius and the mass of the colliding nuclei, respectively. As indicated there is a squared dependency upon the Z of the ion beam which will enhance the equivalent photon flux for heavy ions compared to strictly proton-proton collisions. Figure 4.1 shows the effective two photon luminosities at the LHC for the collision of different ion species as a function of the two photon invariant mass [26]. The plotted luminosities also take into consideration that the ion-ion luminosity for each heavy ion species is different and several orders of magnitude less than the proton-proton luminosity. The effective two photon luminosities for Ar-Ar is therefore larger than Pb-Pb. Similarly for values of invariant mass greater than $180 \text{ GeV}/c^2$ the two photon luminosity from proton-proton collisions is larger than Pb-Pb.

For the Matrix Element calculation of two photon interactions from collid-

ing lepton beams the differential cross section can be written as [27]

$$dn_{QED} = \frac{\alpha}{\pi} \frac{dw}{w} \frac{dq^2}{q^2} \left(1 - \frac{q_{min}^2}{q^2}\right) = \frac{\alpha}{\pi} \frac{dw}{w} \frac{\mathbf{q}_T^2 d\mathbf{q}_T^2}{\left(\frac{w^2}{\gamma^2} + \mathbf{q}_T^2\right)^2} \quad (4.6)$$

where $q(w, \mathbf{q})$ is the four-momentum of the virtual photon and $\gamma = E/m$ is the Lorentz factor of the colliding particle.

However when the colliding beams are protons (or antiprotons) one must then include the electromagnetic form factors G_E and G_M for the proton.

For purely elastic collisions as illustrated by the Feynman diagram of 4.2 a) we have

$$dn_{elastic} = dn_{QED} \frac{G_E^2 - \frac{q^2}{4m_p^2} G_M^2}{1 - \frac{q^2}{4} m_p^2} \quad (4.7)$$

For the semi-elastic and inelastic collision processes an additional factor needs to be applied for each inelastic vertex yielding

$$dn_{inelastic} = dn_{QED} \frac{W_2(q^2, M^2)}{2m_p} dM^2 \quad (4.8)$$

$$\approx dn_{QED} \frac{|q^2|}{4\pi^2\alpha} \frac{\sigma_T^{\gamma p} + \sigma_S^{\gamma p}}{M^2 - m_p^2} dM^2 \quad (4.9)$$

where M is the invariant mass of the hadronic system, W_2 is the inelastic scattering structure function, $\sigma_T^{\gamma p}$ and $\sigma_S^{\gamma p}$ are the γp cross sections known from photo-production and deep inelastic scattering experiments. The characteristic lepton pair p_T for purely elastic collisions is much less when compared to that for inelastic collisions. Experimentally the observed cross section for two photon production of $\mu^+\mu^-$ pairs can be written as

$$\sigma_{\gamma\gamma}^{pp \rightarrow X + \mu^+\mu^-} = \sigma_{\gamma\gamma}^{elastic} + e_{inel} \sigma_{\gamma\gamma}^{inel} - (1 - e_{rescattering}) \sigma_{\gamma\gamma}^{rescattering} \quad (4.10)$$

The Born amplitude of two photon exchange to produce lepton pairs can be calculated completely within QED. In the final state there are no strong interaction effects between the leptons. However one must consider the size of

the absorptive corrections arising from inelastic proton-proton rescattering as shown in Figure 4.3.

The rescattering corrections are strongly suppressed for two reasons [27]. Firstly, the primary part of the Born cross section comes from the peripheral region with large impact parameter b where the strong amplitude $A(s, b)$ is small. Secondly, in the region of small b the rescattering correction is greatly suppressed due to the angular integration.

In addition to the fully elastic-elastic case, there are the contributions coming from the semi-inelastic and fully inelastic reactions as shown in Figure 4.2 b) and 4.2 c).

$$pp \rightarrow X + l^+l^- + p \quad (4.11)$$

$$pp \rightarrow X + l^+l^- + Y \quad (4.12)$$

where X and Y can be baryon excitations such as the N^* or Δ isobars. While it is possible to calculate the matrix elements for these processes based upon photo-production and deep inelastic scattering experiments, the matrix elements are not known to high accuracy [27]. Therefore the preferred solution is to suppress as much as possible the contributions arising from these processes through the application of suitable experimental cuts.

Inelastic vertices of the type $p \rightarrow X + \gamma$ vanish like q_{1t} as the transverse momentum of the photon q_{1t} approaches zero. Therefore in order to suppress the production of N^* and Δ it is easiest to select events with very small transverse momentum of the lepton pair, typically required to be 10 to 30 MeV. The integral over the transverse momenta of the photons in the Born cross section therefore becomes

$$\int \frac{dq_{1t}^2 dq_{2t}^2 q_{1t}^2 q_{2t}^2}{(q_{1t}^2 + t_1)^2 (q_{2t}^2 + t_2)^2} \delta^{(2)}(p_t - q_{1t} - q_{2t}) d^2 p_t \quad (4.13)$$

The dominant contributions come from the regions where $q_{it} \leq p_t$. Selecting events at the LHC such that the total transverse momentum of the lepton pair is small ($p_t < 30$ MeV for example) then the Born cross section behaves as

$$\frac{d\hat{\sigma}}{dp_t^2} \propto \frac{1}{p_t^2} \ln\left(\frac{p_t^4}{t_1 t_2}\right) \quad (4.14)$$

The excitation processes can also be suppressed by taking advantage of the peak in acoplanarity angle at $\phi = 0$.

Absorptive (re-scattering) Conditions [27]

For the rescattering process schematically shown in Figure 4.3 the calculation proceeds with an extra loop integration over the momentum Q transferred via the strong interaction amplitude represented by the dark region. The strong interaction in this case is not mediated by a point-like object and rather should be viewed as a multiphase or gluon ladder (pomeron) exchange between the protons. Therefore Figure 4.3 is a simplified representation of the underlying process. In the end the total correction to the Born cross section due to rescattering can be computed as $2\delta d\hat{\sigma}/dp_t^2$ where $\hat{\sigma}$ is the cross section for the QED subprocess of two photon scattering through the lepton box. In the assumption of small transverse momentum of the lepton pair, the absorptive correction reduces to

$$\delta \approx \frac{\sigma_{inelastic}}{8\pi} p_t^2 C \quad (4.15)$$

where $\sigma_{inelastic}$ is the total inelastic cross section and C is a numerical coefficient. The calculations of Khoze et al. [27], yield for the production of a $\mu^+\mu^-$ pair of invariant mass 20 GeV yields coefficients C equal to 0.14, 0.13, 0.09 and 0.08 for $p_t = 5, 10, 30$, and 50 MeV, respectively. This results in a negligible correction to the Born cross section due to absorptive effects in the situation of low muon pair transverse momentum. For example the $\mu^+\mu^-$ production with pair transverse momentum p_T of 10(50) MeV/c results in a rescattering correction of

$$2\delta \approx \frac{80\text{mb}}{4\pi} p_t^2 C < 0.02\% \text{ (0.13\%)} \quad (4.16)$$

The end result is that the rescattering correction to the Born cross section does not induce a sharp peak in the lepton pair acoplanarity distribution. As

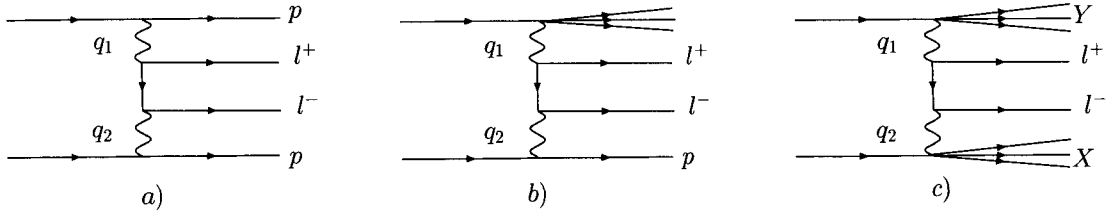


Figure 4.2: Feynman diagrams for the production of a) elastic, b) semi-inelastic, and c) fully inelastic lepton pair production via two photon collisions at the LHC.

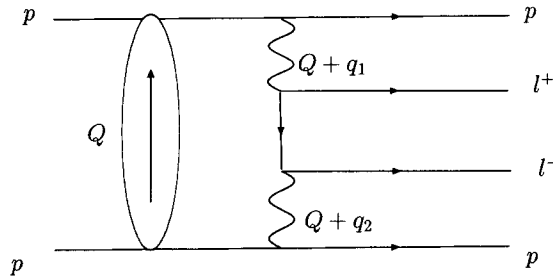


Figure 4.3: Feynman diagram for inelastic proton-proton rescattering effects during lepton pair production via two photon collisions at the LHC.

such a fit of the acoplanarity angle distribution would also be well suited to suppress contributions due to the rescattering correction.

4.1.2 Monte Carlo Simulations

At present there are only a small set of Monte Carlo generators specifically written for the simulation of two photon collisions from incoming hadron beams. These generators can be categorized into the two types of using either the Equivalent Photon Approximation or a full matrix element calculation.

Of the available generators only the LPAIR Monte Carlo [30, 31] performs a full Leading Order matrix element calculation. LPAIR is able to simulate two photon interactions from incoming proton, antiproton or electron/positron beams. In addition to simulating fully elastic collisions, it is also capable of simulating the cases where either one or both of the incoming protons dissociates upon emitting the photon. The corresponding kinematic effect upon the produced lepton pair is calculated according to whether the collision is elastic,

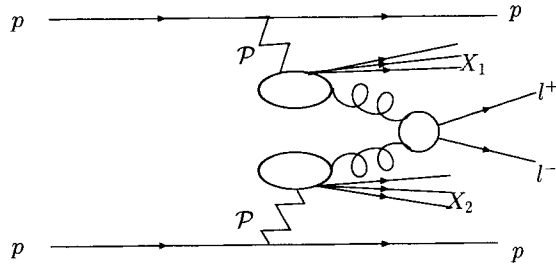


Figure 4.4: Feynman diagram for lepton pair production from double pomeron exchange as simulated with DPEMC.

semi-inelastic or fully inelastic. The dissociation of the (semi-)inelastic proton are however not simulated within LPAIR and are left for other generators to simulate.

The remaining generators of TPHIC [32], PHOJET [33, 34], and DPEMC [35] are in general all based upon the EPA formalism. Differences between the functionalities of the programs, such as the available number of final states from the $\gamma\gamma$ collision, exist. The DPEMC program has the added feature of including several models of double Pomeron exchange, such as the inclusive process as shown in Figure 4.4 which is a background to the two photon production of lepton pairs [36]. The results presented in Chapter 5 are based upon the LPAIR and DPEMC Monte Carlo generators as they best represent the process of two photon interactions during pp collisions at the LHC. ¹ The Pythia [37] Monte Carlo generator is used for the simulation of various background processes to the production of $\mu^+\mu^-$ pairs from two photon collisions at the LHC.

4.2 Single Gauge Boson Production at the LHC

At the CERN LHC (and the Fermilab Tevatron) the main process by which the γ^*/Z or W intermediate vector boson is generated is via the Drell-Yan process [38] in which a quark and anti-quark annihilate.

¹A discussion of the non-applicability of TPHIC to the simulation of $\gamma\gamma$ collisions during pp running at the LHC will be given in 5.1.

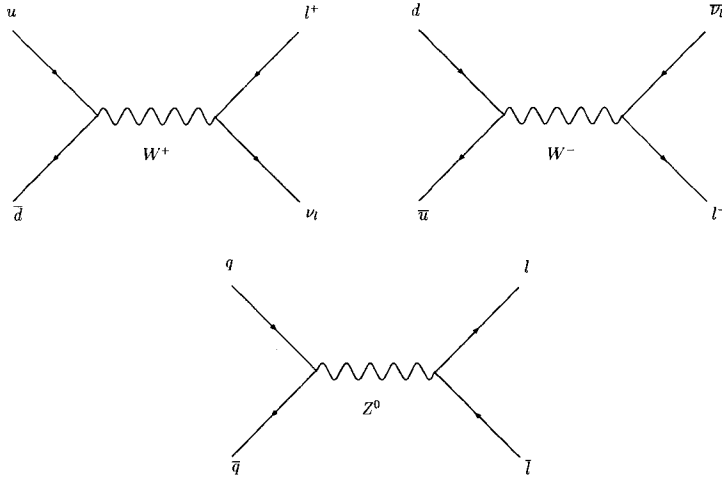


Figure 4.5: Feynman diagrams for the production of W and Z bosons via Drell-Yan at Leading Order QCD.

$$q + \bar{q} \rightarrow \gamma^*/Z \quad (4.17)$$

$$u + \bar{d} \rightarrow W^+ \quad (4.18)$$

$$\bar{u} + d \rightarrow W^- \quad (4.19)$$

The Feynman diagrams for the Drell-Yan production of W and Z are shown in Figure 4.5. Here the Drell-Yan process occurs through the collision of valence quark and sea quark (or sea quark and sea anti-quark) of the same flavour for the Z^0 . For the production of W bosons it requires the collision of either valence quark and anti-quark from the sea or sea quark and sea anti-quark in which the annihilating quarks are of different flavour. Figure 4.6 demonstrates the cross section for various hard scattering processes including the production of W and Z as a function of \sqrt{s} [39]. The cross sections for such production at the Tevatron and LHC are marked by the dashed lines and can be analytically written as

$$\sigma_{W^+} = \int dx_1 dx_2 F_{u/p} F_{\bar{d}/p} \hat{\sigma}(u\bar{d} \rightarrow W^+) \quad (4.20)$$

$$\sigma_{W^-} = \int dx_1 dx_2 F_{\bar{u}/p} F_{d/p} \hat{\sigma}(\bar{u}d \rightarrow W^-) \quad (4.21)$$

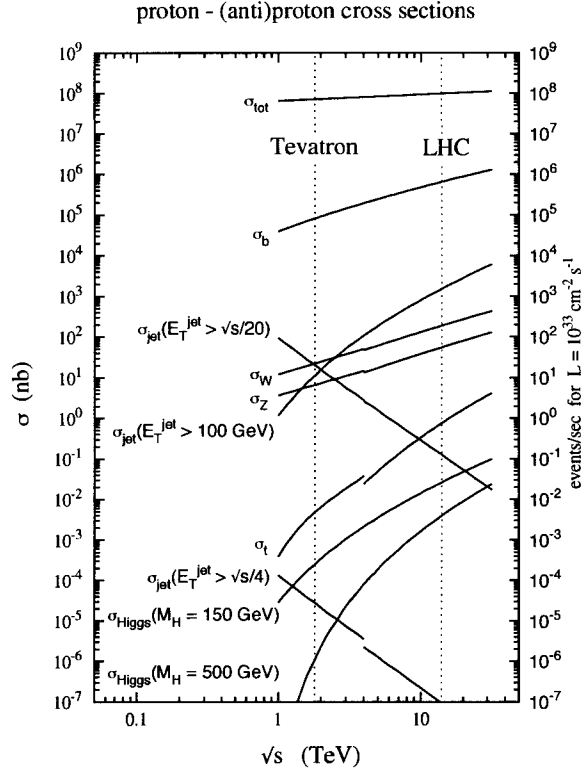


Figure 4.6: Cross section for hard scattering, including the production of W and Z , as a function of \sqrt{s} at the Tevatron and LHC.

where $\hat{\sigma}(u\bar{d} \rightarrow W^+)$ (and $\hat{\sigma}(\bar{u}d \rightarrow W^-)$) is the cross section when the u and \bar{d} (and the \bar{u} and d) annihilate. The Parton Distribution Functions (PDFs) $F_{q/p}(x)$ give the probability of finding a quark q inside a proton that carries a fraction x of the momentum of the proton, p .

$$\sigma_{u\bar{d} \rightarrow W^+} = 2\pi \frac{G_F}{\sqrt{2}} M_W^2 \delta(\hat{s} - M_W^2) \quad (4.22)$$

Since $dx_1 dx_2 = x_1 x_2 d\hat{s} dY / \hat{s}$ where Y is the rapidity of the W in the centre-of-mass frame.

$$Y = \frac{1}{2} \ln [(E + P_z)/(E - P_z)] \quad (4.23)$$

$$\frac{d\sigma}{dY}(W^+) = K \frac{2\pi G_F}{3\sqrt{2}} x_1 x_2 F_{u/p}(x_1) F_{\bar{d}/p}(x_2) \quad (4.24)$$

$$\frac{d\sigma}{dY}(W^-) = K \frac{2\pi G_F}{3\sqrt{2}} x_1 x_2 F_{\bar{u}/p}(x_1) F_{d/p}(x_2) \quad (4.25)$$

$$(4.26)$$

At leading order the momentum fraction can be related to the mass and rapidity of the produced vector boson.

$$x_{1+,2-} = \frac{M_W}{\sqrt{s}} e^{\pm Y} \quad (4.27)$$

Figure 4.7 shows a map of Q^2 as a function of x for the production of a particle of mass M at rapidity Y at the LHC. Also shown is the kinematic coverage of HERA and fixed target experiments from which the PDF fits are made [16]. Therefore the product of the parton momentum fraction $x_1 x_2$ is constrained by the mass of the produced particle and the centre of mass energy of the collider. For the production of W and Z the value of Q^2 is approximately 10^4 GeV^2 and therefore the product of the parton momentum fractions $x_1 x_2$ is $\approx 5 \times 10^{-2}$ at $y = 0$.

The W and Z can decay as

$$W^+ \rightarrow (e^+ \nu_e)(\mu^+ \nu_\mu)(\tau^+ \nu_\tau)(u\bar{d})(c\bar{s}) \quad (4.28)$$

$$W^- \rightarrow (e^- \bar{\nu}_e)(\mu^- \bar{\nu}_\mu)(\tau^- \bar{\nu}_\tau)(\bar{u}d)(\bar{c}s) \quad (4.29)$$

$$Z \rightarrow (e^+ e^-)(\mu^+ \mu^-)(\tau^+ \tau^-)(\nu \bar{\nu})(u\bar{u})(d\bar{d})(c\bar{c})(s\bar{s})(b\bar{b}) \quad (4.30)$$

In order to utilize W and Z production as a luminosity monitoring technique clean identification of the leptons is required. Therefore examination of the decay processes of the W and Z is restricted to the muon and electron channels only.

4.2.1 Parton Distribution Functions

Parton Distribution Functions (PDFs) are important tools that enable the prediction of physical cross sections and their uncertainty ranges. They are

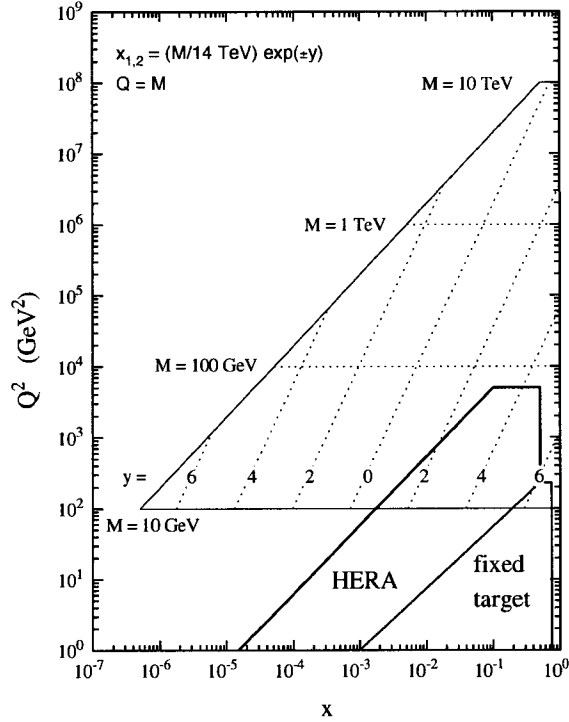


Figure 4.7: Kinematic map of Q^2 as a function of x for the production of a particle of mass M at rapidity Y at the LHC.

needed for both precision Standard Model measurements as well as for searches of new physics beyond the Standard Model. The PDFs are determined via global fits to current data collected for deep inelastic scattering, Drell-Yan, jet and direct photon production. Various research groups that provide PDFs that can be used within theoretical calculations and numerical simulations include the CTEQ, MRST, Alekhin and ZEUS distributions. A listing of the currently available PDFs that have been produced with error sets is given in Table 4.1. Copies of the various PDF sets are available for download from [40].

The experimental datasets, upon which the CTEQ6 and MRST2001 analyses are based, are essentially the same, with some small differences in the data incorporated. For example, the very low Q^2 data from the SLAC experiments is omitted in the CTEQ6 analysis. The method by which the experimental uncertainties are treated in the fitting process also differ between the two groups. The CTEQ6 and MRST2001 sets also differ in terms of the theoretical calculations used to describe the deep inelastic scattering structure functions.

PDF	No. eigenvectors	No. PDF members	$\Delta\chi^2$	Reference
CTEQ61E	20	40	100	[41]
MRST2001E	15	30	50	[42]
Alekhin02NLOE	15	30	1	[43]
ZEUS 2005	11	22	50	[44, 45]

Table 4.1: Available PDF error sets and their associated number of eigenvectors and $\Delta\chi^2$ from the Hessian approach.

CTEQ6 utilizes the conventional zero-mass parton Wilson coefficients, while MRST2001 use the non-zero parton mass variable flavour number scheme. Further details on the differences in methodology can be found elsewhere [41].

PDF Uncertainties [41, 46]

The uncertainties of the PDFs have been estimated using the Hessian method by which the space of potential PDF parameter values, P_i , is mapped out based upon the experimental results which are used as constraints for the fit. The CTEQ61E and MRST2001E PDF fits use 20 and 15 parameters, respectively, which are tuned to the most likely values through the χ^2 minimization of a global fit to experimental data. Figure 4.8 demonstrates the concepts of the Hessian method. The functional form of the PDF parameterization can be written as

$$F(x, Q) = a_0 x^{a_1} (1-x)^{a_2} P(x; a_3, \dots, a_i) \text{ and } i = 1, \dots, N \quad (4.31)$$

where a_i are the fit parameters. Performing the global fit using N free parameters results in the determination of a central value S_0 . It is at this point in the method that the global χ^2 is increased by a tolerance $\Delta\chi^2 = T^2$ so as to form an error matrix, the Hessian H_{ij} , where the tolerance represents the individual $\pm 1\sigma$ uncertainty of each parameter of the fit.

$$\Delta\chi^2 = \chi^2 - \chi_0^2 = \sum_{i=1}^N \sum_{j=1}^N H_{ij} (a_i - a_i^0) (a_j - a_j^0) \quad (4.32)$$

However the error matrix is not diagonalized at the central value S_0 and in turn it is difficult to convert from errors in the fit parameters P_i to uncertainties

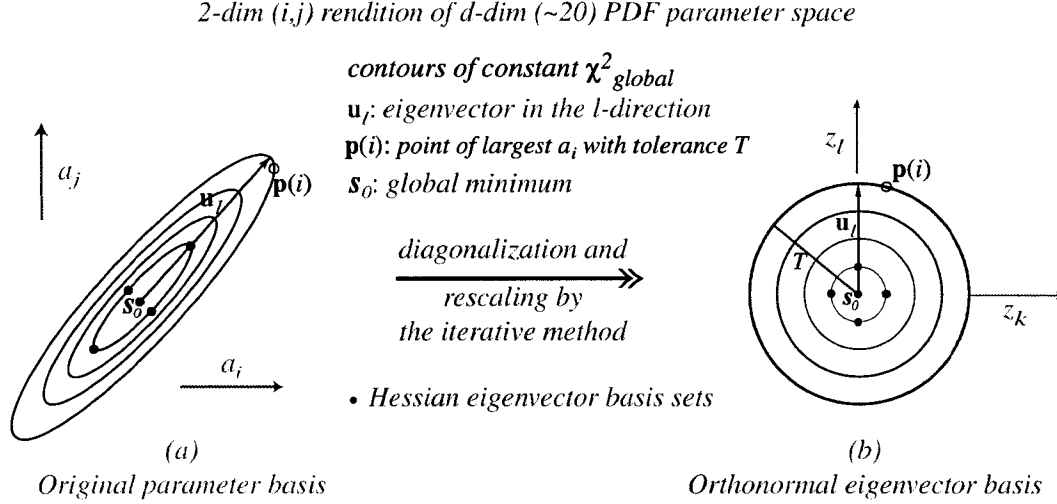


Figure 4.8: Hessian method description.

of quantities that have been measured experimentally. Diagonalizing the error matrix results in the construction of N linearly independent eigenvectors Q_i . The individual $\pm 1\sigma$ variations of each eigenvector is then transformed back into the parameter space described by the values of P_i , and in turn generates a set of up and down error PDFs for each Q_i yielding $2N$ new members of the PDF set. The number of eigenvectors used by each group in their respective PDF error set fit varies as listed in Table 4.1. The value of the tolerance T (and therefore $\Delta\chi^2$) chosen to represent the $\pm 1\sigma$ variations is also taken differently among the various parameterizations.

Therefore for an observable X we can calculate the best estimate from the PDF Set S_0 and the corresponding uncertainty from the up and down error PDFs according to the formula

$$\Delta X = \frac{1}{2} \left(\sum_{i=1}^{N_P} [X(S_i^+) - X(S_i^-)]^2 \right)^{1/2} \quad (4.33)$$

where $X(S_i^\pm)$ are the predictions for this observable based on the PDF sets S_i^\pm from the eigenvector basis. Since equation 4.33 assumes symmetric errors a slight modification must be made to the computation for the correct handling of asymmetric errors. This correction will be discussed in 7.1.4. For each of the CTEQ61E, MRST2001E, Alekhin02NLOE and ZEUS 2005 PDFs the error set

distributions for each parton flavour at $Q^2 = 10^4 \text{ GeV}^2$ is shown in Figures 4.9, 4.10, 4.11, 4.12, respectively. Also shown are the percentage uncertainty of each PDF set relative to the best-fit PDF as a function of x . The choice of $Q^2 = 10^4 \text{ GeV}^2$ corresponds to the value necessary for the production of W and Z at the LHC.

Future Development of PDFs

The next period of datataking by ZEUS at HERA-II is expected to run until approximately mid-2007 at which point an integrated luminosity in excess of 500 pb^{-1} is anticipated. The current ZEUS PDF fits were constructed from the HERA-I data collected up until 2000 and were typically based upon accumulated data samples of up to 12 pb^{-1} [44, 47]. It is projected that at HERA-II the ZEUS PDF fits will undergo significant improvements in the valence quark uncertainties over the whole range of x and for sea quarks at high x values due to the increased statistical precision of the high Q^2 data [48], thereby contributing to the overall improvement in the PDF error estimates prior to the start of the LHC.

4.2.2 Monte Carlo generators

In order to simulate the production of W and Z at the LHC the most commonly used generators include Pythia [37] and Herwig [49, 50]. Other programs that are available but not included in the studies presented here include MC@NLO [51] and RESBOS [52]. MC@NLO includes the effects of NLO QCD corrections to the simulation, while RESBOS and RESBOS-A apply the method of QCD resummation and higher order QED corrections, respectively [53]. Higher order QCD corrections at NLO and NNLO to the predicted cross sections (but not the simulations) are possible from the techniques described in [54]. Detailed usage and modifications to the software codes that enable the calculation of the higher order corrections together with the PDF error sets is for the first time describe in 7.1.3 of this thesis.

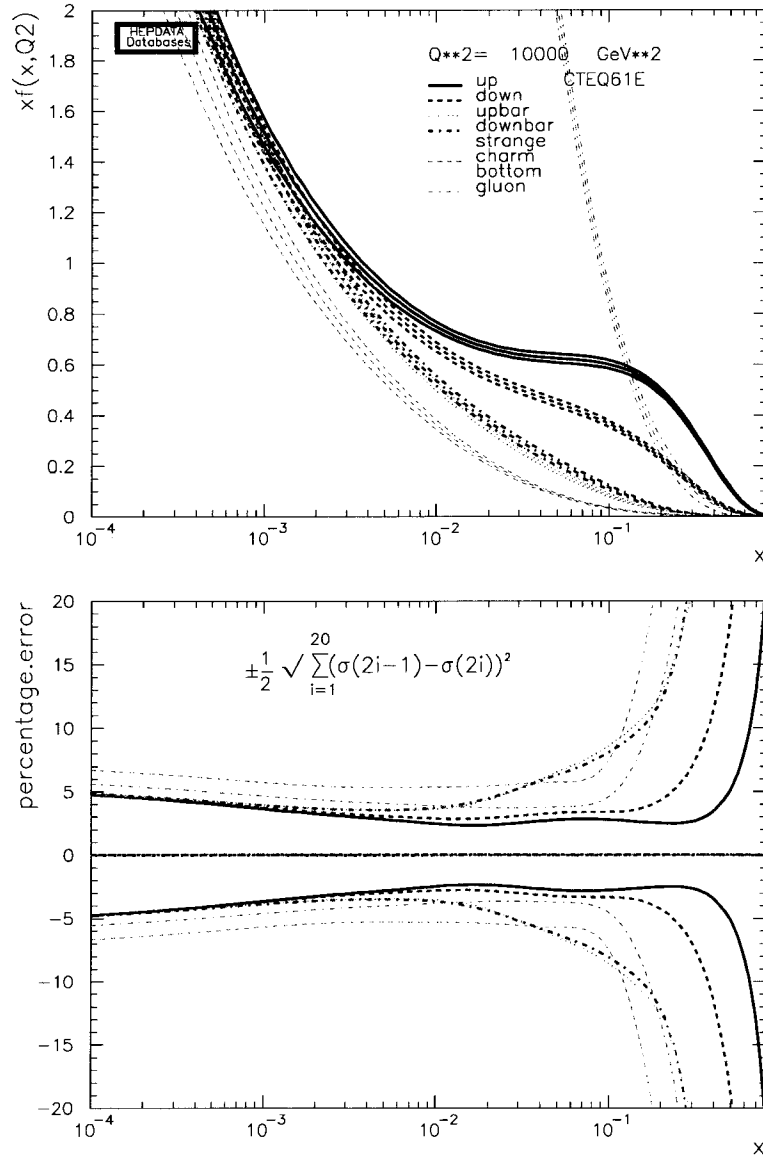


Figure 4.9: Plot of the CTEQ61E PDF error set distributions for each parton at $Q^2 = 10^4 \text{ GeV}^2$ (top) and the corresponding percentage uncertainty relative to the best fit PDF member (bottom).

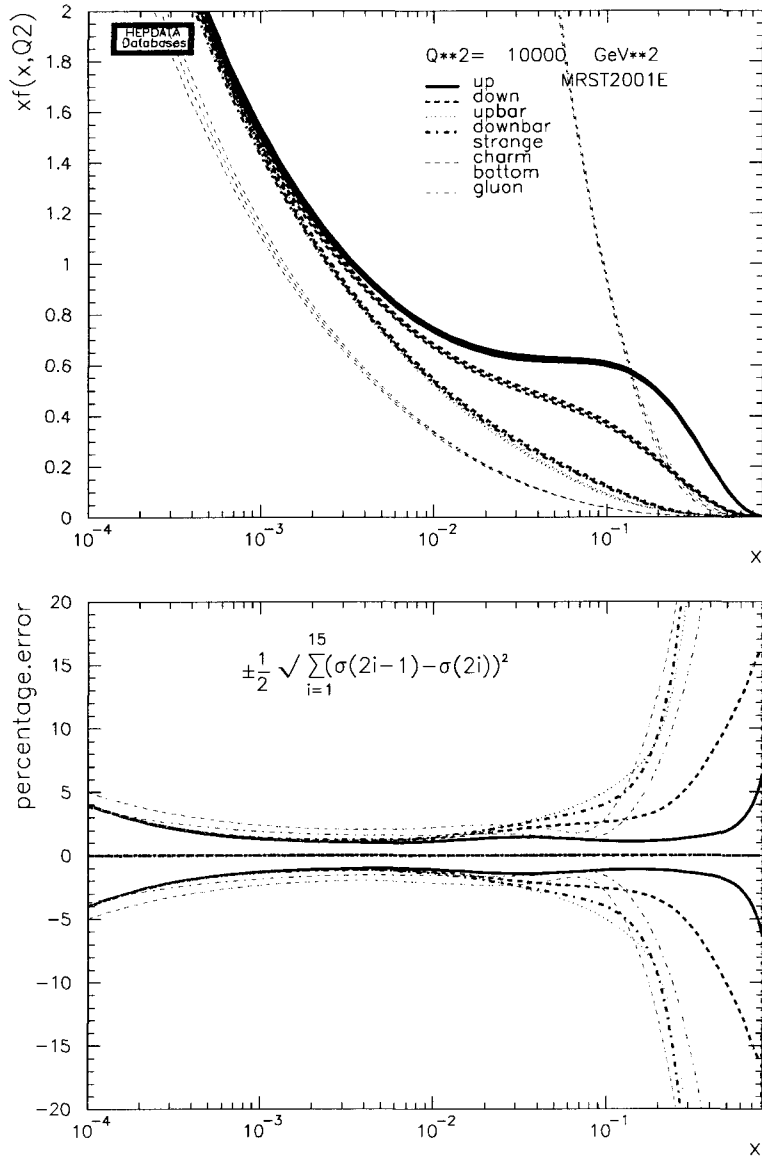


Figure 4.10: Plot of the MRST 2001 PDF error set distributions for each parton at $Q^2 = 10^4 \text{ GeV}^2$ (top) and the corresponding percentage uncertainty relative to the best fit PDF member (bottom).

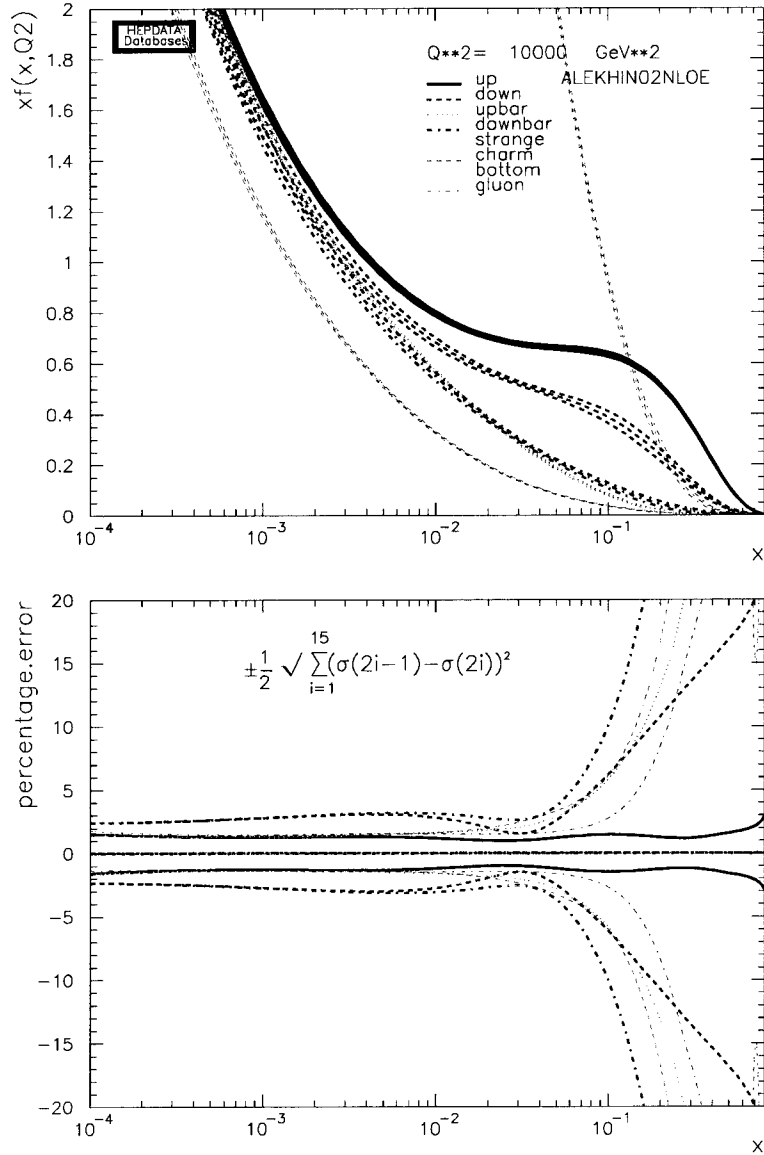


Figure 4.11: Plot of the Alekhin02 NLO PDF error set distributions for each parton at $Q^2 = 10^4 \text{ GeV}^2$ (top) and the corresponding percentage uncertainty relative to the best fit PDF member (bottom).

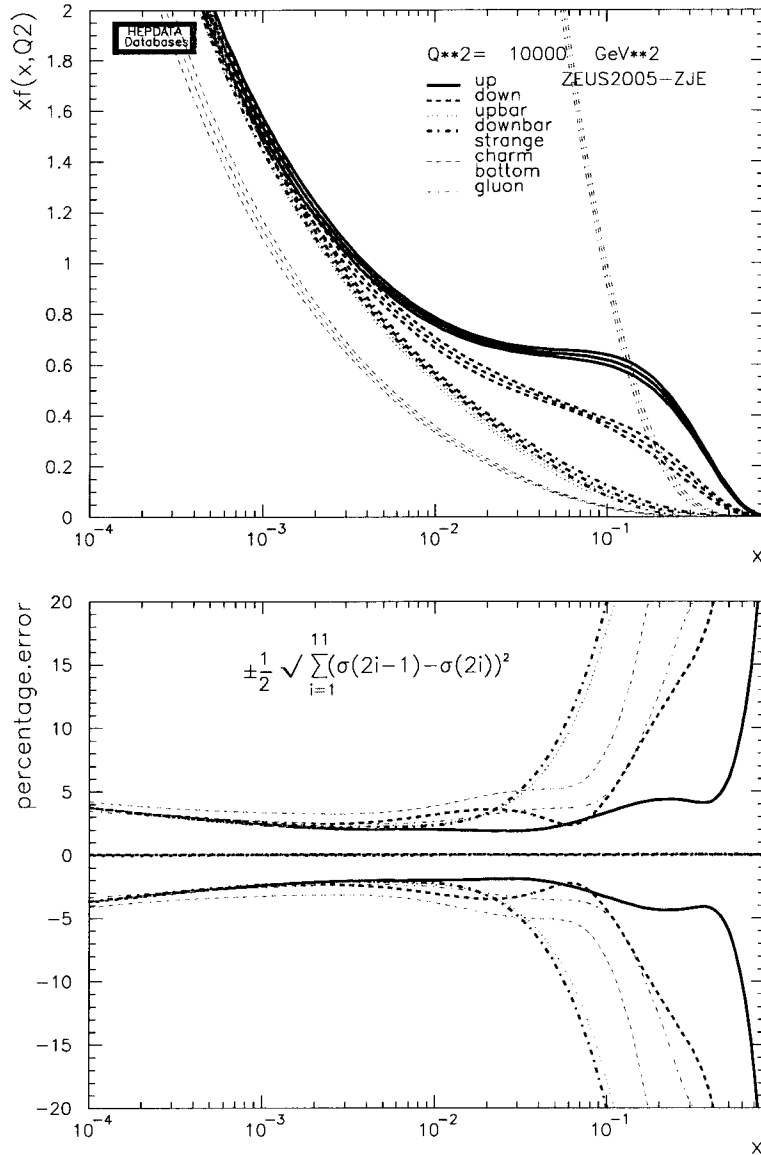


Figure 4.12: Plot of the ZEUS 2005 PDF error set distributions for each parton at $Q^2 = 10^4 \text{ GeV}^2$ (top) and the corresponding percentage uncertainty relative to the best fit PDF member (bottom).

Chapter 5

Luminosity Measurement via Two Photon Interactions

The theory which underlies the description of the collision of virtual photons arising from the electromagnetic field of the LHC beams was presented in 4.1. In this chapter two of the theoretical approaches as implemented in the form of Monte Carlo simulations will be used to study the production of $\gamma\gamma \rightarrow \mu^+\mu^-$ events in proton-proton collisions with ATLAS. A review of both the general and specific event characteristics will be given, along with the kinematic criteria and tools that are used to estimate and eliminate the false identification of $\gamma\gamma \rightarrow \mu^+\mu^-$ events which come from various background processes. The presented results will also take into consideration the requirements for muon selection as defined by the ATLAS Trigger system. Finally a brief comparison will be made with the similar process of $\gamma\gamma \rightarrow e^+e^-$, demonstrating the much broader potential of the two photon production of $\mu^+\mu^-$ pairs as a luminosity measurement process, even in the LHC environment of pileup from minimum bias events.

5.1 Muon pair production

5.1.1 Event characteristics

Within ATLAS individual muons must have a transverse momentum $p_T(\mu^\pm)$ greater than 3 GeV/c in order to reach the wall of muon chambers within the central tracking region of $|\eta| < 2.7$. However the muon trigger system of

ATLAS presently has a Level-1 p_T threshold of 6 GeV/c. This lower limit is primarily necessary to maintain a single muon trigger rate that is not too large but is also efficient in triggering upon muons. Table 5.1 lists the typical Level-1 muon trigger efficiencies over various η ranges.

The production of di-muon pairs from the collision of two photons at the LHC are typically centrally produced with low transverse momentum $p_T(\mu^\pm)$, and small invariant mass. Additionally the total transverse momentum of the muon pair, $p_T(\mu^+\mu^-)$ is also quite small. As will be evident the acoplanarity angle ϕ , as defined in Figure 5.1 is centered around zero for elastic $\gamma\gamma$ collisions.

Although other two photon collision generators such as TPHIC were previously mentioned in 4.1.2, it was found that the kinematic behaviour of the outgoing lepton pair within TPHIC was only correctly modelled in the situation of two photon collisions arising from incoming heavy ion beams and not for pp or $p\bar{p}$ collisions. In all events the value of acoplanarity angle ϕ was calculated to have a value of zero. For two photon collisions arising from the electromagnetic fields of the ion beams the maximum perpendicular transverse momentum transfer is dependent upon the radius R of the colliding nuclei and must satisfy the requirement of $q_\perp \leq 1/R$ [26] where R is the radius of the nuclei in units of fm given by

$$R = 1.2 A^{1/3} \quad (5.1)$$

For heavy ion collisions the value of R from 5.1 results in a value of $q_\perp \approx 0$. However, for lighter colliding nuclei, such as protons, the radius R is sufficiently small that the same approximation cannot be made for the value q_\perp . Therefore the zero acoplanarity angle ϕ is only a good approximation for heavy ions and is not appropriate to describe two photon collisions when the LHC is operating in proton-proton collider mode.

5.1.2 Trigger Definitions and efficiencies

The ATLAS Level-1 muon trigger is based upon the measurement of muon trajectories traversing three different planes, known as stations. Figure 5.2

$ \eta $ Region	Level-1 Efficiency (± 0.05)
< 0.4	0.80
$0.4 - 0.8$	0.82
$0.8 - 1.2$	0.75
$1.2 - 1.6$	0.95
$1.6 - 2.0$	0.98
$2.0 - 2.4$	0.90

Table 5.1: Efficiency of the ATLAS Level-1 muon trigger at the low p_T threshold of 6 GeV/c for various regions of coverage.

demonstrates the ATLAS Level-1 muon trigger scheme in which the muon trajectories are deflected by the magnetic field of the ATLAS toroid. The amount of deflection is dependent upon the muon momentum and the magnetic field strength along the path traversed. Single muon p_T thresholds of 6 GeV/c and 20 GeV/c are employed at the Level-1 trigger for the selection of low and high p_T muons, respectively. In the central region the low p_T trigger is constructed with information from the two innermost RPC chambers of the MDT. High p_T triggers are formed from muons which are able to traverse three layers of RPCs. The efficiency of the low p_T muon trigger of 6 GeV/c at Level-1 is listed in Table 5.1 as a function of the pseudorapidity region covered [17].

The possibility of deploying single muon triggers with p_T thresholds below the current 6 GeV/c level are been studied within ATLAS and would take advantage of the Barrel Tile Calorimeter's third layer which is able to strongly discriminate between muons and hadrons. The development of di-muon triggers at Level-1 is also been studied within ATLAS. It should be noted that the Level-1 single muon trigger threshold will be much lower (typically around 3 GeV/c), during heavy ion runs. The decrease in collision luminosity to $10^{27} \text{cm}^{-2} \text{s}^{-1}$ in collision mode will be offset by the enhanced photon flux due to the increased Z of the colliding nuclei. Therefore it should also be possible to study two photon to $\mu^+ \mu^-$ events during the ATLAS heavy ion runs.

The efficiency for the reconstruction of single muons at the Level-2 trigger and Event Filter have been studied using Monte Carlo simulations [55].

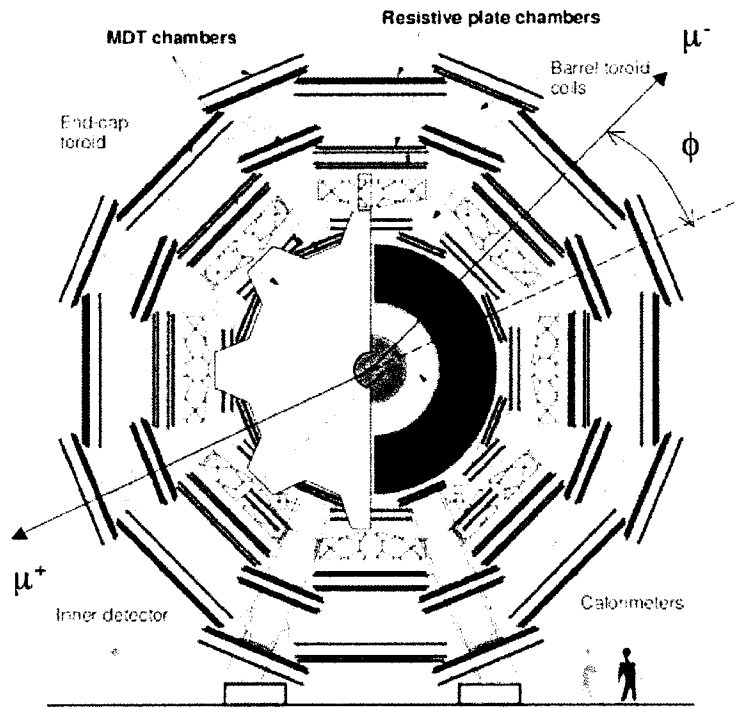


Figure 5.1: Schematic representation of the ATLAS muon detector system and the measure of the acoplanarity angle ϕ for $\mu^+\mu^-$ pair production at the LHC.

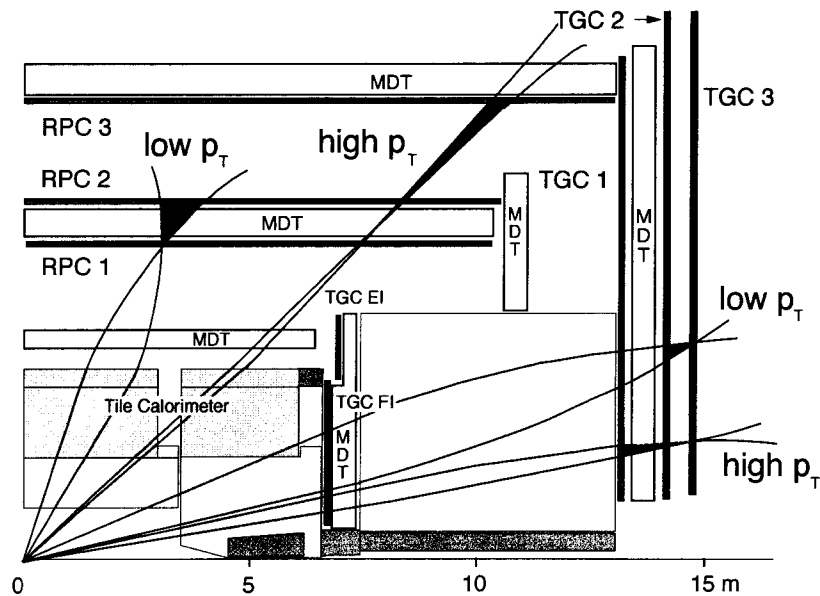


Figure 5.2: The ATLAS Level-1 muon trigger system.

When combining the tracking information of the inner detector along with the muon selection algorithms of MOORE and MuId the overall efficiency for muon reconstruction is greater than 90% for muons with $p_T > 7$ GeV/c. This efficiency falls rapidly with decreasing p_T to approximately 25% at values near 3 GeV/c.

5.1.3 Event selection, efficiency, and rate

In order to select two photon production of $\mu^+\mu^-$ events several important kinematic variables emerge with varying strengths to identify the process of interest. The initial set of loose kinematic criteria applied to all signal and background simulation samples are listed in Table 5.2 and is followed by a brief discussion of each variable.¹ In all results presented here the generated Monte Carlo samples were passed through the ATLAS Fast Simulation program ATLFAST in order to establish as close as possible a realistic description of the detector resolution and performance effects but without having to simulate the event with the full ATLAS Geant4 based simulation. Furthermore, due to the specialized nature of the available two photon generators, it was necessary to convert all generator output information into ASCII format which was then subsequently read into the ATLFAST simulation program via the Athena software framework. The selection criteria presented here were studied in parallel with a similar effort within the ATLAS collaboration. Both studies were presented within the ATLAS Luminosity Working Group which reviewed the feasibility of using two photon production of $\mu^+\mu^-$ events for luminosity measurement [56–58].

Acoplanarity angle ϕ

The acoplanarity angle ϕ is defined as the angular measure of the difference of two tracks from being back-to-back when their respective tracks are projected onto the plane transverse to the beam axis, therefore being the $x - y$

¹For some of the distributions, the criteria on the relevant kinematic variable was removed so as to show the full spectrum of values possible. Also the loose selection criteria includes a muon p_T threshold of 3 GeV/c which is necessary for the muons to reach the muon detector system at ATLAS.

Kinematic Variable	Criteria 1 (Loose Cuts)	Criteria 2 (Tight Cuts)
$\mu^+\mu^-$ Invariant Mass	$< 60 \text{ GeV}/c^2$	$< 20 \text{ GeV}/c^2$
$p_T(\mu^\pm)$	$> 3 \text{ GeV}/c$	$> 6 \text{ GeV}/c$
$\mu^+\mu^-$ pair p_T	$< 0.25 \text{ GeV}/c$	$< 0.15 \text{ GeV}/c$
acoplanarity angle ϕ	$< 0.10 \text{ rad}$	$< 0.01 \text{ rad}$

Table 5.2: General kinematic selection criteria applied for the selection of $\mu^+\mu^-$ pairs from two photon interactions at the LHC.

plane. A schematic representation of the acoplanarity angle ϕ definition with an overlay of the ATLAS muon detector system is shown in Figure 5.1.

Figure 5.3 presents the predicted cross section as a function of the reconstructed acoplanarity angle ϕ for the signal two-photon to $\mu^+\mu^-$ events from the LPAIR and DPEMC Monte Carlo generators, as well as for the semi-inelastic and inelastic backgrounds from LPAIR in which either one or both of the protons dissociates upon emission of the photon. The simulation of the elastic process from LPAIR and DPEMC are in approximate agreement within the region of $|\phi| < 0.025$ with a large difference in the predicted differential cross section for the $\phi = 0$ bin. Beyond this value of ϕ the DPEMC result, which is based upon the Equivalent Photon Approximation, quickly decreases in comparison to the Matrix Element calculations of LPAIR. Noticeably similar in shape and magnitude is the distribution for the background process of $\mu^+\mu^-$ pairs coming from the inclusive double Pomeron exchange (DPE) simulation.

A scatter plot demonstrating the relationship between the measured acoplanarity angle ϕ and the ratio of the muon transverse momentum $p_T(\mu^+)/p_T(\mu^-)$ is presented in Figure 5.6. The $\mu^+\mu^-$ pair from the signal elastic two photon production and background DPE events, with their similar acoplanarity angle distributions, are also clearly very balanced when considering the magnitude of the p_T for each muon. This is further visible from a plot of the cross section as a function of the $p_T(\mu^+)/p_T(\mu^-)$ ratio given in Figure 5.5.

Similarly the three dimensional histogram of Figure 5.4 displays the relationship between the reconstructed acoplanarity angle ϕ and the $p_T(\mu^+)/p_T(\mu^-)$ ratio for the elastic, semi-inelastic and fully inelastic cases. The dominant process in the near-zero ϕ -angle region comes from the signal elastic $\gamma\gamma \rightarrow \mu^+\mu^-$

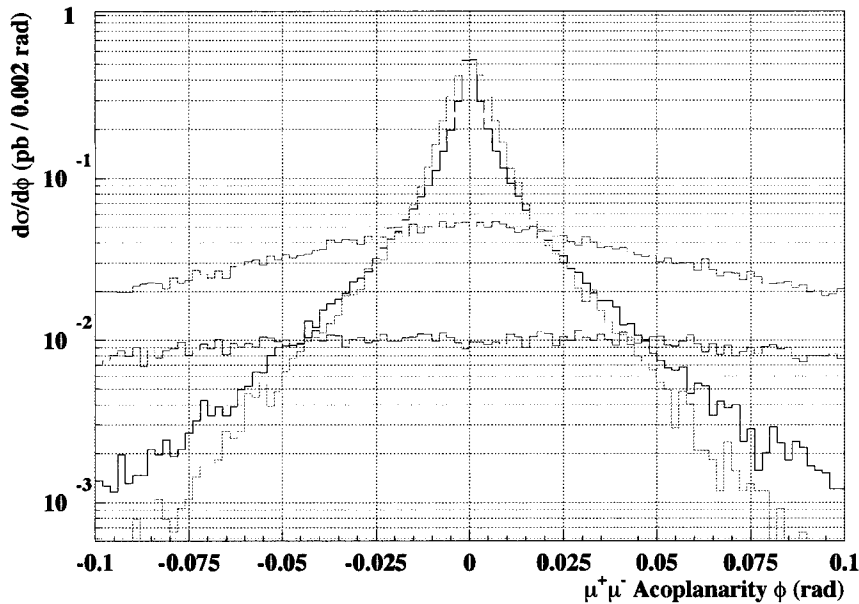


Figure 5.3: Cross section as a function of acoplanarity angle ϕ for the muon pair produced from $\gamma\gamma$ interactions in ATLAS. Shown are the distributions for elastic (black), semi-inelastic (blue), and fully inelastic (red) production via LPAIR, and elastic (green) and double pomeron exchange background (pink) from DPEMC.

events highlighted in red. The amount of the contributions from the (semi-)inelastic cases are overlaid onto the elastic distribution, thereby indicating the total cumulative cross section for all three processes.

Muon pair p_T

As has been previously indicated in Section 4.1, the reconstructed value of the total transverse momentum of the muon pair, $p_T(\mu^+\mu^-)$, is an important factor when attempting to take into account the background contributions due to rescattering effects. Figure 5.7 shows the predicted cross sections for the signal and background events as a function of the reconstructed $p_T(\mu^+\mu^-)$. The background (semi-)inelastic and DPE distributions decrease more gradually with rising $p_T(\mu^+\mu^-)$ in comparison with the signal elastic events. This difference would be particularly important considering that the distributions of acoplanarity angle ϕ and the transverse momentum balance of $p_T(\mu^+)/p_T(\mu^-)$

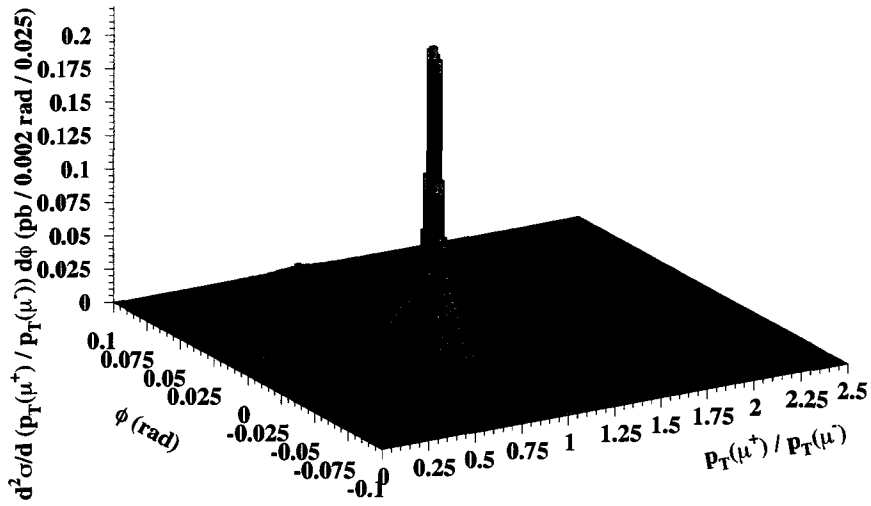


Figure 5.4: Two dimensional histogram demonstrating the relative cross sections in the acoplanarity angle ϕ versus transverse momentum ratio parameter space. Shown are the distributions for elastic (red), semi-inelastic (green), and fully inelastic (blue) production via the LPAIR generator.

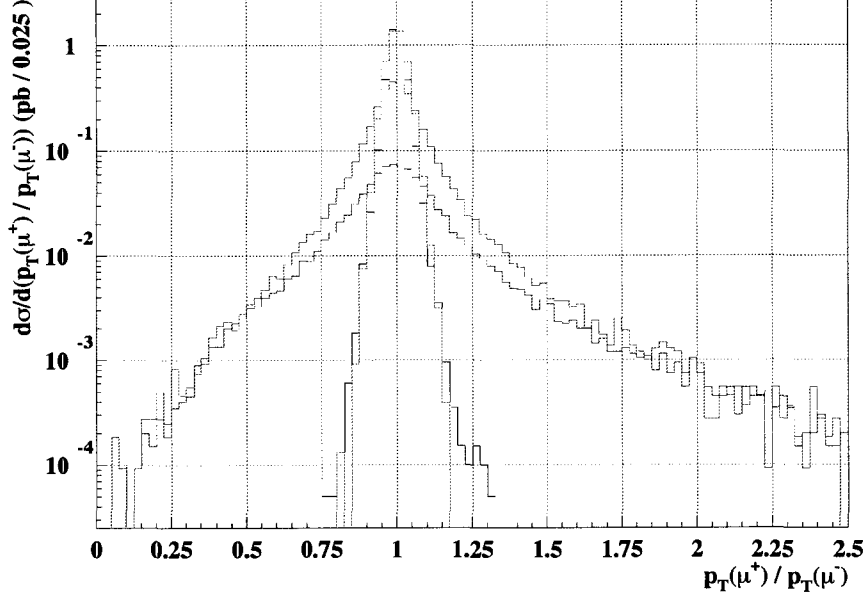


Figure 5.5: Cross section as a function of $p_T(\mu^+)/p_T(\mu^-)$ for the muon pair produced from $\gamma\gamma$ interactions in ATLAS. Shown are the distributions for elastic (black), semi-inelastic (blue), and fully inelastic (red) production via LPAIR, and elastic (green) and double pomeron exchange background (pink) from DPEMC.

are very similar for the elastic $\gamma\gamma$ and DPE processes.

The cross section as a function of the difference in the $\mu^+\mu^-$ p_T values, as shown in Figure 5.8, can provide some level of discrimination against the potential backgrounds through a requirement of $|p_T(\mu^+) - p_T(\mu^-)| < 0.25$ GeV/c.

Invariant Mass

Figure 5.9 displays the cross section as a function of the reconstructed $\mu^+\mu^-$ invariant mass for both the signal two photon and background processes. Visible near 90 GeV/ c^2 is the Z^0 invariant mass peak from the double pomeron exchange background. Therefore a cut in the invariant mass at 20 GeV/ c^2 is applied to remove the background peak.

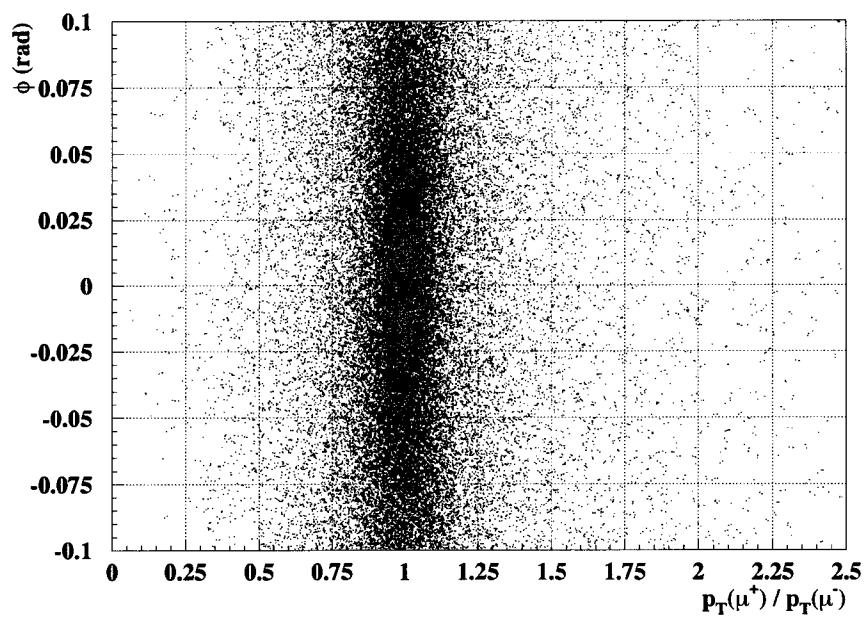


Figure 5.6: Scatter plot demonstrating the measured acoplanarity angle ϕ as a function of the ratio $p_T(\mu^+)/p_T(\mu^-)$ measured in ATLAS. Shown are the distributions for elastic (black), semi-inelastic (blue), and fully inelastic (red) production via LPAIR, and elastic (green) and double pomeron exchange background (pink) from DPEMC.

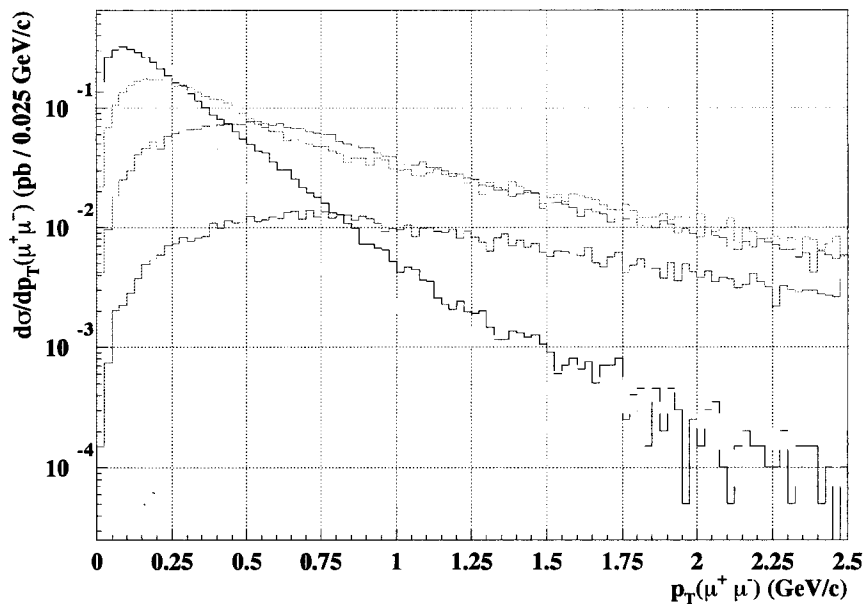


Figure 5.7: Cross section as a function of the total $\mu^+\mu^-$ pair p_T for the muon pair produced from two photon interactions in ATLAS. Shown are the distributions for elastic (black), semi-inelastic (blue), and fully inelastic (red) production via LPAIR, and elastic (green) and double pomeron exchange background (pink) from DPEMC.

Other Kinematic Characteristics

In addition to the more discriminating kinematic quantities described above, there are some common characteristics shared between the signal and various background processes that individually would not aid in the selection of elastic $\gamma\gamma \rightarrow \mu^+\mu^-$. For example Figure 5.10 shows the cross section as a function of the individual muon p_T values where the shape of the distributions are very similar, particularly for the low p_T region. However some separation of signal and background is possible when considering the level of correlation between the μ^+ and μ^- transverse momenta values as indicated in Figure 5.11.

Track Transverse Momentum and Angular Resolutions

Particularly important to the measurement of the acoplanarity angle and muon pair p_T are the expected values of the $1/p_T$ and ϕ angle resolutions which

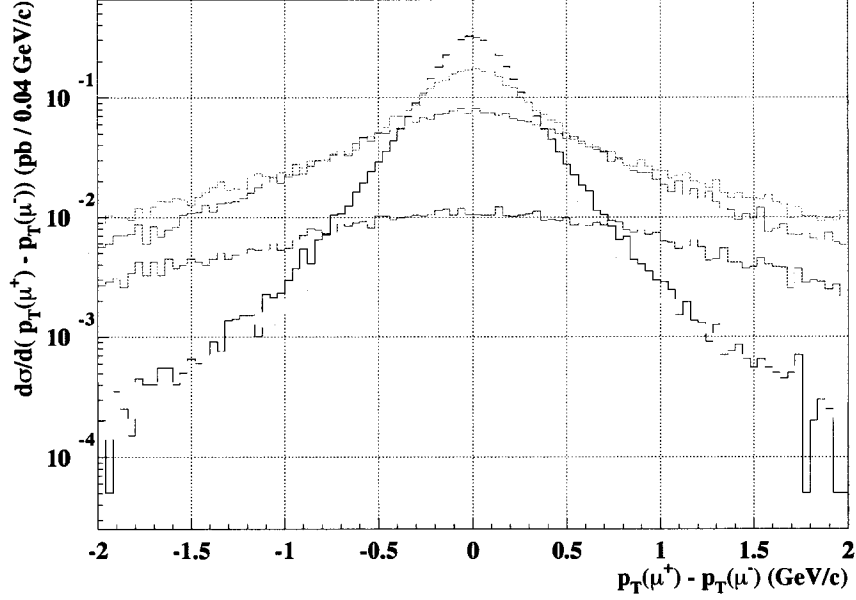


Figure 5.8: Cross section as a function of $p_T(\mu^+) - p_T(\mu^-)$ for the muon pair produced from $\gamma\gamma$ interactions in ATLAS. Shown are the distributions for elastic (black), semi-inelastic (blue), and fully inelastic (red) production via LPAIR, and elastic (green) and double pomeron exchange background (pink) from DPEMC.

can be achieved with the ATLAS inner detector. Studies [17] have found that for the the passage of muons with $p_T = 5 \text{ GeV}/c$ the expected resolutions from the measured track helix parameters to be

$$\sigma(1/p_T) \approx 2.5 - 5.5 \text{ TeV}^{-1} \quad (5.2)$$

$$\sigma(\phi) \approx 0.25 - 0.40 \text{ mrad} \quad (5.3)$$

Therefore the application of strict acoplanarity angle ϕ cuts as small as 0.01 rad should be achievable with the tracking information available at ATLAS.

5.1.4 Background Identification and Estimation

The processes of (semi-)inelastic two photon collisions, as well as that from inclusive DPE, have been reviewed and shown to provide strong backgrounds

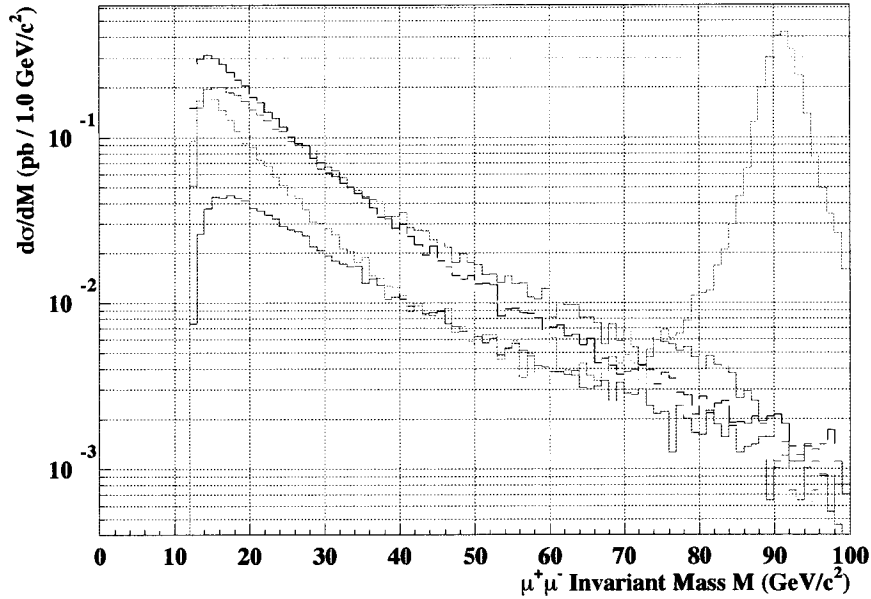


Figure 5.9: Cross section as a function of $\mu^+\mu^-$ invariant mass from $\gamma\gamma$ interactions in ATLAS. Shown are the distributions for elastic (black), semi-inelastic (blue), and fully inelastic (red) production via LPAIR, and elastic (green) and double pomeron exchange background (pink) from DPEMC.

to the signal channel of interest. A separation of $\gamma\gamma$ from DPE process should be possible in general by applying an upper limit on the total p_T of the muon pair. The installation of forward tagging detectors, such as Roman pots, would likely help in this situation as well since these could be used to detect the forward scattered protons.

Additionally the production of $\mu^+\mu^-$ pairs from Drell-Yan (either directly or from $b\bar{b}$ and $c\bar{c}$ with muonic decays) and Leading Order QCD are backgrounds for the observation of this process at the LHC. Table 5.3 lists the expected cross sections for the signal two photon and these backgrounds based on the application of the loose selection cuts of Table 5.2.

Figure 5.12 shows the normalized levels of $\mu^+\mu^-$ pairs expected from the elastic two photon process as well as from Drell-Yan for the measured individual and $\mu^+\mu^-$ pair p_T distributions based upon the application of the selection criteria listed in Table 5.2. An additional tight cut on the acoplanarity angle

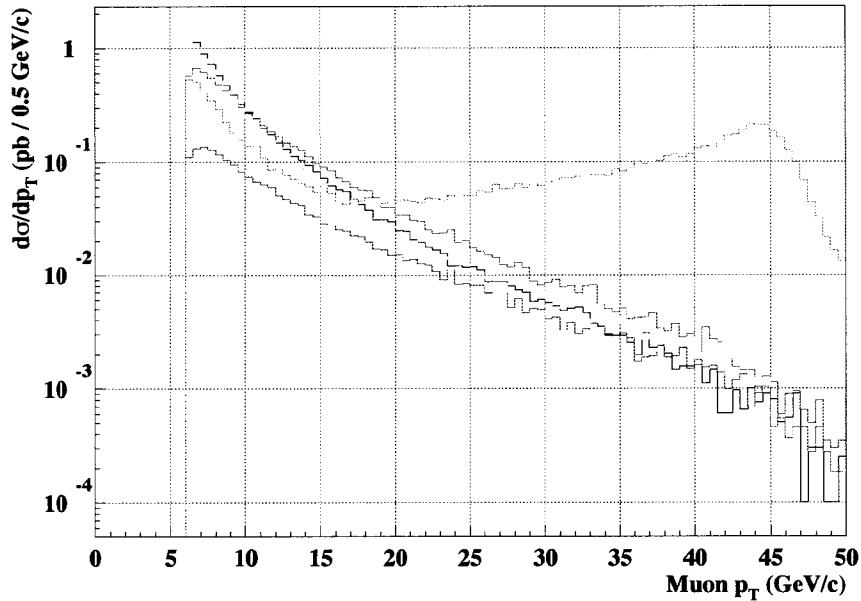


Figure 5.10: Cross section as a function of $p_T(\mu^\pm)$ from $\gamma\gamma$ interactions in ATLAS. The distributions are for elastic (black), semi-inelastic (blue), and fully inelastic (red) production via LPAIR, and elastic (green) and double pomeron exchange background (pink) from DPEMC.

of $|\phi| < 0.01$ rad and $p_T(\mu^+\mu^-) < 0.150$ GeV/c has also been applied. Although shown with arbitrary units along the vertical axis, the relative rates of muon pair production are correct since the common normalization chosen was for an equivalent integrated luminosity. The observation of muon pairs from Drell-Yan remain a serious background even after the kinematic cuts of Table 5.2 are applied with an overall cross section comparable with the $\gamma\gamma \rightarrow \mu^+\mu^-$ process itself.

Other Backgrounds

Background contributions arising due to the rescattering effects can be minimized by requiring very low total muon pair p_T , typically to less than 50 MeV/c, as well as by imposing an upper limit to the invariant mass of the muon pair, as described previously in 4.1.

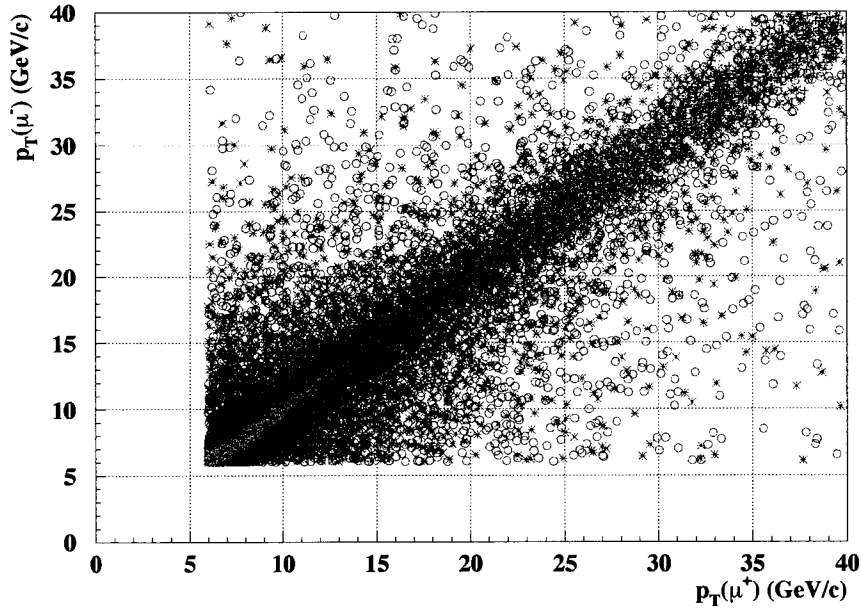


Figure 5.11: Scatter plot demonstrating the degree of correlation between the measured μ^+ and μ^- p_T measured in ATLAS. Shown are the distributions for elastic (black), semi-inelastic (blue), and fully inelastic (red) production via LPAIR, and elastic (green) and double pomeron exchange background (pink) from DPEMC.

Background Reduction with Vertex Fitting

In addition to the application of kinematic selection criteria it is also possible to apply vertex fit requirements in order to select the signal $\gamma\gamma \rightarrow \mu^+\mu^-$ events [56]. The first step is to reconstruct the $\mu^+\mu^-$ vertex from the ATLAS track parameters. Helix parameters as defined in Figure 5.13 are available for each track and include measures of $(d_0, Z_0, \phi, \cot \theta, q/p_T)$ where d_0 is the impact parameter, Z_0 is the distance of closest approach by the track to the interaction point as measured along the z axis, ϕ is the reconstructed polar angle, $\cot \theta$ represents the track θ , and q/p_T is the inverse of the measured track momentum weighted by the charge of the particle traversing the detector [59]. The vertex fit proceeds by using the Karimäki circle fitting routine [60] to reconstruct the $\mu^+\mu^-$ vertex from the smeared track parameters. The vertex reconstruction is considered good if the probability of the fit χ^2 ,

Process	$\sigma(\text{pb})$
TPHIC	25.85
LPAIR (elastic-elastic)	29.33
LPAIR (semi-inelastic)	13.67
LPAIR (inelastic)	2.82
LO QCD ($c\bar{c}$)	1.48×10^5
LO QCD ($b\bar{b}$)	4.16×10^5
Drell-Yan ($c\bar{c}$)	199.7
Drell-Yan ($b\bar{b}$)	220.1
Drell-Yan ($\mu^+\mu^-$)	1127.2
Drell-Yan ($\tau^+\tau^-$)	268.6

Table 5.3: Expected cross sections at the LHC for two photon production of $\mu^+\mu^-$ pairs as well as several background processes, for the application of loose initial kinematic selection criteria.

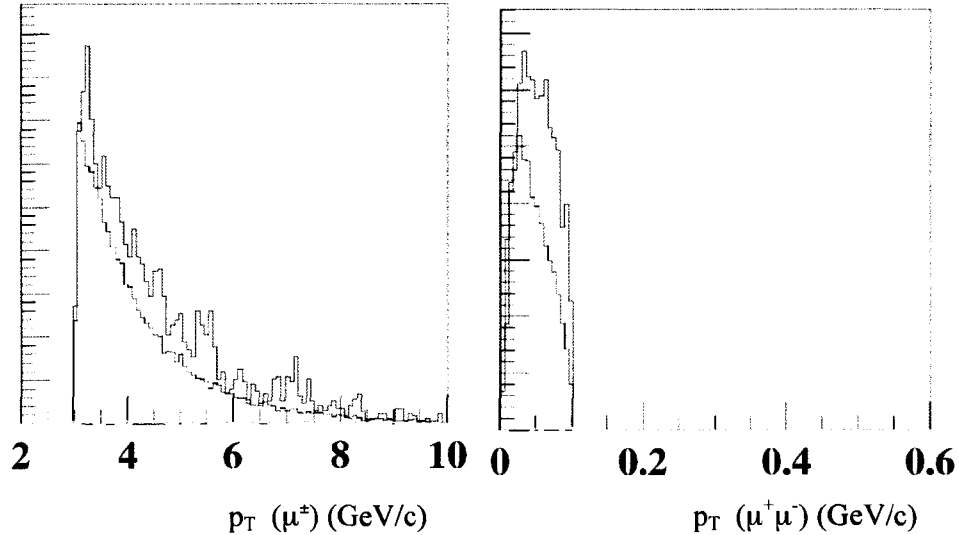


Figure 5.12: Relative cross section as a function of $p_T(\mu^\pm)$ (left) and total $\mu^+\mu^-$ pair p_T (right). Shown are the distributions for the signal elastic (black), and backgrounds from Drell-Yan production of $\mu^+\mu^-$ (red) and $\tau^+\tau^-$ (green) with muonic decays. Only kinematic and no vertex fit criteria have been applied.

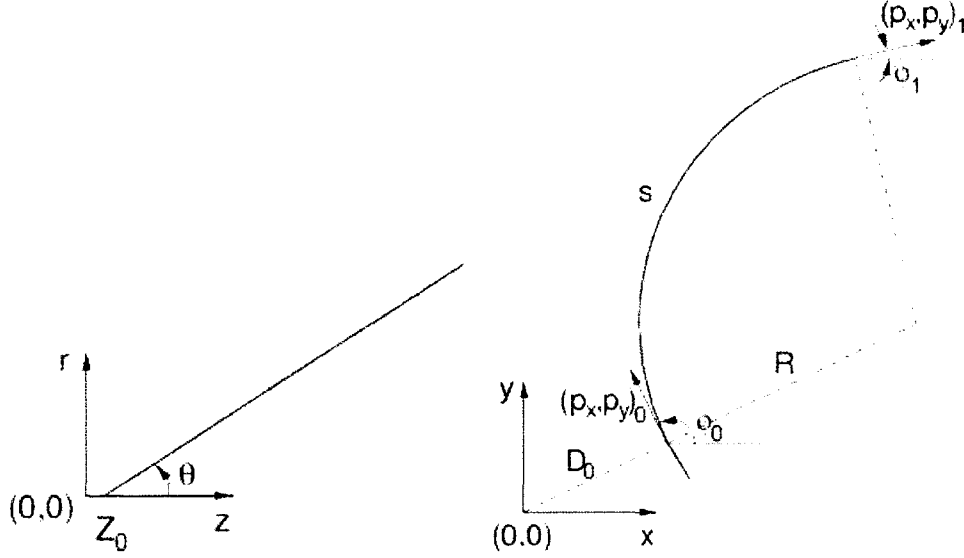


Figure 5.13: Definition of the impact parameter d_0 and Z_0 based upon the track helix parameters.

$Pr(\chi^2)(\mu^+\mu^-)$ is greater than 0.1. This quality of fit is required of the $\mu^+\mu^-$ pairs from either signal or background events.

In order to separate signal from background a three track vertex fit is performed utilizing the $\mu^+\mu^-$ along with any other tracks that pass within $2\sigma(Z_0)$ of the reconstructed $\mu^+\mu^-$ vertex. A good three track fit where $Pr(\chi^2(\mu^+\mu^- + \text{track})) > 0.1$ is chosen to identify the event as a Drell-Yan background event. A poor three track vertex fit where $Pr(\chi^2(\mu^+\mu^- + \text{track})) < 0.1$ is chosen to identify the event as the signal two photon event.

To realistically simulate the environment at the LHC the event primary vertex for all events is smeared according to the LHC beam profile. The spread of the beam was assumed to be $R_{rms} = 16\mu\text{m}$ radially and $L_{rms} = 7.5$ cm longitudinally along the direction of the z axis [20]. Furthermore, all signal and background events were simulated in ATLFAST both with and without the addition of pileup due to minimum bias events. The scenario of low luminosity, originally planned as $L = 10^{33}\text{cm}^{-2}\text{s}^{-1}$, at the LHC was considered.

Table 5.4 lists the expected cross sections at the LHC for the production of $\mu^+\mu^-$ pairs from two photon interactions as simulated with two different $\gamma\gamma$ generators based upon the application of the tight kinematic cuts of Table

Process	$ \phi < 0.1$ rad $\sigma(\text{pb})$	$ \phi < 0.01$ rad $\sigma(\text{pb})$
TPHIC	14.5	14.5
TPHIC w/pileup	14.4	14.4
LPAIR	11.8	8.1
LPAIR w/pileup	11.8	8.0
LPAIR (inel-inel)	0.06	0.02
LPAIR (inel-inel) w/pileup	0.05	0.01
LPAIR (inel-el)	0.63	0.20
LPAIR (inel-el) w/pileup	0.60	0.14
Drell-Yan ($\mu^+\mu^-$)	0.049	0.046

Table 5.4: Signal and background after the application of kinematic and vertex cuts.

5.2 and the $Pr(\chi^2) +$ track vertex fit. The results are available for both wide ($|\phi| < 0.1$ rad) and narrow ($|\phi| < 0.01$ rad) acoplanarity angles. Also shown are the cross sections of the Drell-Yan background process in which $\mu^+\mu^-$ pairs result, as simulated with Pythia (version 5.715) [61]. The background from Leading Order QCD are insignificant and not included in Table 5.4. The combination of kinematic and vertex fit criteria strongly suppresses the contribution from the various background processes relative to the two photon production of $\mu^+\mu^-$ pairs. In addition to reduction of backgrounds from Drell-Yan and QCD, the identical vertex fit requirement is also helpful when looking to identify two photon events in the case of pileup of minimum bias events at the LHC.

5.1.5 Absolute Luminosity calculation and uncertainty

From equation 4.16 the rescattering corrections of [27] can be viewed as negligible by either fitting the acoplanarity distribution ϕ , which automatically suppresses the rescattering correction, or by requiring that the p_T of the muon pair system be less than 50 MeV/c. With this requirement the rescattering correction will be less than 0.13% of the measured elastic cross section which is estimated from the LPAIR Monte Carlo to be 0.775 ± 0.008 pb, given an identical requirement on the p_T of the muon pair. The corresponding cross

sections for the semi-elastic and fully inelastic cases can be found in Table 5.5. The cross section for each of these three processes is shown in Figure 5.14 as a function of the measured acoplanarity angle. The semi-elastic and inelastic backgrounds are approximately 1% of the signal elastic production of $\gamma\gamma \rightarrow \mu^+\mu^-$. Therefore any measurement of the delivered luminosity based upon the observation of the two photon interaction events will only be limited by the size of the statistical sample collected, as well as any systematic uncertainties for the triggering and identification of the $\mu^+\mu^-$ pair. As discussed in 5.1.2 the ATLAS HLT is expected to be 90% efficient for muons of $p_T > 7$ GeV/c. Although the rescattering correction has the lowest selection efficiency, it has the advantage of greatly reducing the level of uncertainty arising from systematic errors associated with the theoretical understanding and fitting of the semi-elastic and inelastic backgrounds. Therefore the statistical size of the event sample is reduced at the sacrifice of minimizing the rescattering correction.

Additionally the choice of model used to calculate the two photon exchange process (either EPA or the matrix element calculation) will contribute somewhat to the level of uncertainty. For example, within the region of $p_T(\mu^+\mu^-) < 0.050$ GeV/c used to ensure a minimal contribution from the rescattering processes, the LPAIR predicted cross section is nearly twice that of DPEMC which is based upon the EPA. However it should be noted that the EPA is as named, an approximation for the two photon interaction process that is directly obtainable from the precise matrix element calculations [62]. Therefore the predictions based upon the LPAIR Monte Carlo have a more extensive background of use by other experiments including H1 and ZEUS at HERA.

5.2 Electron pair production

In addition to the production of $\mu^+\mu^-$ pairs from two photon collisions, the possibility of utilizing the observation of e^+e^- pairs for luminosity measurement has also been studied within ATLAS [16, 63]. For such events the

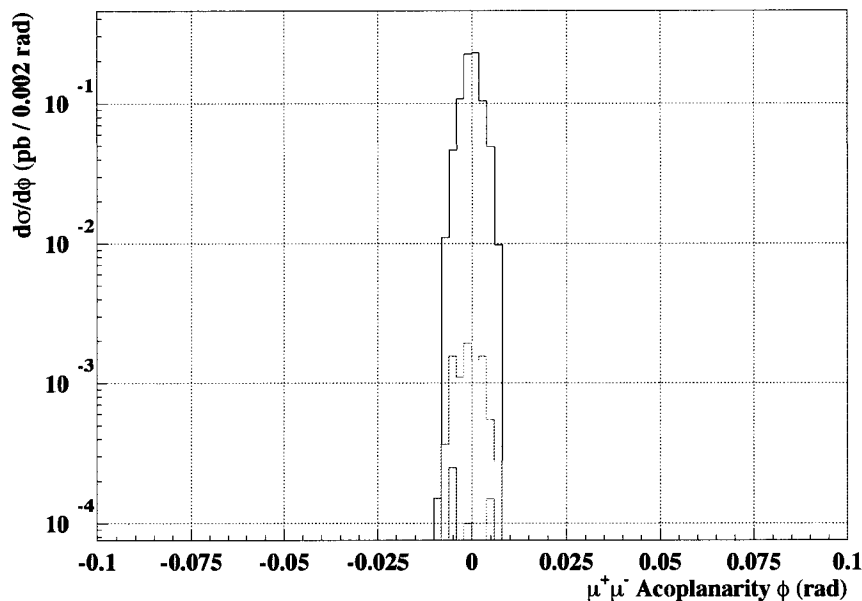


Figure 5.14: Cross section as a function of acoplanarity angle ϕ for the muon pair produced from $\gamma\gamma$ interactions in ATLAS requiring $p_T(\mu^+\mu^-) < 0.050$ GeV/c in order to suppress the rescattering correction to the cross section. Shown are the distributions for elastic (black), semi-inelastic (blue), and fully inelastic (red) production via LPAIR.

e^+e^- pair is produced with very small values of invariant mass, typically of the order of the electron mass, and pair transverse momentum. Furthermore the e^+e^- pairs are produced at near-zero polar angle θ . Therefore any such measurement would require the presence of an analysing dipole magnet to be installed in ATLAS approximately 15 m from the interaction point so as to deflect the e^\pm into separate detectors outside the LHC beamline. Although studies have shown that a large cross section of nearly $2\mu b$ could be expected in such a setup it would only be able to function during collisions where the luminosity would be less than $10^{33}\text{cm}^{-2}\text{s}^{-1}$. This is due to the requirement of no other charged particles within $|\eta| < 7.6$ as part of the event selection criteria [16].

As has been shown in Section 5.1 the production of $\gamma\gamma \rightarrow \mu^+\mu^-$ should be observable at ATLAS even with luminosities greater than $10^{33}\text{cm}^{-2}\text{s}^{-1}$ where pileup of minimum bias events will occur. Furthermore it has the additional

Process	$\sigma(\text{pb})$
LPAIR (el-el)	0.775 ± 0.008
LPAIR (inel-el)	$(8.7 \pm 3.8) \times 10^{-3}$
LPAIR (inel-inel)	$(6.4 \pm 1.8) \times 10^{-3}$

Table 5.5: Signal and background cross sections from LPAIR after the application of the cut requiring $p_T(\mu^+\mu^-) < 50 \text{ MeV}/c$ so as to appropriately neglect the rescattering correction.

advantage of making use of the existing ATLAS detector infrastructure without modification.

Chapter 6

Two Photon Interactions at CDF

In this chapter a detailed description is given of a preliminary search undertaken for the exclusive production of $\mu^+\mu^-$ pairs from two photon interactions at the CDF Experiment. A brief summary is given of the Fermilab accelerator complex and the process by which the 1.96 TeV centre of mass collision energy is achieved for the counter rotating proton and antiproton beams. This is followed by a description of the CDF Experiment in terms of the subdetectors particularly relevant to the search for exclusive $\mu^+\mu^-$ events.

The expected signatures of the two photon to $\mu^+\mu^-$ events are then reviewed based upon Monte Carlo simulations. These simulations are then checked through the analysis of a large diffractive physics dataset collected at CDF in 2004-5. Following a brief description of the CDF trigger conditions used to create the diffractive dataset, a multi-step procedure is outlined by which the dataset is scanned for exclusive muon pairs. The general characteristics of a preliminary set of candidate events are reviewed and compared directly with simulation. Finally, a brief summary will be made of the associated search for $\gamma\gamma \rightarrow e^+e^-$ that has also been underway at CDF.

6.1 The Tevatron

The Tevatron accelerator is located at Fermi National Accelerator Laboratory (Fermilab) in Batavia, Illinois near Chicago and is presently the world's

highest energy collider. At the Tevatron proton antiproton collisions occur at a centre of mass energy of 1.96 TeV. Run II of the Tevatron began in 2001 following 5 years of upgrades to both the accelerator complex and the two detectors located around the Tevatron ring. Figure 6.1 sketches the components of the Fermilab accelerator complex. The final energy of 980 GeV per beam is achieved in several steps for both the proton and antiproton beams. Table 6.1 lists some of the important characteristics of the Tevatron accelerator.

The first stage proceeds with the production of H^- ions in the Cockroft-Walton electrostatic accelerator which accelerates the ions to an energy of 750 keV. These ions are then transferred to the 150 m long linear accelerator (Linac). Radio frequency cavities are used to accelerate the ion beam to an energy of 400 MeV at the end of the Linac, at which point the beam passes through a Carbon foil which strips the electrons from the Hydrogen ions. The resulting proton beam is further accelerated by the Booster synchrotron accelerator to an energy of 8 GeV and are subsequently transferred to the Main Injector. Within the Main injector several functions occur. First, the 8 GeV protons from the Booster are accelerated to an energy of 150 GeV. Second, a portion of the 8 GeV protons are accelerated to 120 GeV and directed to the Target Station. Third, the Main Injector accelerates 8 GeV antiprotons to 150 GeV. Fourth, the Main Injector injects the 150 GeV proton and antiproton beams into the Tevatron.

At the Target Station the incoming 120 GeV proton beams are directed upon a Nickel target thereby producing antiprotons. Approximately 20 antiprotons are produced for every million protons incident upon the target. The antiprotons are separated from other particles using magnets and sent to the Debuncher which reduces the spread in momentum of the antiprotons. The antiproton beam then enters the Accumulator storage ring where they are collected until a sufficient number have been achieved. This procedure requires approximately 15 hours to accumulate 1.3×10^{12} antiprotons which are needed to achieve the desired collision luminosity. Within the Accumulator the antiproton beams undergo the process of stochastic cooling [64] in order to reduce both the longitudinal and transverse momentum spread of the beam.

FERMILAB'S ACCELERATOR CHAIN

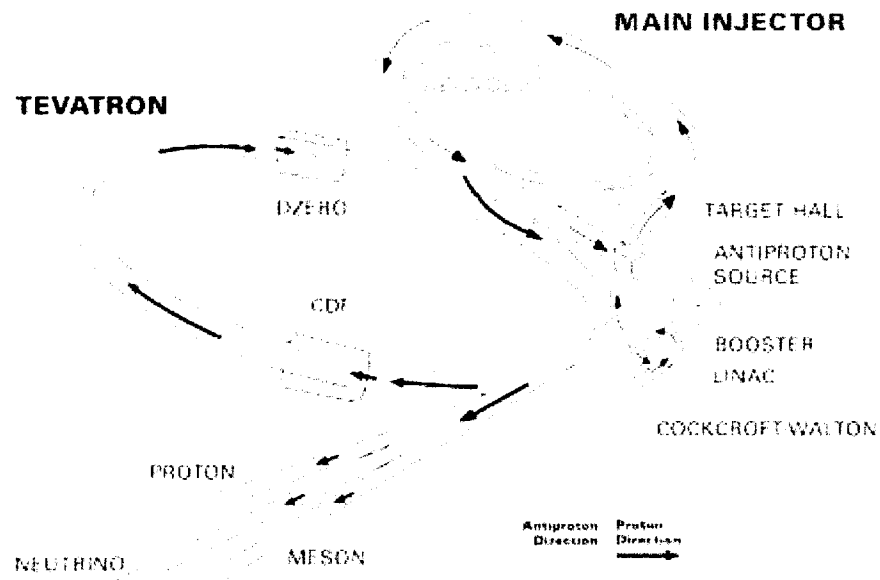


Figure 6.1: Schematic representation of the accelerator complex at Fermilab which provides the proton antiproton collisions to the Tevatron experiments CDF and D0.

When the appropriate beam conditions have been achieved the antiprotons are then transferred to the Main Injector where they are accelerated to 150 GeV in preparation for injection into the Tevatron. The Tevatron is a superconducting synchrotron 6.3 km in circumference that accelerates the proton and antiproton beams to their final energy of 980 GeV. The approximately 1000 superconducting dipole magnets around the Tevatron provide a 4.2 T field used to steer the electrostatically separated beams around the ring.

The counter-rotating beams are organized into 36 bunches each and are brought into collision at two points around the Tevatron ring. It is at these two collision points that the CDF and D0 experiments are situated. The proton and antiproton bunches cross at a given interaction point every 396 ns with a typical Tevatron fill (store) normally lasting up to 30 hours. The peak in the delivered instantaneous luminosity is at the beginning of a store.

Accelerator parameter	Run II
$p \times \bar{p}$ bunches	36×36
Number of p per bunch	2.6×10^{11}
Number of \bar{p} per bunch	3.5×10^{10}
Beam energy [GeV]	980
Luminosity [$\text{cm}^{-2}\text{s}^{-1}$]	8×10^{31}
Bunch crossing time [ns]	396
Number of interactions per crossing	2.3

Table 6.1: Accelerator parameters of the Fermilab Tevatron.

6.1.1 The CDF Detector

The upgraded Collider Detector at Fermilab (CDF II) [65, 66] is a general purpose solenoidal detector centered around the beamline with considerable flexibility and complexity. The detector consists of multiple subsystems which are designed for the measurement of charged particle trajectories and energies.

At CDF the direction of the z axis is taken along the beamline in the direction of the protons, the x axis is in the same horizontal plane as the Tevatron ring and points outward, and the y axis is directed vertically. The cylindrical coordinates (r, ϕ, θ) more intuitively correspond to the CDF detector layout and are commonly used. In general the polar angle is replaced by the pseudorapidity defined as $\eta = -\frac{1}{2} \ln(\tan \theta)$ since the partonic level centre-of-mass energy is unknown at $p\bar{p}$ colliders. The value of η is taken relative to the location of the primary interaction vertex.

Tracking System

The charge and momentum of a track within CDF is measured from the curvature of the track within the 1.4 T solenoidal magnetic field that surrounds the tracking system. The magnetic field is aligned along the beam axis and is produced by a 5 m long superconducting solenoid. The transverse momentum of a reconstructed track, in units of GeV, can be calculated from the relation

$$p_T = 0.3 B q r \quad (6.1)$$

where B is the strength of the magnetic field (T), q is the charge of the

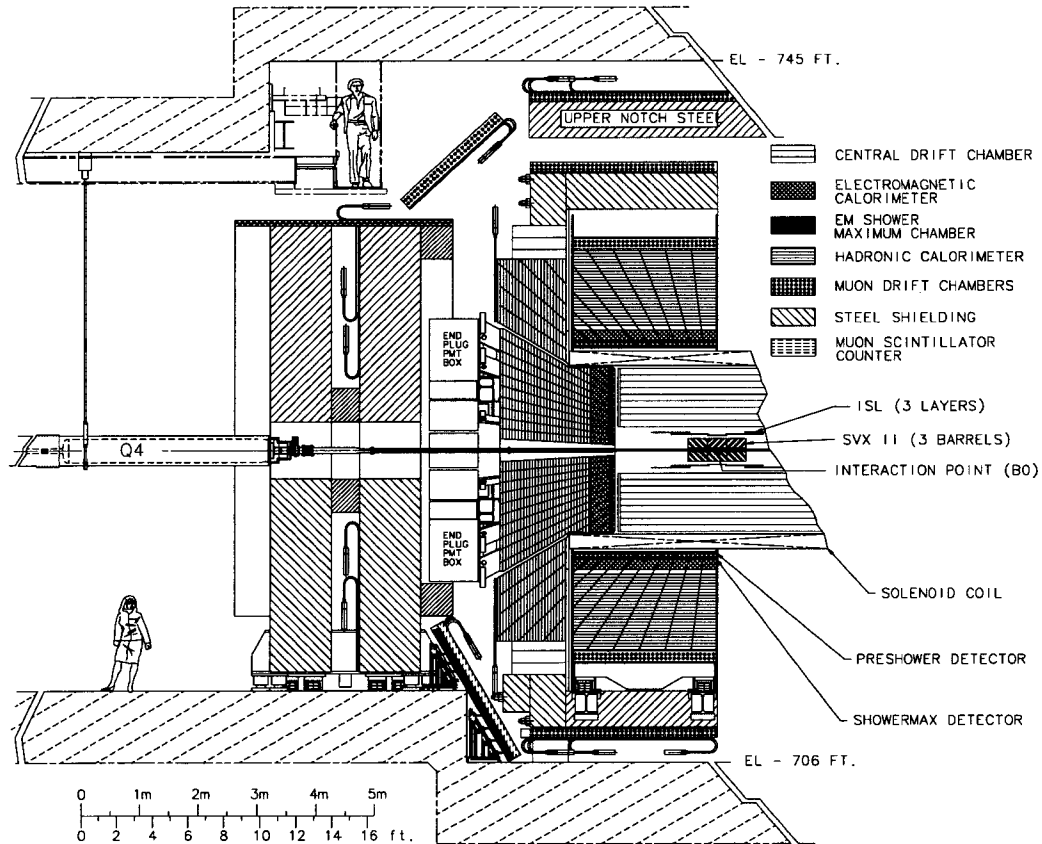


Figure 6.2: Cross sectional elevation view of one half of the CDF detector at FNAL. The other half of the detector is mirror symmetric to the shown layout.

particle (units of e) and r is the measured radius of curvature (m).

The CDF tracking system consists of a silicon micro-strip detector closest to the beamline and surrounded by an open-cell wire drift chamber known as the Central Outer Tracker (COT). The silicon detector provides tracking information out to $|\eta| < 2.0$. The COT consists of eight super-layers (SL) each 3.10 m in length covering the radial region between 40 and 132 cm from the beam axis. A gas mixture of 60% argon and 40% ethane is used within the COT. Each SL has 12 layers of sense wires strung between alternated layers of potential wires. Within four of the SL the wires run parallel to the beam axis and provide track reconstruction in the transverse plane (axial layers). The remaining four SL are at a ± 2 degree angle with respect to the beam axis and provide stereo information for the reconstruction along the z axis. The two

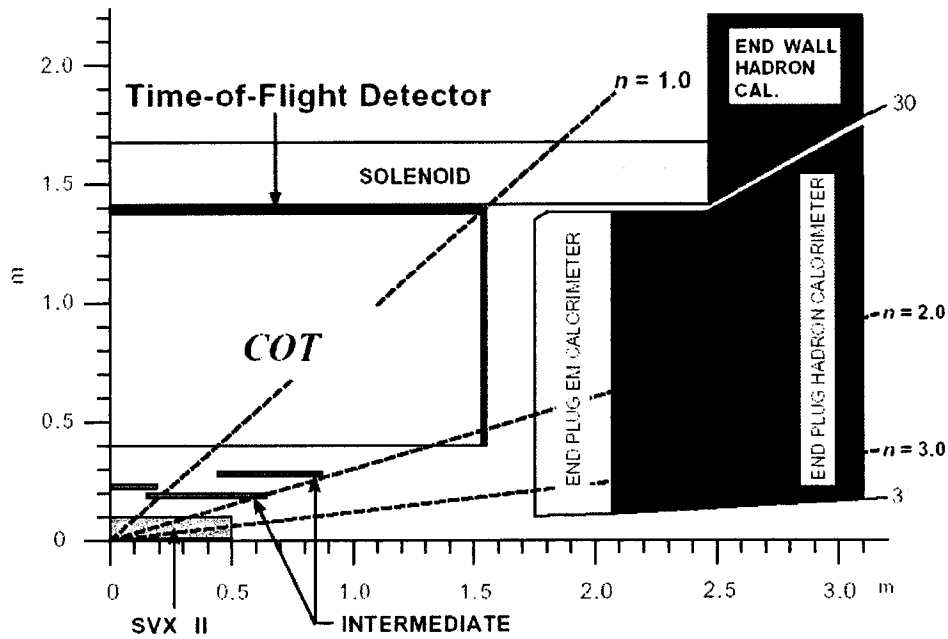


Figure 6.3: Schematic of the CDF tracking system.

types of SL are alternated such that a stereo layer is at the innermost radius. Figure 6.3 presents a schematic of the CDF tracking system and the spatial relation between the COT and the other CDF subdetectors. The momentum resolution of the COT detector has been measured to be $\frac{\sigma_{p_T}}{p_T} = 1.7 \times 10^{-3}$ with units of $[\text{GeV}/c]^{-1}$.

Calorimeter System

The calorimeter system of CDF is a sampling calorimeter with scintillator as the active material arranged between sheets of lead and steel absorber and can be logically arranged into two sections being the central calorimeter ($0 < |\eta| < 1.1$) and forward plug calorimeter ($1.1 < |\eta| < 3.6$). The central calorimeter is arranged into 48 azimuthal wedges each covering 15 degrees in ϕ . Within each wedge are grouped 10 calorimeter readout towers with projective geometry pointing back to the primary vertex. Also within each wedge is an inner electromagnetic (CEM) and outer hadronic (CHA/WHA) section. The CEM is comprised of 31 layers of 0.125 cm thick lead interleaved with 5.0 mm of polystyrene scintillator, and for the CHA there are 32 layers of 2.5 cm steel

Calorimeter Name	Calorimeter Type	Energy Resolution [GeV]
CEM	Electromagnetic	$14\%/\sqrt{E_T}$
PEM	Electromagnetic	$16\%/\sqrt{E}$
CHA	Hadronic	$75\%/\sqrt{E}$
WHA	Hadronic	$80\%/\sqrt{E}$
PHA	Hadronic	$80\%/\sqrt{E} + 5\%$

Table 6.2: Measured energy resolutions for the electromagnetic and hadronic calorimetry system of CDF.

interleaved with 1.0 cm scintillator.

The forward plug calorimeter consists of scintillator tiles readout via wavelength shifting fibers embedded in the scintillator and also consists of electromagnetic (PEM with 23 layers of 0.45 cm lead interleaved with 4.0 mm of scintillator) and hadronic (PHA with 23 layers of 2.5 cm steel interleaved with 1.0 cm of scintillator) components. Finally, within the electromagnetic component of each calorimeter wedge are situated proportional chambers used to measure the profile of the electromagnetic showers, thereby enabling the system to accurately identify the location of the incident particle within the calorimeter tower.

In total there are about 480 readout towers within the Central Calorimeter covering an area of 0.1×15 degrees in $\eta \times \phi$ space. A similar number of towers exist for the Forward Plug calorimeters with each tower covering an angle of 7.5 deg or 15 deg in ϕ with variable coverage in η . From test beam data with electrons and single pions the energy resolution of the electromagnetic and hadronic calorimeters was measured and is presented in Table 6.2.

Muon System

The CDF muon system is located directly behind the calorimeter modules and as such the minimum p_T required to reach the muon system varies between 1.4 and 2.2 GeV/c depending upon the amount of material traversed. The overall system consists of four independent systems of proportional wire chambers and scintillators. The Central Muon detector (CMU) and Central Muon Upgrade detector (CMP) both cover $|\eta| < 0.6$ and is the principle muon

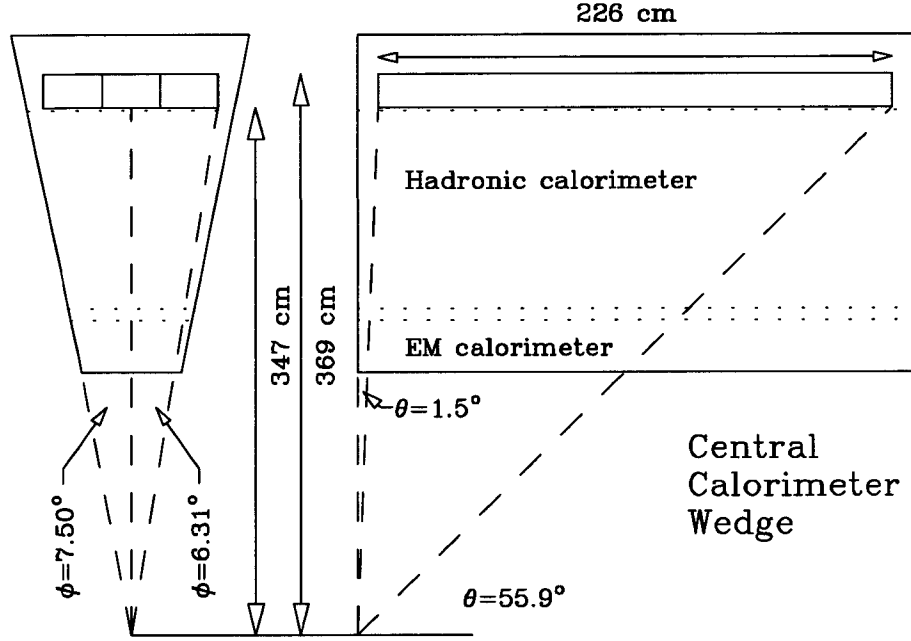


Figure 6.4: Schematic of the CMU chambers at the outer edge of each Central Calorimeter Wedge.

detector system used in this analysis. The CMU units consist of four rectangular drift chambers filled with an argon/ethane gas mixture with sense wires that are $50 \mu\text{m}$ in diameter and run parallel to the beam axis. The hit positions in the drift cells are determined from the drift time of the ions to the wire as the traversing muon ionizes the gas in the chambers. Figure 6.4 provides a schematic of the CMU chambers located behind each calorimeter wedge.

Other muon system detectors include the Central Muon Extension (CMX) which covers the region of $0.6 < |\eta| < 1.0$, and the Barrel Muon Upgrade detector (BMU) which provides coverage within $1.0 < |\eta| < 1.5$. Finally a set of chambers (CMP) identical to those used in the CMU but staggered by half a cell per chamber are located directly behind 60 cm of steel and form a rectangular box around CDF. The CMP aids the CMU in further improving the purity of muon identification.

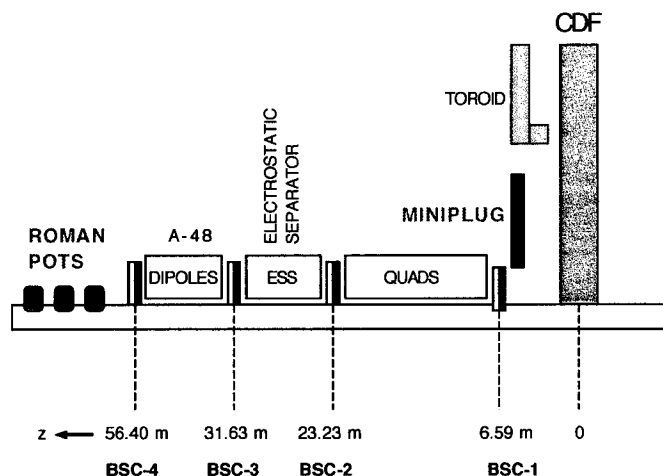


Figure 6.5: Schematic of the beam shower counter (BSC) locations on the West side of CDF. The BSC arrangement on the East side is mirror symmetric but does not include BSC-4 or the Roman Pots.

Beam Shower Counters

Located along the beampipe at various distances from the interaction point are a series of scintillation counters known as Beam Shower Counters (BSC). The BSC are positioned around the beampipe and are used to detect particles close to the beampipe for both diffractive physics and beam loss monitoring. Four stations of BSC units (BSC-1, BSC-2, BSC-3, BSC-4) are progressively located further away from the interaction point and are symmetrically positioned on both the east and west sides of CDF. However, BSC-4 is only on the west side. Together the BSC provide coverage over the pseudorapidity range of $5.4 < |\eta| < 7.5$. Figure 6.5 shows the relative locations of the BSC stations on the west side of CDF. The BSC are used as a veto in the selection of diffractive events which require rapidity gaps as part of the CDF trigger system and aid in the rejection of most non-diffractive and multiple interaction events, while retaining almost all diffractive events. A gap trigger is activated when no BSC station has a signal above the threshold of approximately 300 ADC counts.

Cherenkov Luminosity Counter

The CLC provides coverage in the forward region of $3.75 < |\eta| < 4.75$ in both the east and west sides of CDF. Each module consists of 48 thin, long gas filled Cherenkov counters. The counters are arranged into three concentric layers, each with 16 counters, pointing to the interaction point. Each of the counters are conical in shape and constructed with 0.1 mm thick reflective aluminized mylar. The cones closest to the beampipe are 110 cm in length, while the counters in the outermost two layers are 180 cm long. The counters are mounted inside a thin aluminum pressure vessel filled with isobutane which acts as the Cherenkov radiator. The Cherenkov light is detected using fast 2.5 cm diameter photomultiplier tubes.

Data Acquisition and Trigger

CDF employs a three level trigger system designed to select interesting physics events from the collisions which occur every approximately 400 ns. Each level of the trigger system is designed to provide sufficient rejection that will enable the collisions to be reduced to a more acceptable final rate that can be subsequently written to storage.

The first level of trigger (Level-1) is built from custom hardware and is highly optimized for speed. The Level-1 system makes a decision of whether an event should be accepted based upon preliminary information from the calorimeters, tracking system and muon chambers. This Level-1 decision to either accept or reject the event must be made within $6 \mu\text{s}$. This in turn reduces the data rate from 2.5 MHz to a maximum of 20 kHz at the output of the Level-1.

Event data passing the Level-1 trigger are read into the event buffers while the second level trigger system operates. The second level trigger (Level-2) is a set of programmable logic devices used to reconstruct calorimetric clusters and simple tracks. The Level-2 also has access to the silicon tracker information at this stage, and must provide a decision within $50 \mu\text{s}$, thereby reducing the event data rate to 300 Hz which is then passed to the final trigger level of CDF

(Level-3).

The CDF Level-3 trigger system consists of a farm of approximately 300 Linux computers which are able to analyse and fully reconstruct each event. Events which pass the final trigger stage are written out to permanent storage at a maximum rate of 80 Hz, equivalent to 20 MBytes per second. In addition, the data is also made available to the monitoring system in order to ensure the proper functioning of the detector and trigger system during the store. This enables the shift crew to document any special running conditions for the data collected.

Detector Simulation and Data Analysis

The CDF detector simulation [67] is based upon the GEANT3 program [68] written in Fortran and provides a detailed simulation of the detector materials, geometry, readout and trigger system. The detector simulation takes event generator samples as input. It is the event generators that simulate the physics process of interest and provides the particle-level information to the GEANT3 simulation. The format of the real and simulated data samples is identical following the real-time and offline reconstruction processing.

6.2 Search for Two Photon Production of Exclusive $\mu^+\mu^-$ Events

The search for the exclusive production of $\mu^+\mu^-$ pairs from two photon collisions at the Fermilab Tevatron is described below. Given the earlier discussion regarding the applicability of this process for luminosity measurement at the LHC, it was therefore considered appropriate to perform a first stage study of these events at a currently operating hadron collider such as the Fermilab Tevatron. The availability of a diffractive physics dataset recently collected at CDF will present a useful study in preparation for observing di-muon production from two photon interactions at the LHC.

6.2.1 Simulation Results

The LPAIR Monte Carlo generator was used to simulate elastic, semi-elastic and fully inelastic two photon production of $\mu^+\mu^-$ pairs at CDF. These muon pair samples are based upon particle level simulation only as the event files have not yet been passed through the CDF full detector simulation program. Typical characteristics of the events include: low invariant mass ($< 10 \text{ GeV}/c^2$), small total pair transverse momentum ($< 0.5 \text{ GeV}/c$), and small near zero acoplanarity angle ϕ .¹ Individual muons must also have a $p_T > 1.5 \text{ GeV}/c$ in order to reach the muon detector system at the outer portions of CDF. For each of the three samples the following general criteria were applied so as to understand the characteristics of each event type relative to each other as well as with respect to other potential backgrounds. The basic applied criteria included the requirement that both muons must have $p_T(\mu^\pm) > 1.5 \text{ GeV}/c$ within $|\eta| < 1.0$, and that the measured acoplanarity angle ϕ be less than 0.1 rad.

Shown in Figure 6.6 (top) are the predicted cross sections as a function of p_T for the elastic (black), semi-elastic (blue) and fully inelastic (red) two photon production of $\mu^+\mu^-$ events at CDF. The elastic cross section exceeds that of the other two processes at low p_T and $M(\mu^+\mu^-)$ but become comparable in the region above 7 GeV/c and 15 GeV/c², respectively. The simulated distributions of $\mu^+\mu^-$ invariant mass also follow the same general trend, with the cross section of the elastic production dominant at low values as shown in Figure 6.6 (bottom).

As was demonstrated from the analysis of two photon production of $\mu^+\mu^-$ at ATLAS provided in Chapter 5, the acoplanarity angle ϕ is able to provide a very strong signature of the elastic interaction. The ϕ distribution is shown in Figure 6.7 (top) with the elastic peak centered at zero and a cross section nearly a factor of ten larger than the approximately flat distribution from the fully inelastic process. The cross section values due to the semi-elastic are

¹A reminder that ϕ is defined as the angular difference of two tracks from being back-to-back (180 degrees) in the plane transverse to the beam axis. See Figure 5.1 for a visual description of acoplanarity.

well below the threshold shown in Figure 6.7.

Another strong signature of the elastic di-muon production is the distribution of the ratio of μ^+ to μ^- transverse momenta as shown in Figure 6.7 (bottom). For all three processes the magnitude of the muon p_T values are typically balanced. However, for the elastic case the distribution is much narrower compared to the backgrounds. The balanced nature of the elastically produced muon pair is further evident from the distribution of the difference in transverse momentum of Figure 6.8 (top). A good demonstration of the elastic event characteristics is evident from a plot of the correlation between μ^+ and μ^- p_T values. The elastically produced leptons are much more tightly correlated in transverse momentum, as shown in Figure 6.8 (bottom), with large deviations occurring for the semi-inelastic and inelastic cases.

In Chapter 4.1, it was identified that the total $\mu^+\mu^-$ pair transverse momentum of Figure 6.9 (top) can be used to restrict the contributions to the process cross section coming from (semi-)inelastic events, as well as the rescattering effects that can occur between the proton and antiproton following the photon emission. By applying an upper limit on the total pair p_T as defined in Equation 4.16 it is then possible to neglect the rescattering corrections. For example, restricting the p_T sum to less than 50 MeV/c aids to suppress the inelastic backgrounds by nearly a factor of 200.

Finally, the elastic events are clearly visible above the background of semi-inelastic and inelastic events when considering the distribution of acoplanarity angle ϕ as a function of the transverse momentum ratio in Figure 6.9 (bottom). The signal elastic events (black) peak about an acoplanarity angle of zero radians, and are well visible above the background in the region of $0.90 < p_T(\mu^+)/p_T(\mu^-) < 1.10$.

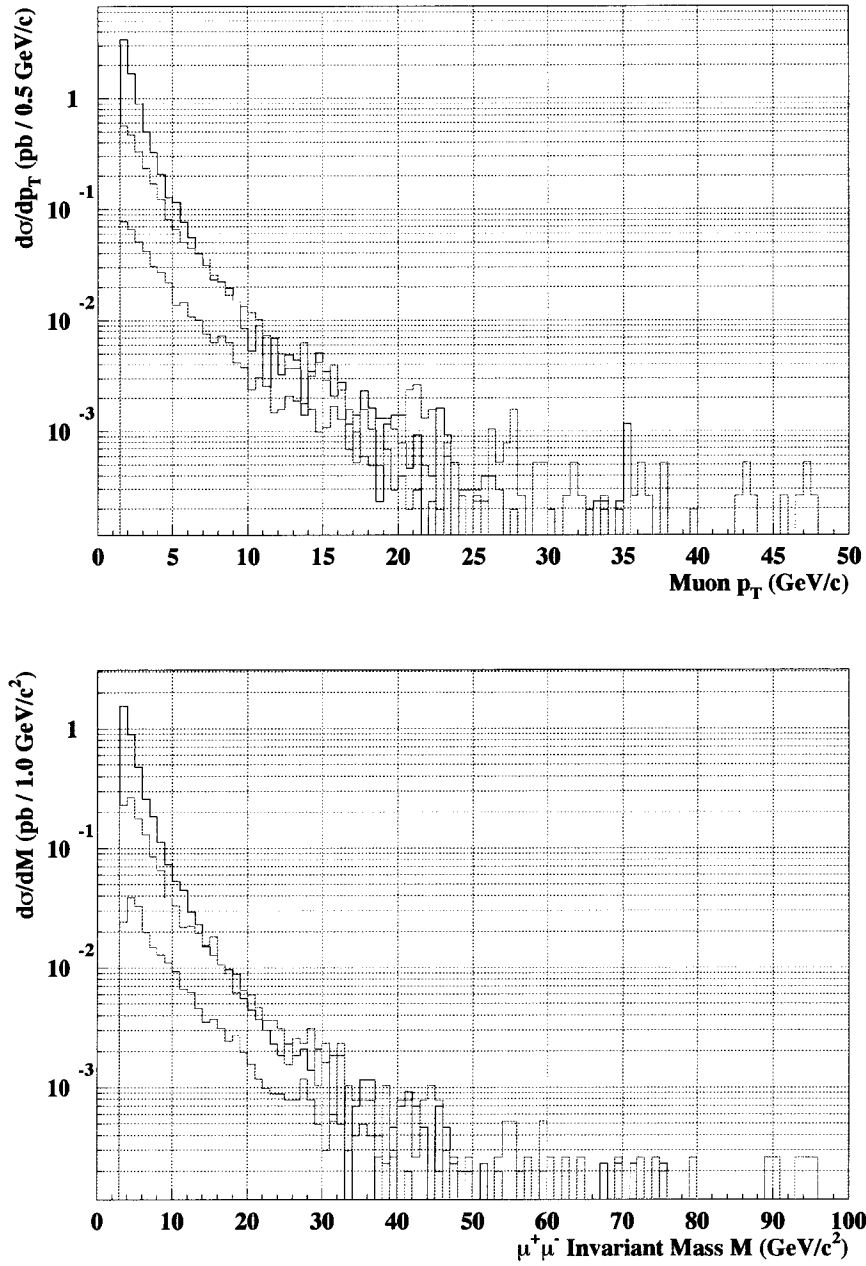


Figure 6.6: Cross section as a function of transverse momentum of the produced muons (top) and invariant mass (bottom) of the $\mu^+\mu^-$ pair from two photon interactions in CDF. Shown are the distributions for elastic (black), semi-inelastic (blue), and fully inelastic (red) events simulated with LPAIR.

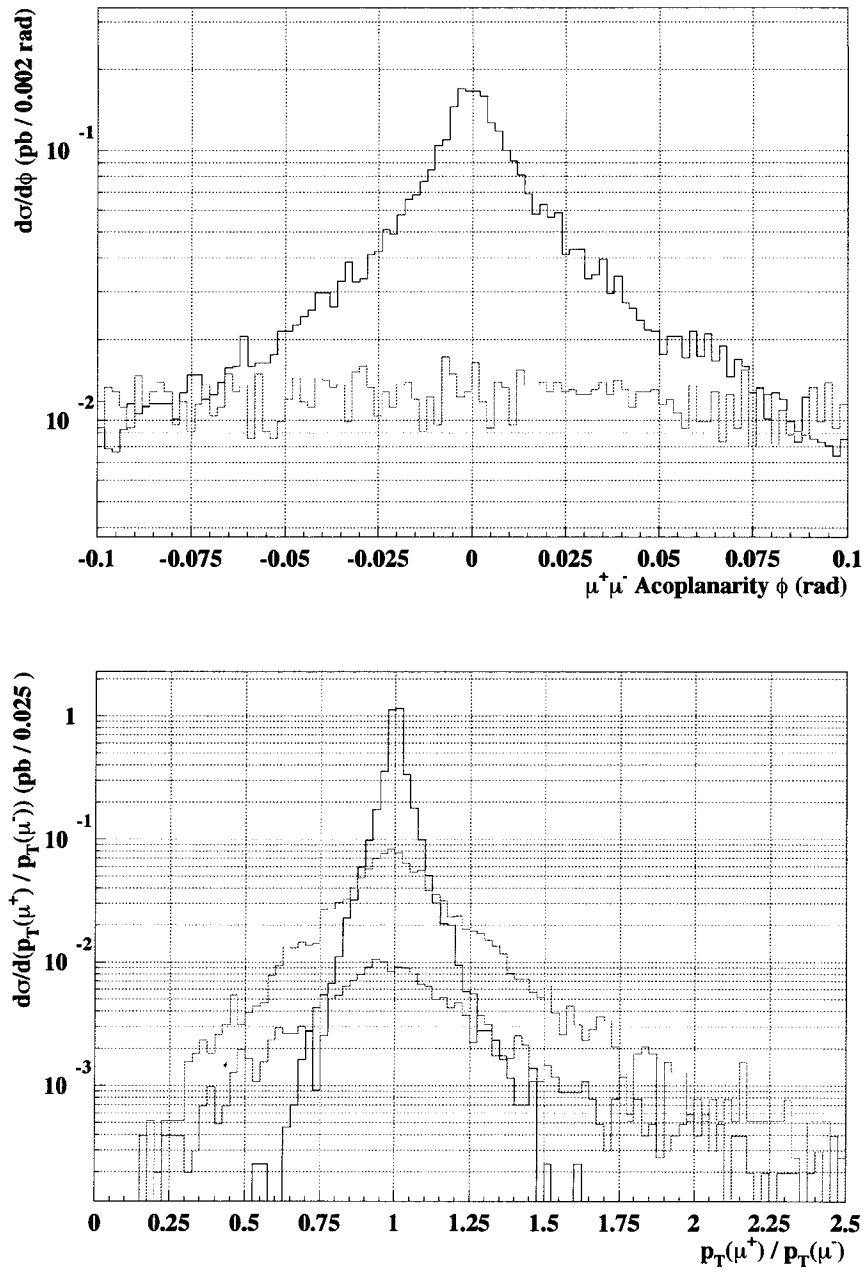


Figure 6.7: Cross section as a function of the acoplanarity angle ϕ (top) and the ratio of the muon transverse momentum values (bottom) from two photon interactions at CDF. Shown are the distributions for elastic (black), semi-elastic (blue), and fully inelastic (red) events simulated with LPAIR.

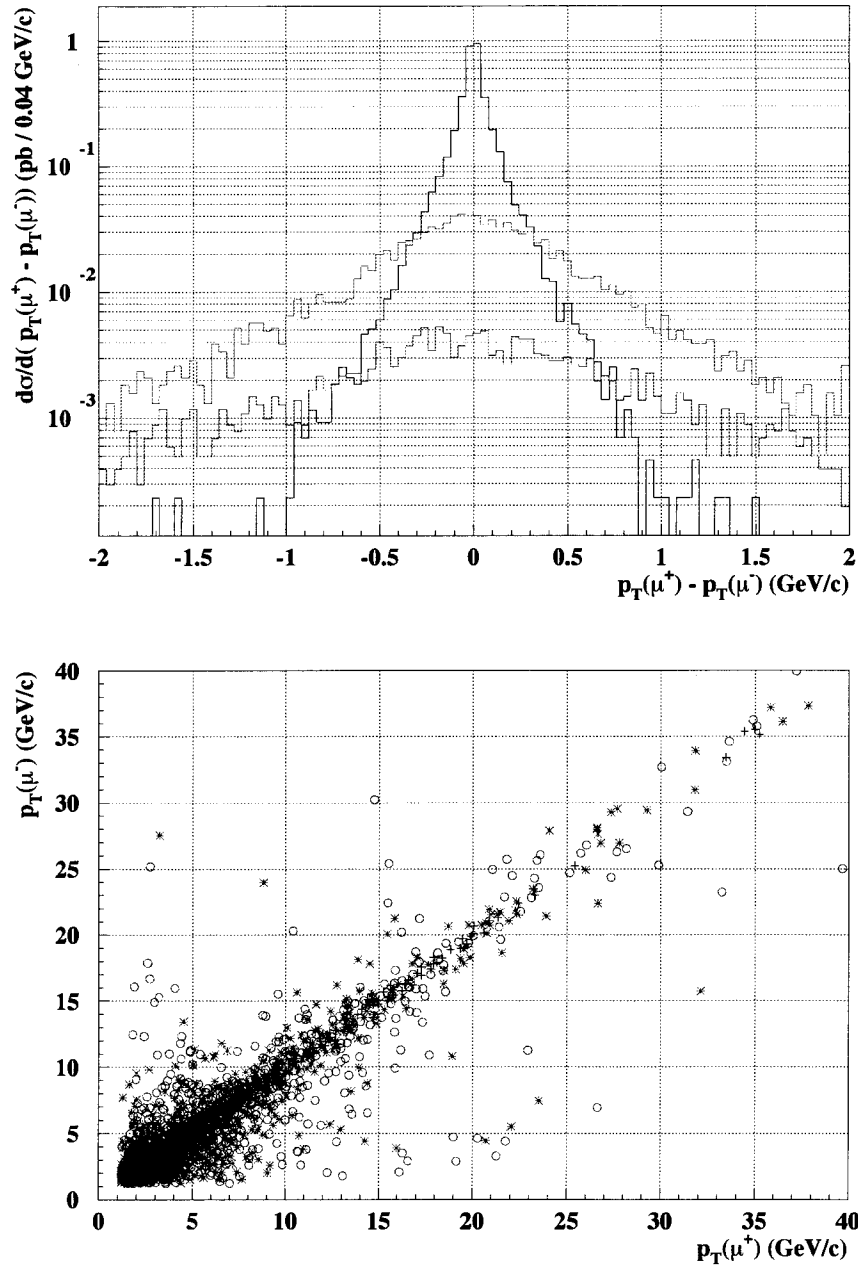


Figure 6.8: Cross section as a function of p_T difference between muons (top) and a scatter plot demonstrating the predicted correlation between the transverse momenta of the produced muons (bottom) from two photon interactions in CDF. Shown are the distributions for elastic (black), semi-inelastic (blue), and fully inelastic (red) events simulated with LPAIR.

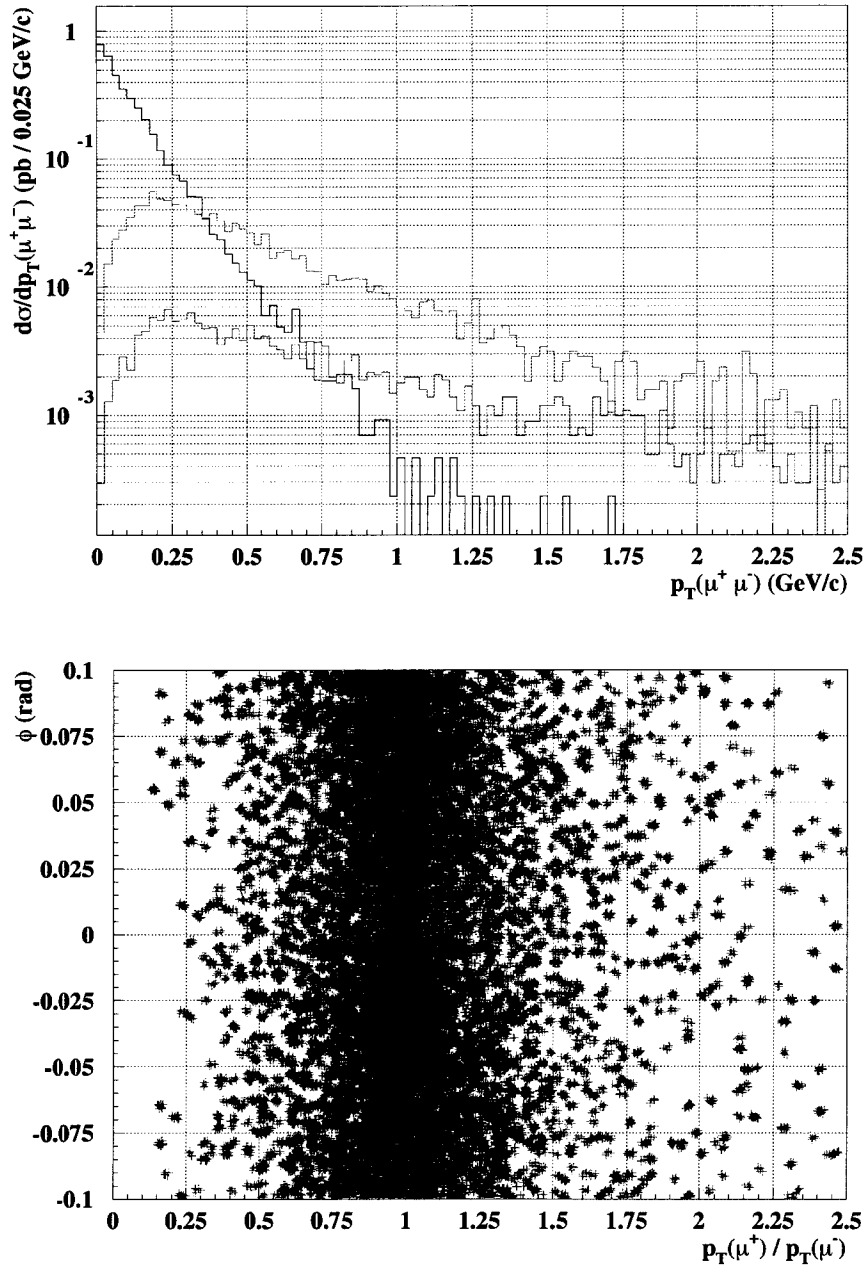


Figure 6.9: Cross section as a function of pair transverse momentum $p_T(\mu^+\mu^-)$ (top) along with the relationship between the acoplanarity angle ϕ and the ratio of the muon transverse momentum (bottom) from two photon interactions in CDF. Shown are the distributions for elastic (black), semi-inelastic (blue), and fully inelastic (red) events simulated with LPAIR.

Diffractive Trigger	Description
Level-1: L1_TWO_GAP CMU1.5_PT1.5[1]	One CMU muon of $p_T > 1.5$ GeV/c Rapidity gap in the East and West BSC
Level-2: L2_AUTO_L1_TWO_GAP CMU1.5PT1.5	One CMU muon of $p_T > 1.5$ GeV/c Additional track of $p_T > 1.5$ GeV/c Rapidity gap in the East and West BSC
Level-3: DIFF_CHIC CMU1.5_P1.5_PT1.5_TRK	One quality CMU muon of $p_T > 1.5$ GeV/c Invariant mass (CMU muon + Track) $2.7 < M(\mu + \text{track})[\text{GeV}/c^2] < 4.0$

Table 6.3: Trigger conditions applied in order to produce the *gdf0d* dataset.

6.2.2 Data Results

A special trigger entry was added to the CDF trigger menu in late 2004 as part of a diffractive J/ψ and χ_c study previously conducted by CDF [69, 70]. It is this dataset identified as *gdf0d* that has been used as the input sample for the search analysis of exclusive two photon production of $\mu^+\mu^-$. The CDF trigger settings used in the creation of the *gdf0d* dataset are given in Table 6.3.

The first level trigger for the *gdf0d* dataset requires the observation of a muon traversing the CMU system with a minimum p_T of 1.5 GeV/c in conjunction with rapidity gaps in both the East and West beam shower counters (BSC). Events which pass the first level trigger are then further required to possess at least one additional track (not necessarily that of a muon) having $p_T > 1.5$ GeV/c within the COT coverage of $|\eta| < 1.2$. Finally, at level three the trigger selects those events in which the observed CMU muon and the other track are of opposite charge and yield a measured invariant mass $M(\mu^\pm + \text{track})$ between 2.7 and 4.0 GeV/c².

Following the application of the above trigger criteria the data sample was available in the central CDF data file catalogue. It is at this stage that the data can be accessed for user analysis. To decrease the amount of time required to process this large data sample it was decided to produce a skimmed data set from *gdf0d* which included the application of a

first set selection criteria. The skimmed dataset was produced by extracting events from *gdf0d* in which there were a minimum of 2 fully reconstructed muons. These reconstructed muons are defined as high-level objects within the CDF StNtuple Object Oriented software framework. The total dataset included in this study is estimated to represent an integrated luminosity of $325 \pm 25 \text{ pb}^{-1}$ (statistical) $\pm 25 \text{ pb}^{-1}$ (systematic).

Offline Selection Criteria

To search for the production of exclusive $\mu^+\mu^-$ pairs from two photon collisions, a series of four offline selection cuts were applied to the *gdf0d* dataset. These post-trigger criteria can be classified into the two categories of muon and track quality cuts, and peripheral collision (two photon interaction) cuts. It is the peripheral collision criteria that focus on the characteristics of the fully elastic production of lepton pairs from $\gamma\gamma$ collisions. Each of the four selection steps applied to the *gdf0d* dataset are outlined below.

Step 1: Muon and Track Quality Requirements

Require that there be at least one pair of oppositely charged muon tracks, where all tracks have an associated track within the CMU sub-detector, where both tracks have $p_T > 1.5 \text{ GeV}/c$. Furthermore the difference of the track z_0 values must be $|\Delta z_0| < 5.0 \text{ cm}$, and additionally $CMU(\Delta X) < 30 \text{ mm}$ for each track.

The following muon quality cuts are also applied.

- χ^2 of the track within the CMU sub-detector $CmuChi2Link < 9$,
- $|\eta(\mu^\pm)| < 1.0$,
- Number of axial and stereo hits of the track within the COT $NCotHitsAx \geq 20$ and $NCotHitsSt \geq 16$,
- Each track must have a reconstructed value of $|z_0| < 60.0 \text{ cm}$ from the event primary vertex.

Step 2: Cosmic Ray Veto

Apply a veto against the presence of cosmic rays. An event is tagged as containing a cosmic ray if any of the following conditions are satisfied [71]:

- track(s) have large d_0 (> 0.2 cm) and/or large z_0 (> 60 cm), as well as the measures of d_0 for both potential cosmic legs are correlated,
- track(s) are acollinear in Rz with an acollinearity angle > 3.1 rad,
- significant out-of-time energy. Calorimeter energy towers should typically be within a $[-10$ ns, $+10$ ns] lower-upper bound timing window with an energy greater than 0.75 GeV to be considered in-time and not cosmic ray related.
- large out-of-time Time of Flight measurement where the time difference, Δ_{TOF} , between the top and bottom leg of a di-muon pair is $|\Delta_{TOF}| > 5$ ns. For a real event $\Delta_{TOF} \approx 0$.

Step 3: Peripheral Collision Cuts

In addition to the cosmic ray veto, we require the following:

- Acoplanarity angle $|\phi| < 0.10$ rad,
- $|p_T(\mu^+) - p_T(\mu^-)| < 0.4$ GeV/c,
- $p_T(\mu^+\mu^-) < 0.25$ GeV/c.

Step 4: Peripheral Collision Cuts + J/ψ Veto

In addition to the cosmic ray veto, we apply the Peripheral Collision Cuts of Step 3 along with a requirement that the reconstructed $\mu^+\mu^-$ invariant mass be separated from the mass of the J/ψ by at least $3\sigma(J/\psi)$.

- Acoplanarity angle $|\phi| < 0.10$ rad,
- $|p_T(\mu^+) - p_T(\mu^-)| < 0.4$ GeV/c,
- $p_T(\mu^+\mu^-) < 0.25$ GeV/c,
- $|M(J/\psi) - M(\mu^+\mu^-)| < 3\sigma(J/\psi)$.

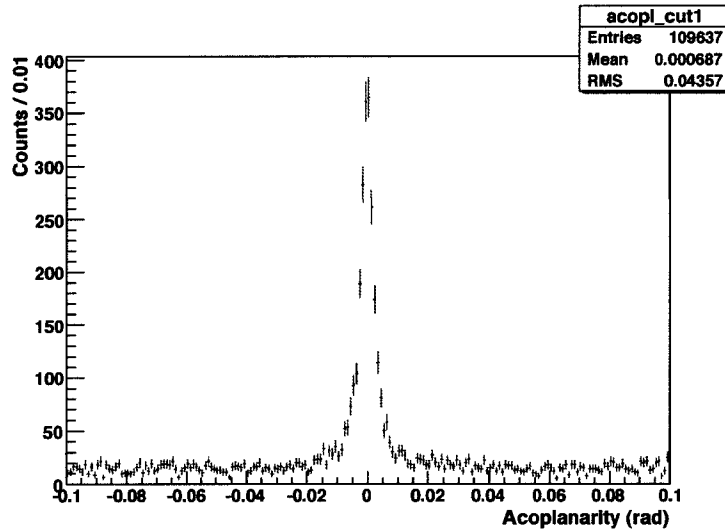


Figure 6.10: (Step 1) Reconstructed acoplanarity angle between the two measured muons.

Comparison with Monte Carlo

The result of each step of analysis as applied to the diffractive physics data sample is given below. The basic event characteristics evident at each stage of the analysis are outlined leading to a preliminary set of candidate $\gamma\gamma \rightarrow \mu^+\mu^-$ events. A detailed comparison with the expectations from simulation is made. However it should be noted that the results presented here are indeed preliminary that, although having been presented to the CDF QCD Working Group, require some further refinement before being considered as approved (or blessed in the CDF nomenclature) for public release into a thesis or publication. Therefore the results presented here include distributions for both simulation and data that have been normalized to unit area thereby enabling a comparison to be made in terms of the shapes of distributions. These results though cannot be used at the present time to infer a measurement for the process cross section. Nonetheless such a measurement is the subject of future work.

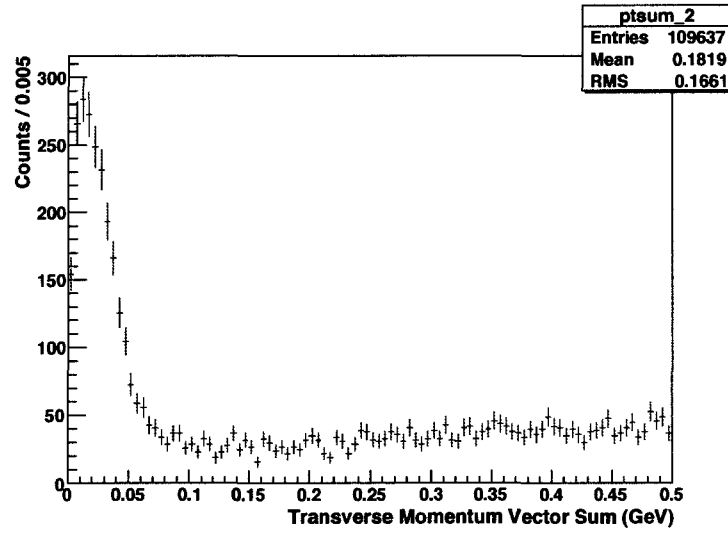


Figure 6.11: (Step 1) Magnitude of the vector sum of the muon pair transverse momenta.

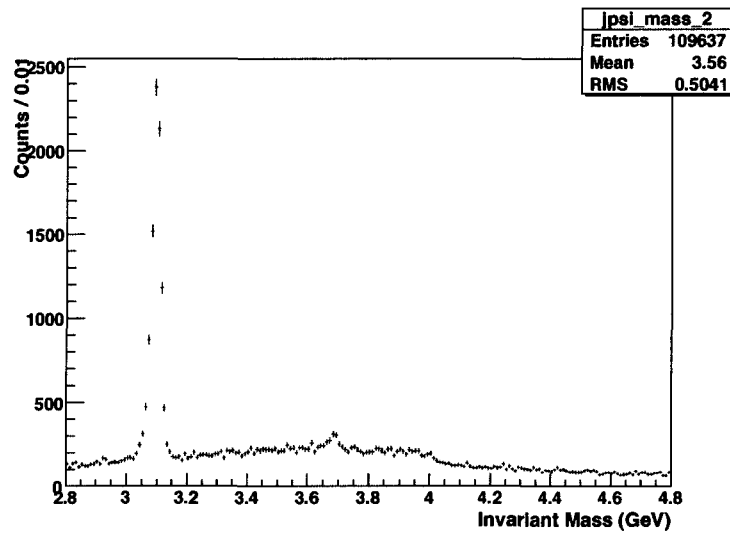


Figure 6.12: (Step 1) Reconstructed invariant mass of the observed muon pairs.

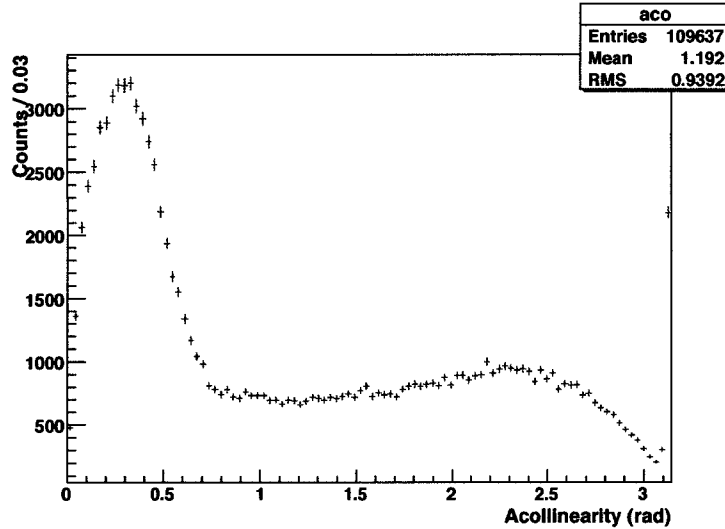


Figure 6.13: (Step 1) Reconstructed acollinearity of the two measured muons. Values of acollinearity near 180 degrees are characteristic of cosmic rays traversing CDF.

Step 1 Results: Muon and Track Quality Requirements

Figure 6.10 plots the distribution of reconstructed acoplanarity angle ϕ for all $\mu^+\mu^-$ pairs satisfying the muon and track requirements of Step 1. Figure 6.11 shows the reconstructed sum transverse momentum of the $\mu^+\mu^-$ pairs which peaks below 0.050 GeV/c. Figure 6.12 displays the reconstructed $\mu^+\mu^-$ pair invariant mass where peaks are observed near 3.1 GeV/c² and 3.7 GeV/c² corresponding to the masses of the J/ψ and $\psi' = \psi(2s)$, respectively.

Step 2 Results: Cosmic Ray Veto

The presence of cosmic ray muons in events accepted by the diffractive trigger become evident when examining the distributions of the $\mu^+\mu^-$ pair p_T (Figure 6.11) and measured opening angle or acollinearity of the tracks (Figure 6.13). The peak in the distribution near zero pair p_T , as well as acollinearity angles very near π radians are characteristic of cosmic rays tracks observed within CDF. The acceptance of such events in the triggered data sample are removed if any of the cosmic ray veto conditions of Step 2 have been met. A separate Cosmic Ray Data block exists in the CDF StNtuple analysis chain

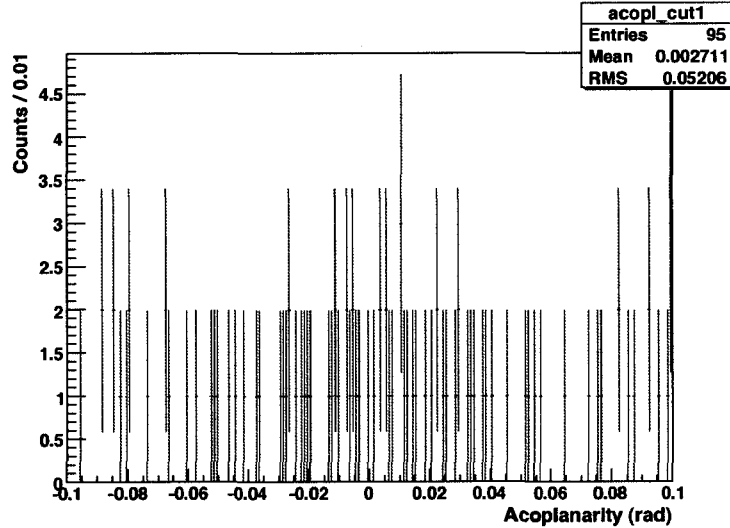


Figure 6.14: (Step 3) Reconstructed invariant mass of the observed muon pairs.

which provides access to this information for all events.

Step 3 Results: Peripheral Collision Cuts

Shown in Figure 6.14 is the reconstructed acoplanarity angle for all $\mu^+\mu^-$ pairs from the examined *gdf0d* dataset which satisfy the muon and track quality requirements, survive the cosmic ray veto, and have passed the peripheral collision criteria for the selection of exclusive $\gamma\gamma \rightarrow \mu^+\mu^-$ events. Similarly shown in Figure 6.15 is the reconstructed sum transverse momentum of the $\mu^+\mu^-$ pairs. Figure 6.16 demonstrates the values of the reconstructed $\mu^+\mu^-$ invariant mass for these events. The presence of the J/ψ and ψ' mass peaks are clearly prominent in the mass distribution. Also all measures of the acollinearity angle as shown in Figure 6.17 are consistent with events that do not contain misidentified cosmic ray muons as all values are below π radians.

J/ψ Background Rejection

Shown in Figure 6.18 is the measured invariant mass distribution for the range of 2.8 to 3.3 GeV/c^2 which overlaps with the expected J/ψ mass peak [15] and is clearly visible near 3.1 GeV/c^2 . The calculation of the observed invariant mass is based upon those good quality muon tracks in the event that have not

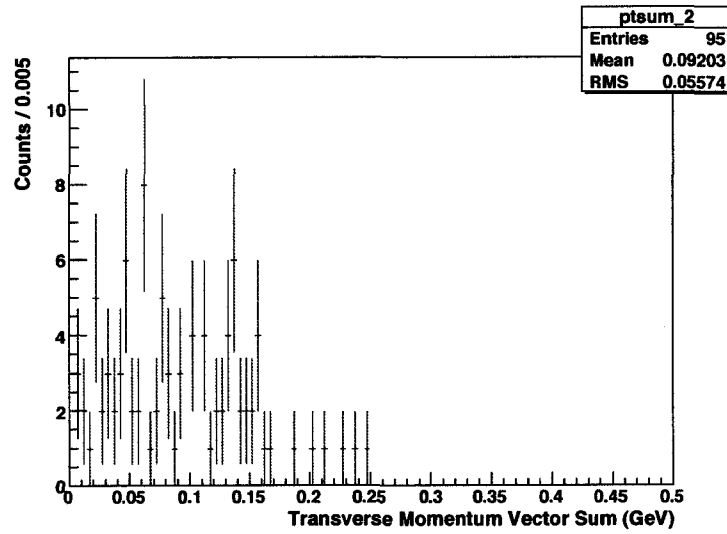


Figure 6.15: (Step 3) Magnitude of the vector sum of the muon pair transverse momenta.

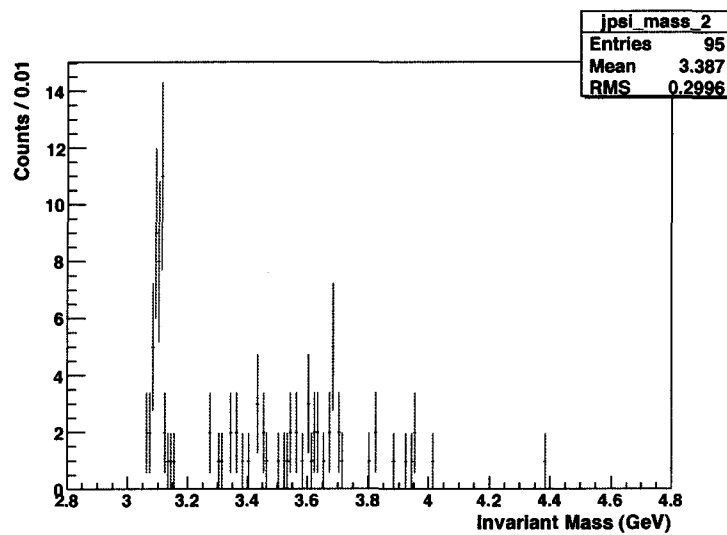


Figure 6.16: (Step 3) Reconstructed invariant mass of the observed muon pairs.

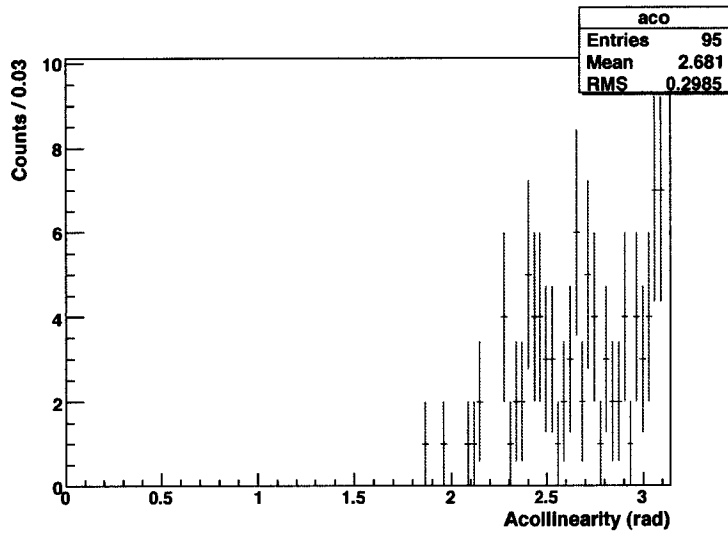


Figure 6.17: (Step 3) Reconstructed acollinearity of the two measured muons. Values of acollinearity near π radians are characteristic of cosmic rays traversing CDF.

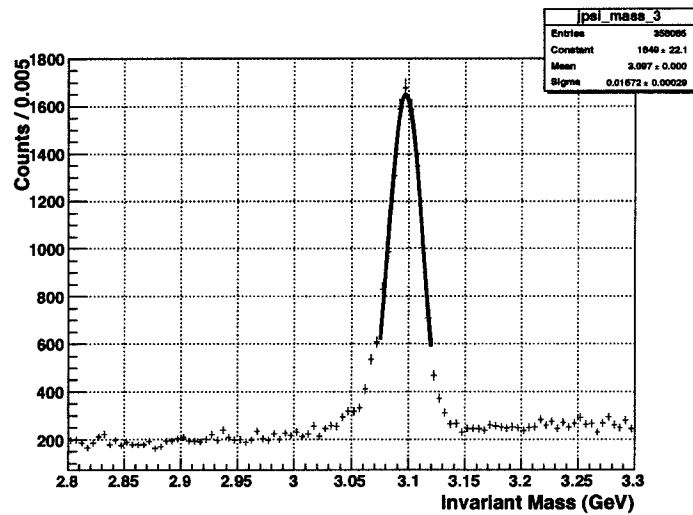


Figure 6.18: Reconstructed invariant mass and width of the di-muon pair around the mass of the J/ψ meson.

triggered the cosmic ray veto. Fitting the peak with a Gaussian yields a mean of $3.097 \text{ GeV}/c^2$ with a σ of $0.016 \text{ GeV}/c^2$. The fitted value for the invariant mass peak from the *gdf0d* dataset is used to provide the reference J/ψ mass as reconstructed in the CDF detector without requiring any extensive energy scale calibration processes. To eliminate the possibility of a J/ψ decay to $\mu^+\mu^-$ being misidentified as originating from an elastic two photon collision all events in which the reconstructed invariant mass is within 3σ of the J/ψ peak are rejected. ²

Step 4 Results: Peripheral Collision Cuts + J/ψ Veto

After the application of the Step 4 selection cuts a total of 54 potential $\gamma\gamma \rightarrow \mu^+\mu^-$ candidates remain from the examined portion of the *gdf0d* dataset which extended into the early part of 2005. Figures 6.19, 6.20 and 6.21 display the distribution of reconstructed acoplanarity angle, transverse momentum and invariant mass of the $\mu^+\mu^-$ pairs from data, respectively. Also shown in the three histograms are the corresponding distributions as predicted by the elastic LPAIR Monte Carlo simulation. Since the results have yet to be officially blessed via the CDF QCD working group, both the data and simulated distributions have been normalized to unit area under the curves, as indicated by the per bin weighting along the vertical axis. This enables us to perform a detailed comparison of the predicted and measured shapes of the distributions, while at the same time remaining conservative and avoid an unnecessarily preliminary estimate of the process cross section at the Tevatron. An excess in one bin of the invariant mass distribution near the mass of the ψ' is clearly visible above the simulation result near $3.7 \text{ GeV}/c^2$ of Figure 6.21.

Event displays for two of the preliminary $\gamma\gamma \rightarrow \mu^+\mu^-$ candidates are shown in Figures 6.22 and 6.23. The near zero acoplanarity angle along with the absence of any other activity in the event are good indicators of the elastic two photon interaction. Nonetheless additional steps need to be taken to ensure the exclusivity of the events, as well as to eliminate the possibility

²Although not included in this analysis a similar selection criteria needs to be applied to restrict the considered mass window to be outside the expected range for ψ' production.

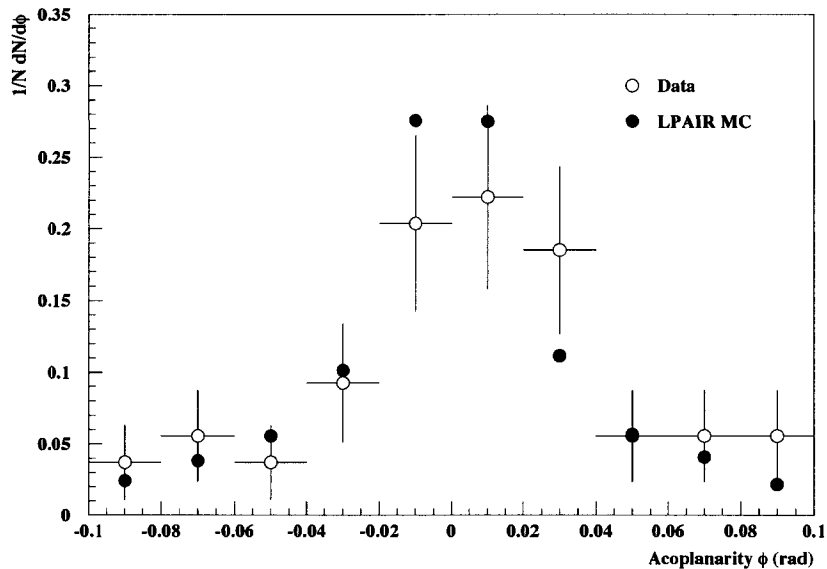


Figure 6.19: (Step 4) Reconstructed acoplanarity angle between the two measured muons for data and simulation.

of contamination from either the J/ψ or ψ' . This includes a more detailed examination of all calorimetric activity in the candidate events in order to determine any levels of activity which, although insufficient to result in the reconstruction and identification of a high-level object such as an electron or jet, may have gone undetected in the current level of exclusivity analysis. Furthermore it is planned to extend the study to non-exclusive events at CDF where the combination of kinematic and vertex fit requirements can be applied as discussed in the ATLAS context of Chapter 5.

6.3 Electron pair production

In addition to the above described search for the exclusive production of $\gamma\gamma \rightarrow \mu^+\mu^-$ a corresponding search for exclusive e^+e^- production via the same two photon process has been ongoing by members of the CDF diffractive physics group and the author [72]. For that analysis the exclusivity requirements have been more extensively studied and the methods developed there

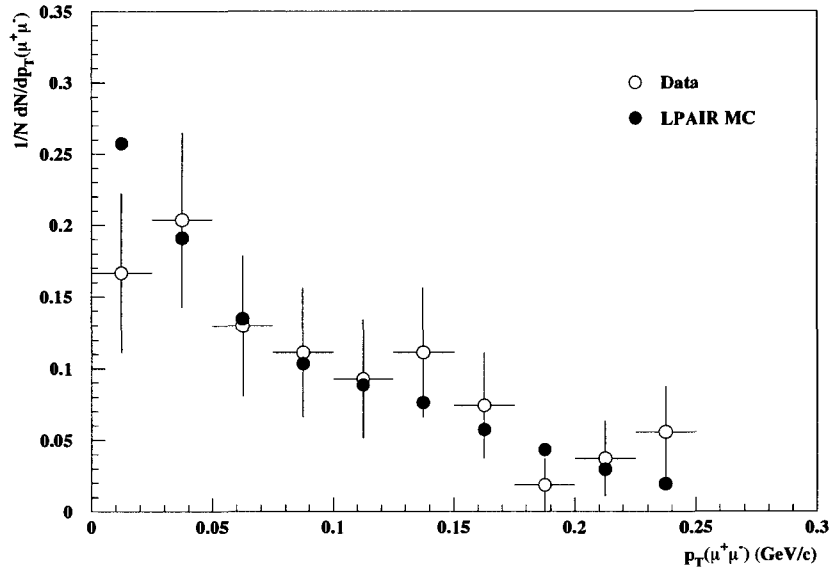


Figure 6.20: (Step 4) Magnitude of the vector sum of the muon pair transverse momenta for data and simulation.

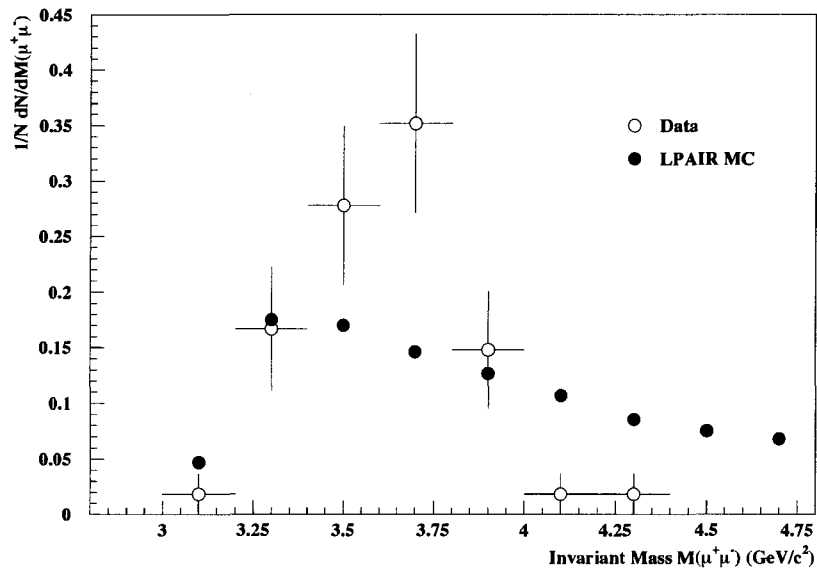


Figure 6.21: (Step 4) Reconstructed invariant mass of the observed muon pairs for data and simulation.

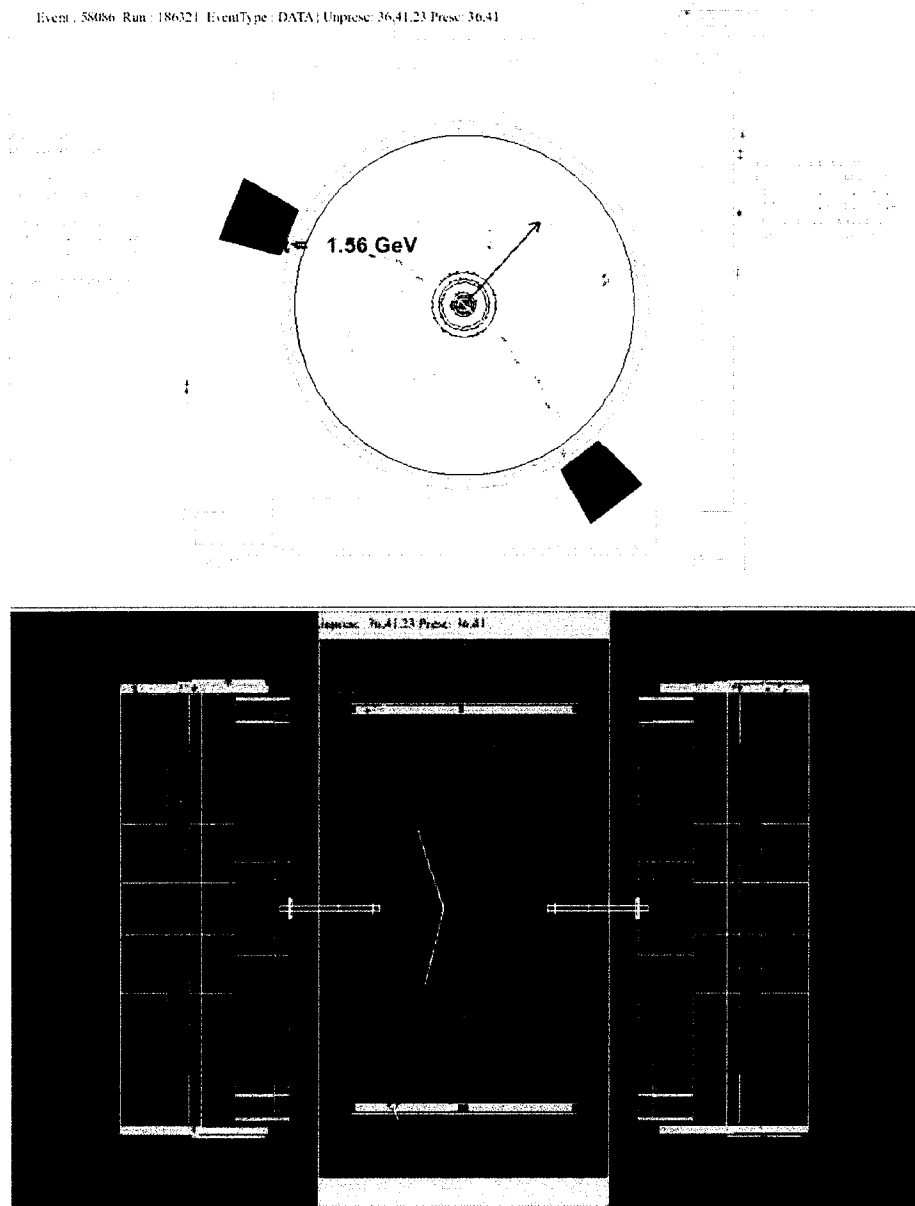


Figure 6.22: $R\phi$ view transverse to the beam-line (top) and $R-Z$ view (bottom) of a candidate two photon to muon pair event observed at CDF.

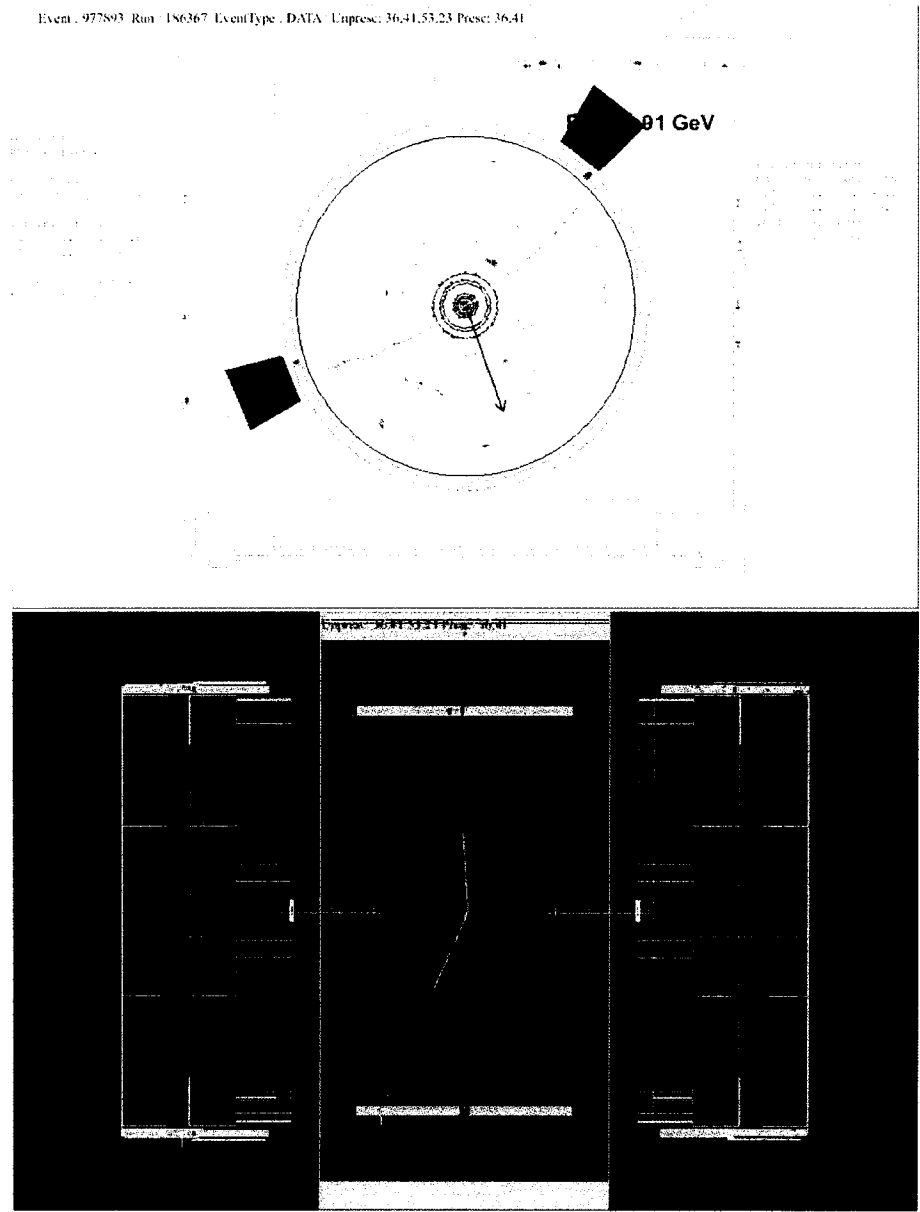


Figure 6.23: $R\phi$ view transverse to the beam-line (top) and R-Z view (bottom) of a candidate two photon to muon pair event observed at CDF.

will be carried over to the examination of the exclusivity associated with the $\mu^+\mu^-$ selection. Essential to the definition of exclusivity for the $\mu^+\mu^-$ and e^+e^- analyses, and the diffractive trigger sample, are the Beam Shower Counters (BSC). For the $\gamma\gamma \rightarrow e^+e^-$ search the results achieved so far have received pre-blessing from the CDF QCD working group and have been presented publicly [73]. Shown in Figure 6.24 are the reconstructed transverse momentum of the e^+e^- pair, along with the measure of $\Delta\phi$ (equivalent in this case to the acoplanarity angle). For comparison the normalized distributions predicted from the LPAIR Monte Carlo generator as fully simulated within CDF are also shown.

For the e^+e^- search the trigger requirements included a veto on any hits in either the East or West BSC, as well as two EM shower objects each with $E_T > 4$ GeV. Subsequent offline selection criteria include the application of EM object and tracking cuts so as to identify the e^+ and e^- , along with a series of cuts to ensure the exclusive nature of the event. The total sample thus far analysed represents an integrated luminosity of 325 ± 25 pb⁻¹ and from this sample a total of 10 e^+e^- candidates were found. By comparison from Monte Carlo studies with the LPAIR generator the expected number of events to be 9 ± 3 events. The uncertainty of 3 events predominantly accounts for the efficiencies of the electron trigger, as well as the electron reconstruction and identification efficiencies. As of yet though the background subtraction of inelastic type events has yet to be done, and as such a cross section estimate cannot be stated publicly at this time.

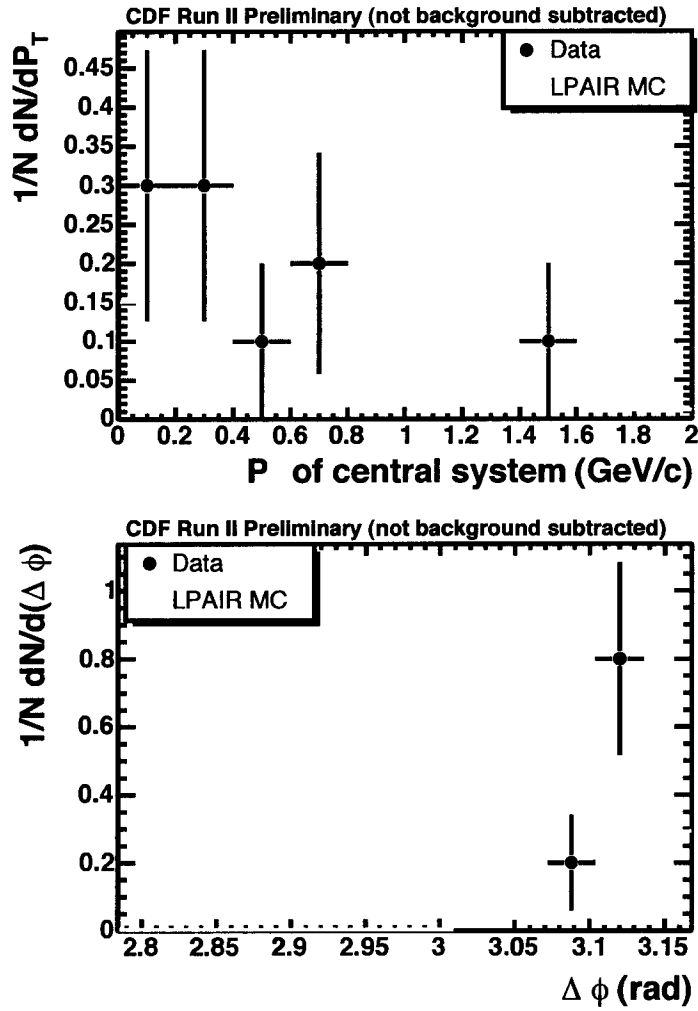


Figure 6.24: Distributions of the observed acoplanarity angle (top) and p_T (bottom) of the electron-positron pair from CDF data (dots) and simulation with LPAIR (histogram).

Chapter 7

Luminosity Measurement and Monitoring via Single Gauge Boson Production

In this chapter the concept of applying the observation of single W and Z bosons as a device for luminosity measurement and monitoring is reviewed. In addition to the standard experimental uncertainties associated with identifying the lepton decay of the W and Z bosons, the level of uncertainty introduced into the luminosity determination is naturally dependent upon the theoretical uncertainties associated with the higher-order QCD corrections. Additionally the choice of input Parton Distribution Function (PDF) can strongly influence the observed W and Z boson decay properties.

In this chapter we will review the trigger and event selection criteria for W and Z events in ATLAS along with the operational characteristics of deploying such a monitor. The effects of the most recently available higher-order QCD corrections upon the expected W and Z properties will be examined. Finally the relatively new method of PDF reweighting will be studied and applied to the selection of Z events. In turn the utility of this procedure will be demonstrated via a comparison with the more standard brute force method of generating otherwise identical simulation samples but with different PDF error input sets.

Boson	Trigger	Low Luminosity $2 \times 10^{33} \text{cm}^{-2} \text{s}^{-1}$	High Luminosity $1 \times 10^{34} \text{cm}^{-2} \text{s}^{-1}$
W^\pm	Level-1	MU20/EM25I	MU20/EM30I
	Level-2	$\mu 20\text{i}/e 25\text{i}$	$\mu 20/e 30\text{i}$
Z^0	Level-1	MU6/EM15I $\times 2$	MU6/EM20I $\times 2$
	Level-2	$\mu 10/e 15\text{i} \times 2$	$\mu 10/e 20\text{i} \times 2$

Table 7.1: ATLAS Level 1 and 2 trigger definitions implemented for the selection of W^\pm and Z^0 events at the LHC. The symbols MU and EM represent muon and electromagnetic objects, respectively, with the following number indicative of the p_T threshold for the Level 1 trigger. At Level-2 EM objects can be further refined into electron (e) objects. The symbols I(i) indicate a requirement of isolation around the object.

7.1 W and Z Production

The expected number of W and Z events via the Drell-Yan process at the LHC can be schematically represented as shown in Eqn 7.1

$$\begin{aligned}
 N_{pp \rightarrow W^\pm} &= L \times \text{PDF}(x_1, x_2, Q^2) \times \sigma_{q\bar{q} \rightarrow W^\pm} \\
 N_{pp \rightarrow Z^0} &= L \times \text{PDF}(x_1, x_2, Q^2) \times \sigma_{q\bar{q} \rightarrow Z^0}
 \end{aligned}
 \tag{7.1}$$

where L is the integrated luminosity accepted by the detector, $\text{PDF}(x_1, x_2, Q^2)$ is the fraction of incoming proton momentum carried by each of the partons colliding to produce the W or Z at the Q^2 of the collision, and $\sigma \rightarrow W^\pm/Z^0$ is the parton-level cross section for the boson production.

7.1.1 Trigger Criteria and Event Selection

In addition to the Level 1 and 2 trigger thresholds listed in Table 7.1, further offline selection criteria are applied so as to efficiently select events while at the same time rejecting background processes. The offline selection criteria for single W^\pm production, as optimized for the studies prepared for the ATLAS Physics TDR, include:

- An isolated e or μ with $p_T > 25 \text{ GeV}/c$ within $|\eta| < 2.4$,
- Measured missing transverse energy measurement of $E_T^{\text{miss}} > 25 \text{ GeV}$,

- No reconstructed jets in the event with $p_T(\text{jet}) > 30 \text{ GeV}/c$,
- Measured recoil of the event against the W of $|p_T| < 20 \text{ GeV}/c$.

With lepton reconstruction and identification efficiencies of approximately 90% and 80%, respectively, the overall selection efficiency for the production of $W \rightarrow l\nu$ where $l = e, \mu$ is approximately 25%. This is the value for the efficiency as determined from full simulation of the ATLAS detector. An equivalent efficiency was determined through the application of the above cuts to a sample of W events generated with Pythia and subsequently passed through the ATLFAST program [74, 75].

In addition the contributions from background processes which pass the event selection criteria need to be taken into consideration. Accordingly the true number of W produced is given by

$$N = \frac{N_{cand}(1 - f_{QCD}) - N_Z}{\epsilon A(1 + \frac{A_\tau}{A})\sigma_W} \quad (7.2)$$

Here N_{cand} is the number of W candidates, f_{QCD} is the fraction of QCD candidates which pass the W selection criteria, N_Z is the number of candidates that are actually Z where one of the leptons is outside the detector acceptance and goes undetected, ϵ is the lepton identification efficiency for the detector, A is the detector acceptance for the observation of the $l = e, \mu$ decays of the W , A_τ is the acceptance times branching ratio for misidentified $W \rightarrow \tau\nu$ decays, and σ_W is the theoretical cross section.

The dominant source of background for the electron and muon channels is from the production of $W \rightarrow \tau\nu$ and the production of $Z \rightarrow \mu^+\mu^-$ in the muon channel. The expected levels of these backgrounds at the LHC and ATLAS are 1.3% and 4%, respectively [16]. The background from QCD multi-jet events is considered to be negligible for ATLAS given the good electron-jet separation of the detector with jet rejection factors of the order of 10^5 . With these selection criteria approximately 12×10^7 $W \rightarrow l\nu$ events are expected per year at low luminosity ($2 \times 10^{33} \text{ cm}^{-2} \text{ s}^{-1}$) assuming an integrated luminosity of 20 fb^{-1} .

Boson	Low Luminosity $2 \times 10^{33} \text{cm}^{-2} \text{s}^{-1}$		
	Rate (Hz)	$t(\text{seconds})(\delta L/L < 1\%)$	$t(\text{seconds})(\delta L/L < 5\%)$
W^\pm	12	900	30
Z^0	2	5400	180
Boson	High Luminosity $1 \times 10^{34} \text{cm}^{-2} \text{s}^{-1}$		
	Rate (Hz)	$t(\text{seconds})(\delta L/L < 1\%)$	$t(\text{seconds})(\delta L/L < 5\%)$
W^\pm	60	180	10
Z^0	10	1080	60

Table 7.2: Predicted rates for the observation of W^\pm and Z^0 events at the LHC which survive the selection cuts.

7.1.2 Operational Considerations

Following the application of event selection criteria as described above the estimated W and Z production rates at the final stage of the ATLAS trigger known as the Event Filter (assuming that the offline algorithms are used) are given in Table 7.2. Also included are the estimated running times necessary to provide a statistical error of less than 1% (5%) for the measured luminosity via the W/Z production process.

However during all periods of LHC machine operation in which the proton beams are colliding the actual luminosity delivered to the experiments will decrease with time, following an exponential decay associated with the luminosity lifetime τ_{lumi} . In general the luminosity lifetime is foreseen to last between 8.6 and 28 hours and will vary depending upon the stage of commissioning and progression toward the ultimate design luminosity. The normalized exponential decays of τ_{lumi} during the first year of operation and accelerator commissioning, as well as for the nominal and peak luminosities is shown in Figure 7.1 [76]. Typically collisions will be halted and the beams dumped when the luminosity has decreased to approximately 20% of the peak initial luminosity at the beginning of the run. As a result of the luminosity lifetime the W and Z event rates listed in Table 7.2 are the maximum expected values and represent the observed rates during a run when the beams are first brought into collision.

Taking the luminosity lifetime into consideration, at low luminosity the

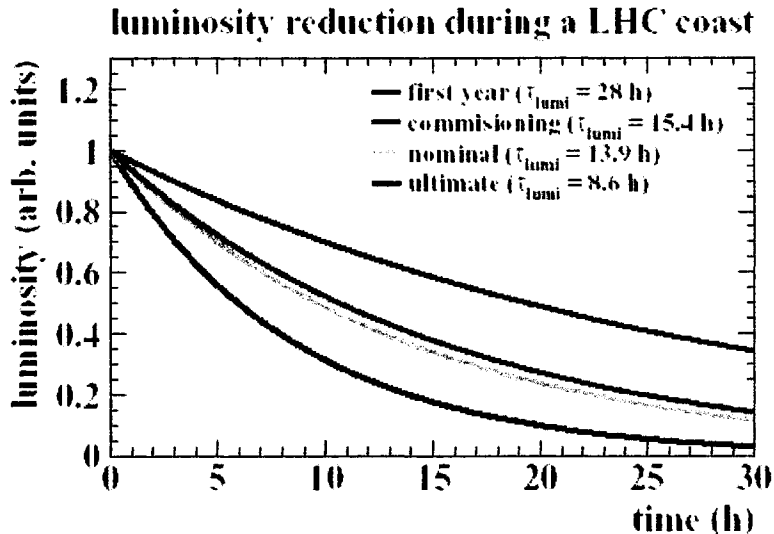


Figure 7.1: Exponential decay of the colliding beam luminosity at the LHC as a function of the expected beam lifetime τ_{lumi} .

rate of W production is expected to vary between 12 and 2.4 Hz, increasing to between 60 and 12 Hz at high luminosity. Similarly the rate of Z production is expected to vary between 2.0 and 0.4 Hz at low luminosity, and between 10.0 and 2.0 Hz at high luminosity.

7.1.3 PDF Errors and W/Z Production beyond Leading Order

In addition to the tree-level amplitude for the Drell-Yan production of W and Z bosons previously shown in Figure 4.5, for accurate comparisons with current data from the Tevatron experiments, as well as the upcoming data from the LHC, it is necessary to consider calculations and simulations that can be carried beyond Leading Order (LO). The Feynman diagrams which correspond to the parton model Drell-Yan cross section corrections at Next-to-Leading Order (NLO) $O(\alpha_s)$ and Next-to-Next Leading Order (NNLO) $O(\alpha_s^2)$ in perturbative QCD are shown in Figures 7.2 and 7.3, respectively [54, 77].

One available tool that can perform such NLO and NNLO calculations is Vrap [78]. Vrap is the computer program written in C++ by Lance Dixon and collaborators based upon their published calculations for W and Z production

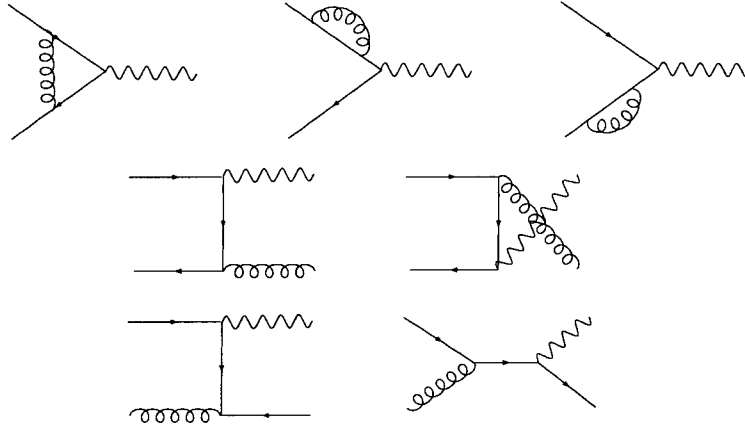


Figure 7.2: Feynman diagrams for the NLO QCD corrections to the production of W and Z bosons.

at NLO and NNLO [54]. The code enables one to calculate the rapidity distribution for the production of lepton pairs at hadron colliders via γ^* , Z and W bosons at LO, NLO and NNLO in perturbative QCD. While the code enables the calculation of the cross section it is not a Monte Carlo generator. The Vrap code calculates the value of $\frac{d^2\sigma}{dM dY}$ where M is the mass of the produced lepton pair and Y is the lepton pair rapidity, taking into account both the NLO and NNLO QCD corrections.

Within the program it is possible to vary input parameters such as the factorization ¹ and renormalization ² scales μ_F and μ_R , respectively. The current standard relationship between μ_F and μ_R assumes that they are taken to be equal and allowed to vary over a range defined by the mass M of the produced lepton pair.

$$M/2 < \mu_R = \mu_F < 2M \quad (7.3)$$

Therefore for the production of W and Z the value of M is the mass of the intermediate vector boson under consideration. Figure 7.4 plots the values

¹The scale at which it is chosen to separate the short- from the long-distance dynamic effects and to be carried out order by order in perturbation theory. Short distance dynamics are represented by the hard-scattering amplitude, while long-distance dynamics are accounted for in the distribution amplitude [79].

²Perturbative QCD calculations to a finite order requires that Ultra-Violet divergences be renormalized, thereby introducing a renormalization scale dependence to the calculation [79].

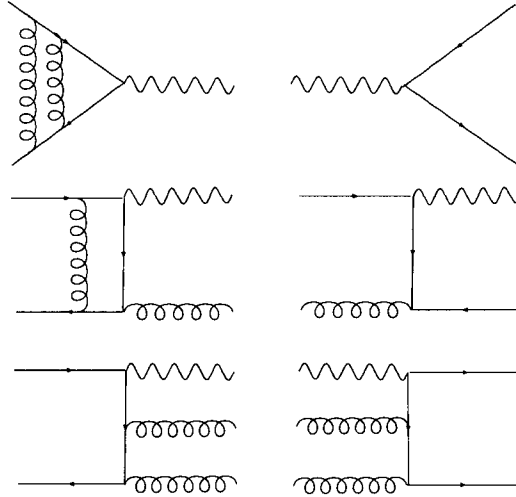


Figure 7.3: Feynman diagrams for the NNLO QCD corrections to the production of W and Z bosons.

of the differential cross section for Z production at the LHC as a function of the boson rapidity Y at LO, NLO and NNLO. Furthermore the values of the renormalization and factorization scales were allowed to vary according to equation 7.3. It is clearly visible that the resulting uncertainty in the predicted cross section is between 25 and 30% at tree-level. However when progressing to NLO and NNLO the cross section uncertainty decreases significantly, to less than 6% and 1% at NLO and NNLO, respectively. The distributions and uncertainties of Figure 7.4 as calculated with Vrap are in agreement with the published results given in [54].

Within Vrap several PDF sets are available including CTEQ5 (at LO and NLO), MRST 2001 (at LO, NLO and NNLO) and Alekhin02 (at NNLO). However, the Vrap code does not include any built-in interfaces to the more recently released CTEQ6.1 and MRST 2001 PDF error sets, both of which are computed at NLO accuracy. Therefore in order to study the effects of the calculated PDF uncertainties the Vrap code was modified as part of this study so as to enable access to these important PDF sets, in addition to the PDF sets already available. While it is possible to compute the production cross sections to NNLO accuracy with Vrap, it is not possible to access PDF sets to the same level of accuracy while simultaneously having access to the error eigenvector

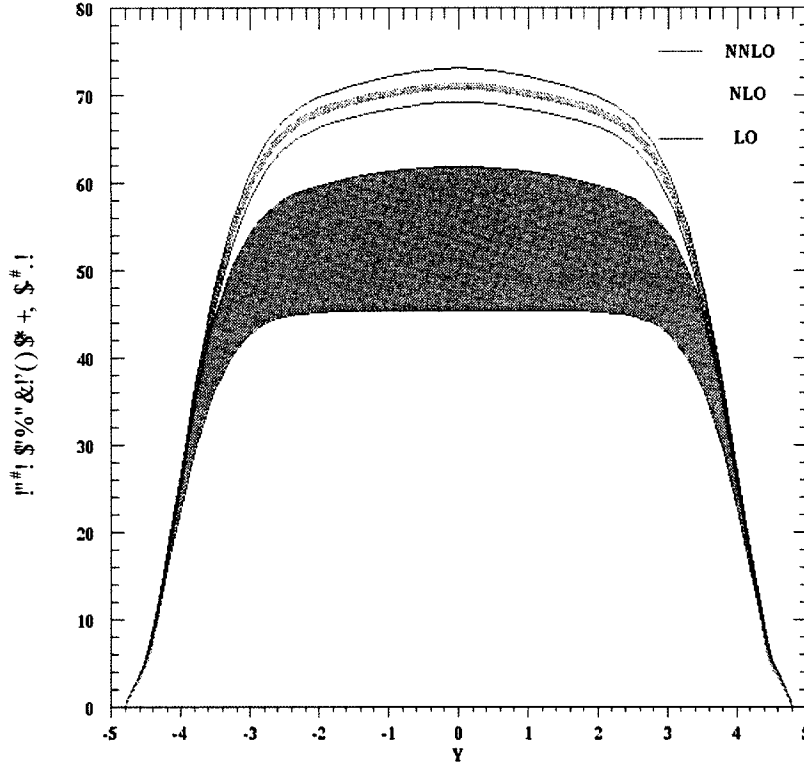


Figure 7.4: Predicted cross sections for the production of Z^0 bosons at LO, NLO and NNLO for the LHC. The error bands represent the uncertainties associated with variations in μ_F and μ_R between $M_Z/2$ and $2M_Z$, and significantly reduce at higher orders.

sets. The MRST 2001 and Alekhin02 PDF sets are available at NNLO, but are only the best fit PDFs and do not include any error sets that represent the PDF uncertainties. Furthermore all current NNLO calculations for W and Z production do not take the lepton spin correlations into account [80]. Since the lepton spin correlations are correctly handled at NLO it was decided to restrict our study to the use of Vrap with a NLO PDF error set. Due to the inherently more conservative estimate of the PDF errors for CTEQ6.1 as compared to MRST 2001, which result from their differing tolerances T being employed during the global fits to the available data (see Section 4.2.1), for this study only the 40 error PDF sets of CTEQ6.1 were applied to the W and Z cross sections at NLO. This should then represent a reasonable estimate of the upper limit effect due to the PDF errors. A comparison with the MRST

2001 PDF error set is left for future studies.

Since the Vrap code is a cross section calculator and not a Monte Carlo generator, to determine the effect of the PDF error uncertainties it was necessary to run a separate task that individually linked each member of the PDF error set.³

Following the prescription given in Equation 4.33 the positive and negative errors over all eigenvector PDF error set pairs is calculated for each rapidity bin Y . The best-fit PDF result for the production of W^+ , W^- and Z^0 is shown as the solid middle line in Figures 7.5, 7.8 and 7.11, respectively. In each case the magnitude of the associated uncertainties due to the PDF error sets are highlighted in green and delimited by the upper and lower distributions. For this calculation the relation $\mu_R = \mu_F = 1/2M_{W/Z}$ is assumed.

To visualize the level of uncertainty resulting from the application of the CTEQ6.1 error PDFs the values of the positive and negative fractional differences from the best-fit PDF set are shown in Figure 7.6. The overall uncertainty from the CTEQ6.1 error PDFs is minimally $\approx 5\%$ for rapidity values of $|Y| \approx 3.5$. However the detection of the W decay products is very difficult at such large Y values. At more central rapidities the resulting uncertainty in the cross section with the PDF error sets increases slightly to approximately 7.5%.

Although Figure 7.6 shows the aggregate effect of the error PDF sets, the individual contributions from the up and down PDF error sets of CTEQ6.1 are shown in Figure 7.7. From this plot the largest contribution to the overall uncertainty in the central rapidity region of $|Y| < 2$ was identified to come from eigenvector 15. Eigenvector 15 of the CTEQ 6.1 error PDF is sensitive to the high x gluon component of the proton momentum. This large contribution to the uncertainty is due to the poorly determined eigenvector direction of the high x gluons [81]. In comparison the highly determined eigenvector directions are predominantly associated with the valence quarks inside the proton.

Histograms of the fractional difference from the best-fit PDF for the pro-

³This is in contrast with the PDF reweighting technique that can be applied to Monte Carlo simulations and is described in Section 7.1.4.

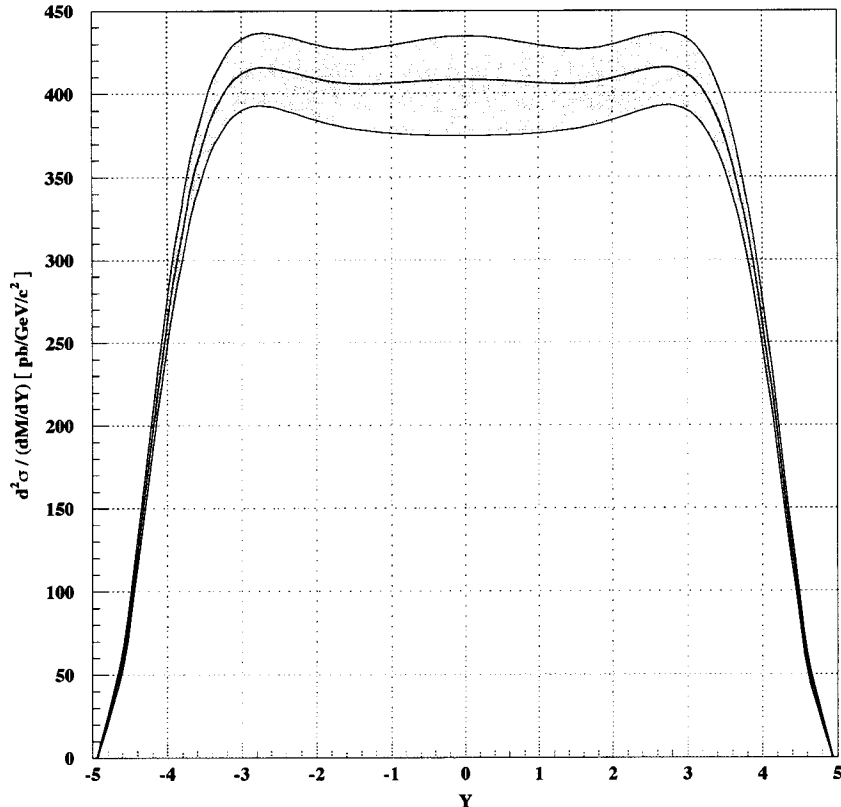


Figure 7.5: W^+ production cross section at the LHC at NLO using the CTEQ6.1 PDF set including the PDF uncertainties (green).

duction of W^- and Z^0 at the LHC are given in Figures 7.9 and 7.12, respectively. Similarly the contributions to the cross section uncertainty from the individual PDF error sets for W^- and Z^0 production are shown in Figures 7.10 and 7.13. Once again the largest contributions to the cross section uncertainties are associated with the high x gluons of eigenvector 15.

7.1.4 The PDF Reweighting Technique

The introduction of PDF error sets, such as CTEQ6.1 and MRST 2001, greatly aided in studies which calculated the effect of PDF uncertainties on the W and Z production. This necessarily introduced a major increase in the computing resources required to simulate the events for each of the PDF error sets (40 for CTEQ6.1 and 20 for MRST 2001). Therefore approaches in the use of PDF reweighting have been investigated very recently as a method

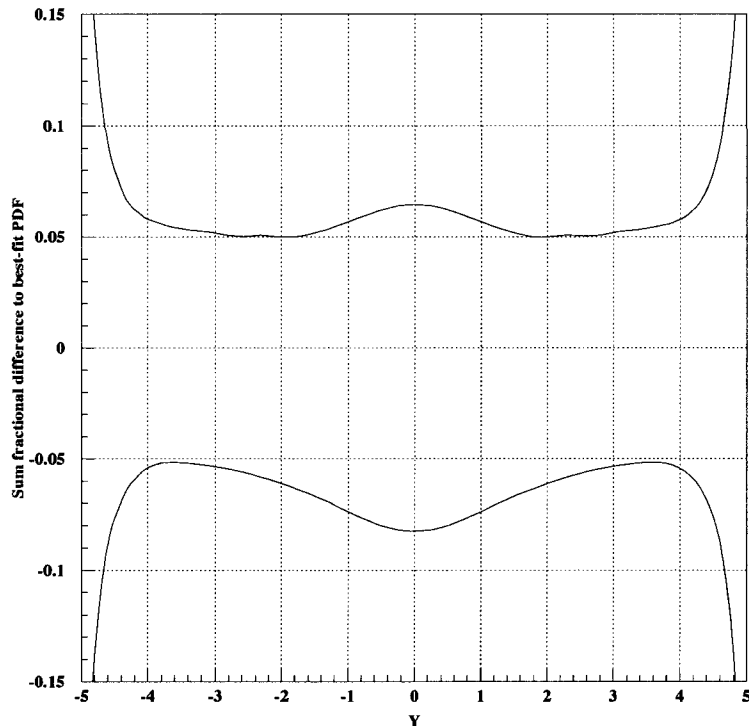


Figure 7.6: Fractional difference of the best-fit CTEQ6.1 PDF set from the sum eigenvector set uncertainties as a function of W^+ boson rapidity.

by which it would be possible to calculate the effects of the PDF error sets while only requiring to run the simulation one time, specifically for the best-fit PDF [82]. The PDF reweighting technique implemented for this study is described below.

With CTEQ and their error PDF sets there are $2N_P + 1$ PDF members which consist of the best fit PDF set S_0 and the eigenvector basis sets in the positive (up) and negative (down) directions along each eigenvector. Therefore for an observable X (such as boson rapidity distribution Y or lepton pseudorapidity η , we can calculate the best estimate from PDF set S_0 and the uncertainty via equation 4.33. One limitation of this formulation is the assumption that the errors are symmetric about the best-fit PDF. A correction to this approach is therefore needed to accommodate the situation where asymmetric errors are present. Table 7.3 presents the standard method by

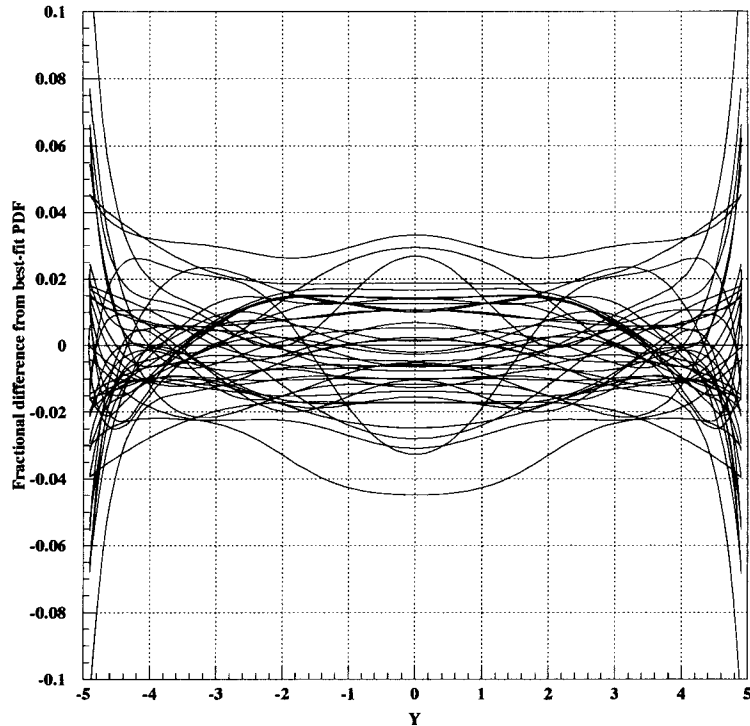


Figure 7.7: Fractional difference of the best-fit CTEQ6.1 PDF set from each eigenvector set uncertainty as a function of W^+ boson rapidity.

which asymmetric errors are calculated.

Furthermore, it is only the uncertainty in the event acceptance arising from the variations introduced by each of the PDF error sets that can be treated as important in addition to the statistical error. This method of error calculation and corresponding evaluation of the acceptance uncertainty due to the PDFs is similar to the procedure followed in a recent CDF measurement of the inclusive W and Z cross sections from Run II at the Fermilab Tevatron [46]. However it should be noted that the study presented in [46] determined the uncertainty on acceptance by the brute force approach of producing simulation samples for the CTEQ6 best-fit PDF and each of the 40 error PDF sets and did not apply the reweighting procedure to only the best-fit PDF member as we describe below.

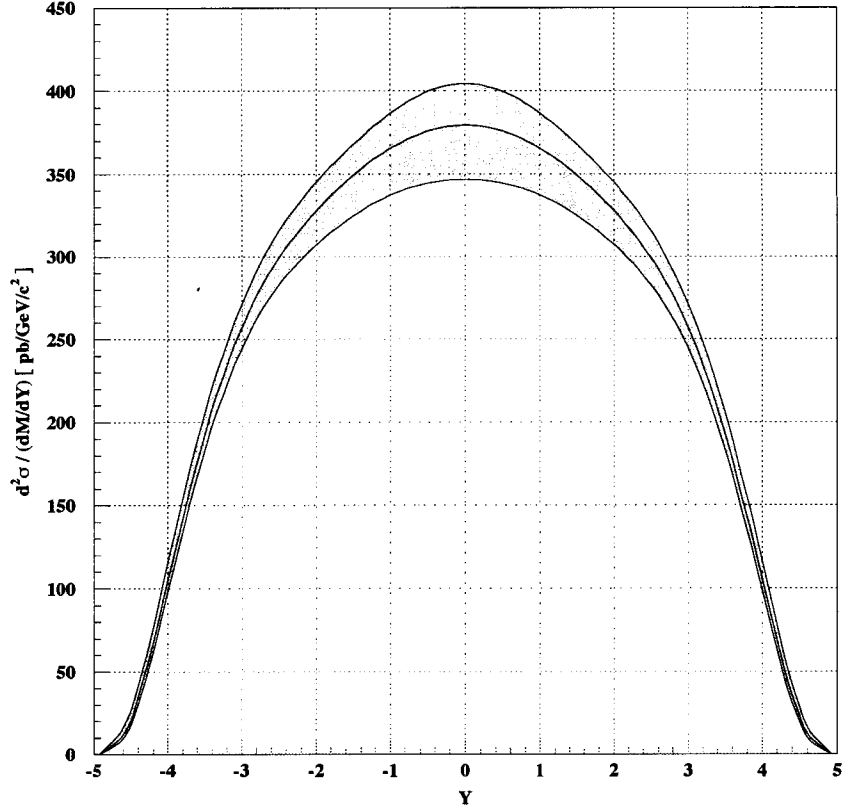


Figure 7.8: W^- production cross section at the LHC at NLO using the CTEQ6.1 PDF set including the PDF uncertainties (green).

Rewighting Procedure

The implementation of the reweighting procedure performed for this study was as follows. Data samples of W and Z from Drell-Yan were produced for the Rome ATLAS Physics Workshop held in June 2005. From the Monte Carlo truth information (the particle level information before any simulation of detector effects) of each event the values of the colliding parton momentum fractions x_1 and x_2 are extracted, along with the flavours of the partons. For the production of intermediate gauge bosons via the Drell-Yan process the value of Q^2 and rapidity Y of the boson can be easily calculated at Leading Order via the relations [37]

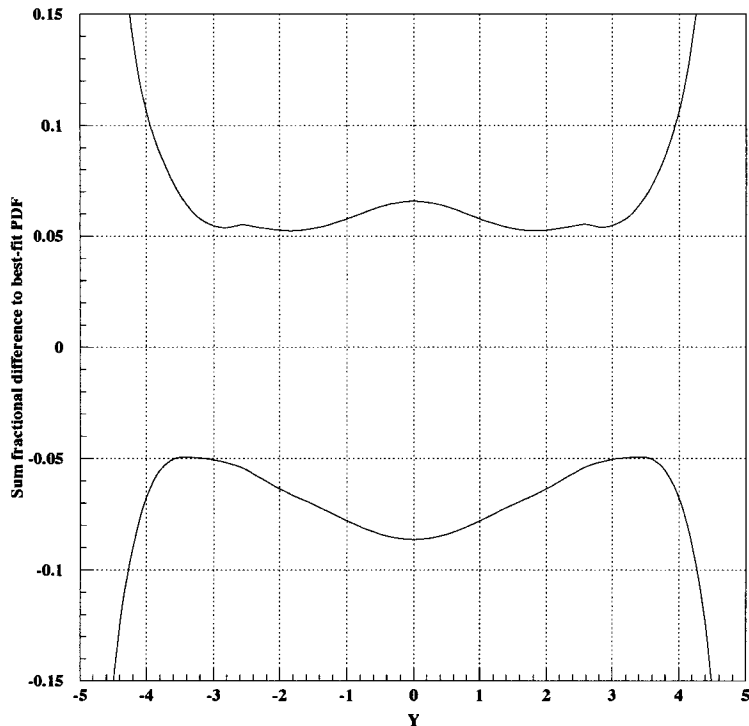


Figure 7.9: Fractional difference of the best-fit CTEQ6.1 PDF set from the sum eigenvector set uncertainties as a function of W^- boson rapidity.

$$Q^2 = \hat{s} = (p_1 + p_2)^2 = x_1 x_2 s = x_1 x_2 4E_{beam}^2 \quad (7.4)$$

$$Q = 2E_{beam} \sqrt{x_1 x_2} \quad (7.5)$$

$$Y = \frac{1}{2} \ln\left(\frac{x_1}{x_2}\right) \quad (7.6)$$

Utilizing the LHAPDF (Version 4.0) software [83] which provides an interface to access most current and prior PDF sets, the values of (x_1, x_2, f_1, f_2) for the event and all PDF error set members is collected, stored, and subsequently evolved to the Q^2 of the reaction. At this point the contribution to the overall reweighting factor w resulting from all members of the PDF error set is calculated according to the equation

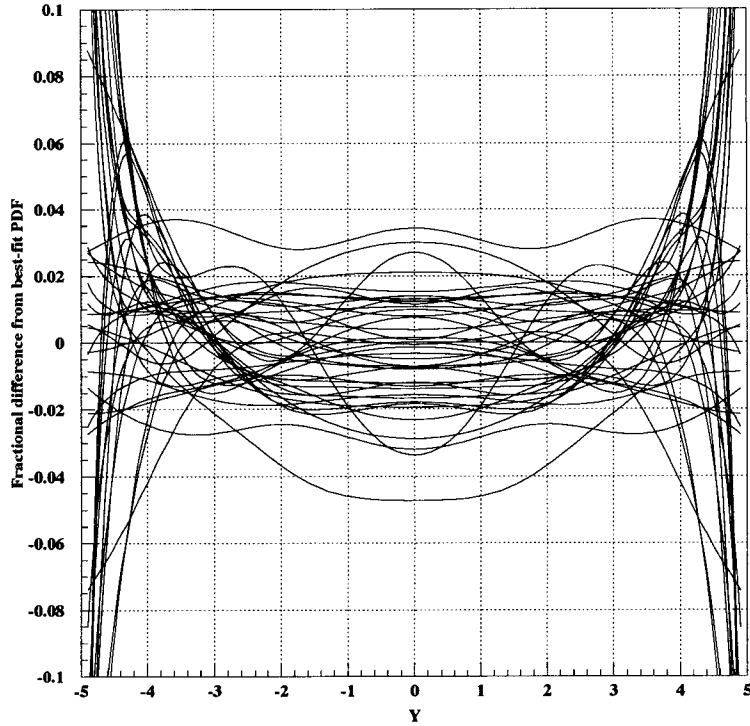


Figure 7.10: Fractional difference of the best-fit CTEQ6.1 PDF set from each eigenvector set uncertainty as a function of W^- boson rapidity.

$$w = \sum_{i=1}^k \frac{f_a^i(x_a, Q) \cdot f_b^i(x_b, Q)}{f_a^0(x_a, Q) \cdot f_b^0(x_b, Q)} \quad (7.7)$$

where the reweighting contribution for each PDF error set member is the product of the momentum PDFs for parton flavours a and b with respective momentum fractions x_a and x_b relative to the equivalent quantity for the PDF best-fit set at the Q^2 of the process. Looping over all 41 PDF sets of the CTEQ6.1 PDF library (1 best fit and 40 error PDF sets corresponding to the 20 eigenvectors) therefore provides a measure of the reweight contributions coming from each PDF set member. A profile histogram is used to record the distribution of PDF reweighting terms as a function of the PDF error set. From this histogram the overall reweight term and its corresponding uncertainty can be calculated as the sum over all PDF error set members

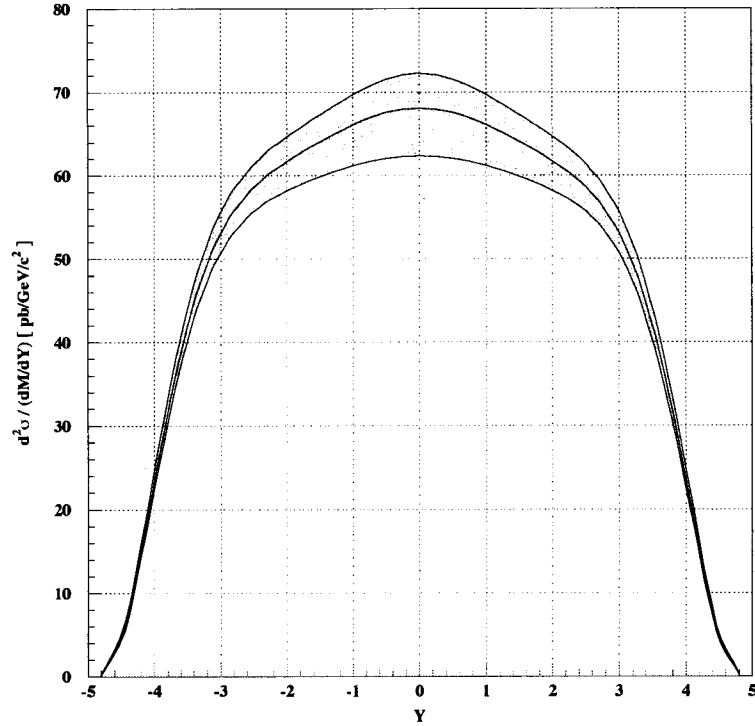


Figure 7.11: Z^0 production cross section at the LHC at NLO using the CTEQ6.1 PDF set including the PDF uncertainties (green).

according to the method outlined in Table 7.3.

Since the W^\pm and Z^0 are only visible via the lepton(s) from their decay, it is most appropriate to keep track of the reweighting terms not only as a function of PDF error set, but also as functions of both the boson rapidity Y and the pseudorapidity η of the lepton(s) coming from the Z^0 and W^\pm . This is accomplished through a second series of profile histograms, one for each rapidity and pseudorapidity bin, that similarly record the distribution of PDF reweighting terms as a function of the PDF error set member. Within each bin the mean and width of the relevant PDF weight distributions are computed separately for each PDF error set.

We therefore have the value of the PDF reweight term for each bin of a physical quantity X . So when considering the distribution of lepton pseudorapidities from W^\pm decays stored into a histogram N_{bins} bins covering the range

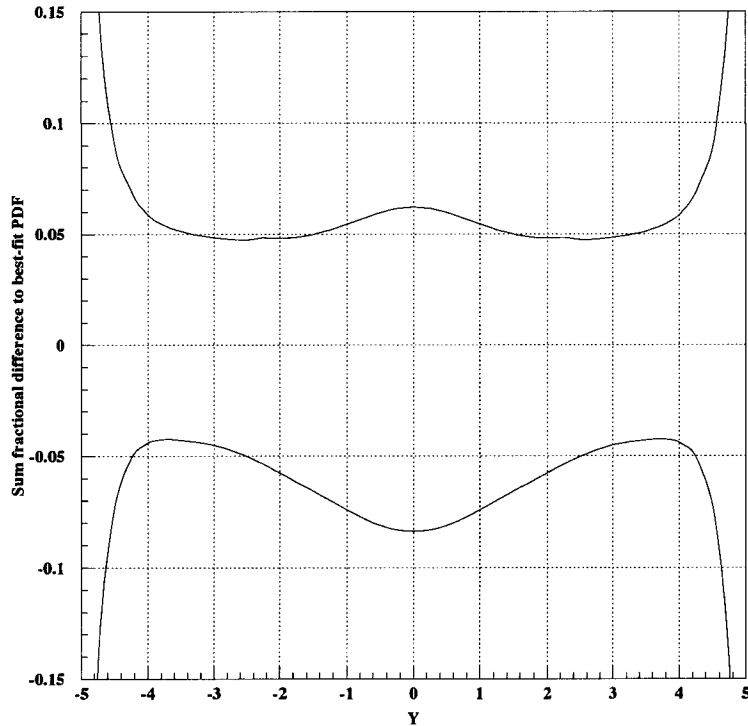


Figure 7.12: Fractional difference of the best-fit CTEQ6.1 PDF set from the sum eigenvector set uncertainties as a function of Z^0 boson rapidity.

of $\eta_{min} \leq |\eta| \leq \eta_{max}$, there will be N_{bins} profile histograms which record the distribution of PDF reweights as a function the PDF error set number. So at the end of the calculation we will have computed the total uncertainty for each bin as the sum of errors according to PDF reweighting, along with the statistical error, added in quadrature as given in equation 7.7 and following the rules for asymmetric errors given in Table 7.3.

7.1.5 Simulation Results with PDF Reweighting

The procedure for PDF reweighting as describe above was applied to the $Z^0 \rightarrow e^+e^-$ dataset produced for the Rome ATLAS Physics workshop. The particle-level information associated with this 41 000 event sample was passed through the ATLAS Fast Detector simulation program (ATLFAST) from release 10.2.0 of the ATLAS software.

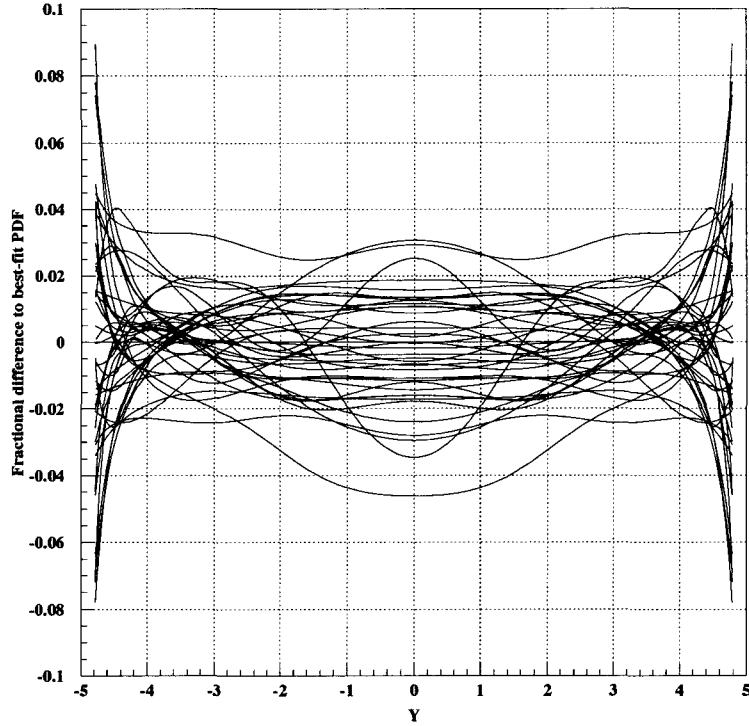


Figure 7.13: Fractional difference of the best-fit CTEQ6.1 PDF set from each eigenvector set uncertainty as a function of Z^0 boson rapidity.

A series of selection criteria were applied to the simulation dataset in order to determine the acceptance for the observation of $Z^0 \rightarrow e^+e^-$. The selection criteria required the reconstruction of two isolated electrons of opposite charge within $|\eta| < 2.5$ and with $p_T(e^\pm) > 20$ GeV/c. The invariant mass of the reconstructed e^+e^- system was further required to be within 6 GeV/c² of the accepted Z^0 mass. With this sample we considered the PDF reweighting technique for two distinct cases.

- Case 1: The set of events are examined without the application of any selection cuts and the PDF reweight terms B_i are calculated.
- Case 2: The set of events are analysed via a series of selection cuts and the corresponding PDF reweight terms C_i for these surviving events are calculated.

Acceptance Shift	Error (positive)	Error (negative)
$\Delta A_1^i > 0, \Delta A_2^i > 0$	$\sqrt{(\Delta A_1^{i2} + \Delta A_2^{i2})}/2$	0
$\Delta A_1^i > 0, \Delta A_2^i < 0$	ΔA_1^i	ΔA_2^i
$\Delta A_1^i < 0, \Delta A_2^i > 0$	ΔA_2^i	ΔA_1^i
$\Delta A_1^i < 0, \Delta A_2^i < 0$	0	$\sqrt{(\Delta A_1^{i2} + \Delta A_2^{i2})}/2$

Table 7.3: Method by which the errors in acceptance uncertainty are calculated for each of the error PDF sets.

It is the ratio of these two values, C_i/B_i , that provides the measure of the uncertainty on the acceptance due to the PDF reweighting and therefore due to the uncertainties in the PDFs themselves. Figure 7.14 shows the calculated values of the PDF weights before (solid triangle) and after (open square) the application of selection cuts to the $Z^0 \rightarrow e^+e^-$ sample. The corresponding ratio of B_i/A_i , where i ranges over the number of PDF error sets of CTEQ6.1, is shown in Figure 7.15. The uncertainty associated with each point is the effective uncertainty as calculated from the bin-by-bin widths of the PDF weight distributions that are represented by each before and after selection cut point of Figure 7.14 summed in quadrature. Since each point represents a different and independent pair of PDF error set members then the corresponding acceptance weights are also independent of each other. Therefore no correlation should be inferred between the spread of the calculated acceptance weights and the magnitude of the acceptance weight uncertainty.

When summing over all the PDF error sets according to the prescription of equation 7.7 and Table 7.3, the overall values for the positive and negative uncertainties on the acceptance due to the PDF error sets were calculated to be

$$\Delta A_+ = 0.64\% \quad (7.8)$$

$$\Delta A_- = 1.10\% \quad (7.9)$$

These values compare well with the results calculated for the inclusive W and Z cross sections as measured at the Tevatron by CDF where the positive and negative errors associated with the CTEQ PDF eigenvector sets for the

$Z \rightarrow e^+e^-$ channel was found to be 0.69% and 0.84%, respectively [46].

It is also worthwhile to examine the percentage uncertainty in the surviving $Z^0 \rightarrow e^+e^-$ sample coming from the PDF error sets incorporated into the reweighting method. Figure 7.16 shows the distribution of the e^+ and e^- pseudorapidities of the selected events along with the statistical uncertainty within each η bin. The percentage uncertainty introduced via the PDF reweighting is shown in Figure 7.17 also as a function of the electron and positron pseudorapidity. Within $|\eta| < 2.5$ nearly all contributions to the error in acceptance are less than 0.5%, with the minimum of 0.25% typically near $|\eta| \approx 0$. It is expected that the corresponding uncertainties in acceptance for the production of W^+ and W^- should also be at this same approximate level. In the future this study will be expanded to include the PDF reweighting for production of W^\pm as well as the decays to muons. This will be greatly aided during the upcoming ATLAS Computing Systems Commissioning (CSC) period in 2006 (previously identified as Data Challenge 3) that will make larger samples of simulated W^\pm and Z^0 events available for analysis.

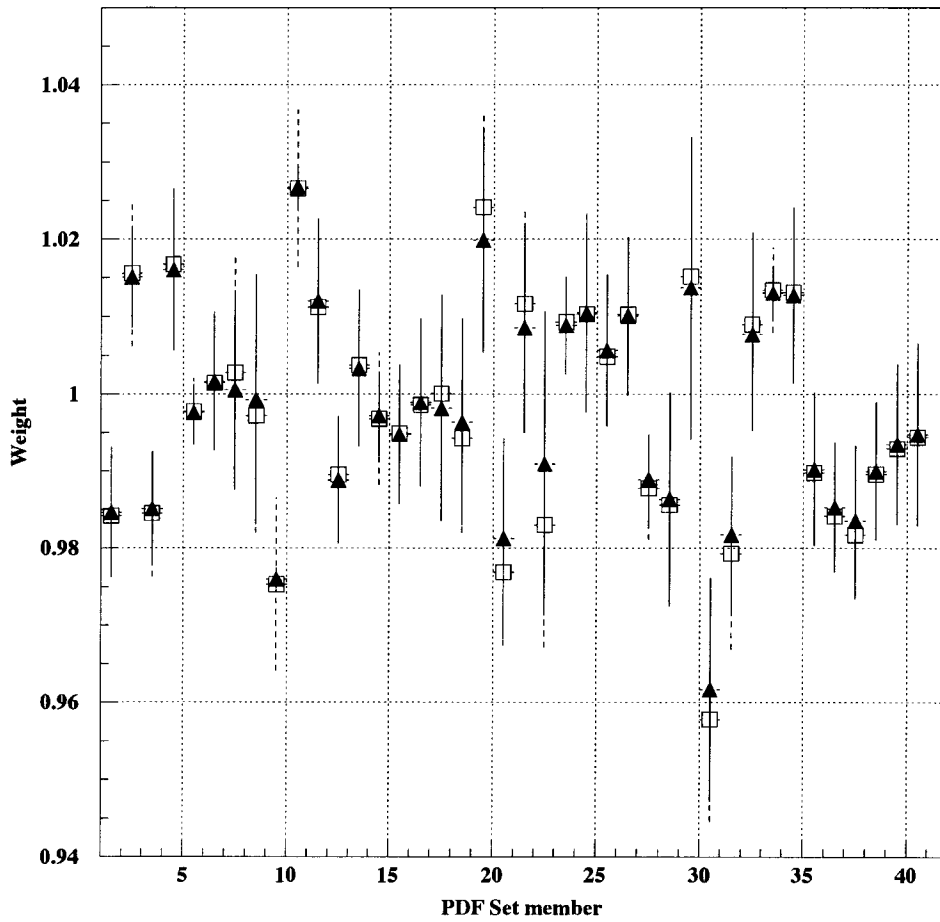


Figure 7.14: Calculated values for the contribution toward the overall PDF weight for each eigenvector set before the application of Z^0 event selection criteria (solid triangle) and after event selection (open square).

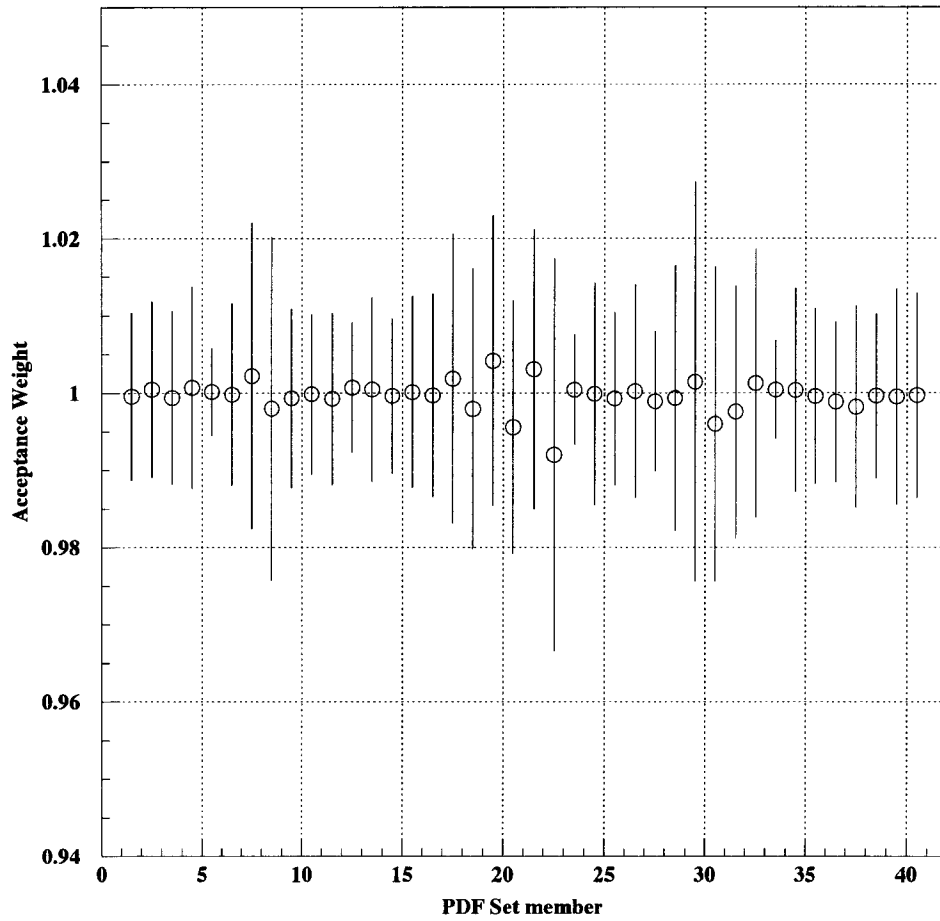


Figure 7.15: Calculated PDF reweighting terms for the acceptance of $Z^0 \rightarrow e^+e^-$ events in ATLAS for each member of the CTEQ6.1 error PDF set.

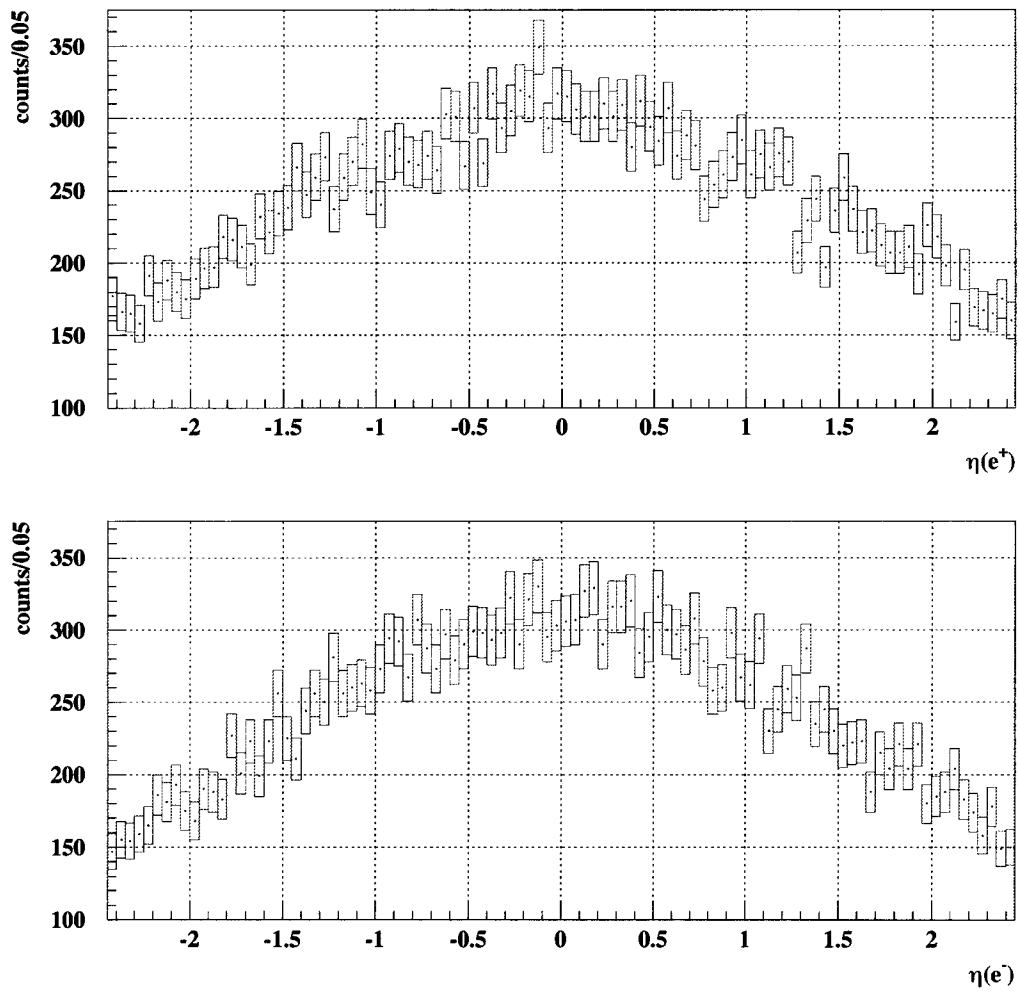


Figure 7.16: Distribution of the ATLAS Rome monte carlo sample of $Z^0 \rightarrow e^+e^-$ as a function of e^+ (top) and e^- (bottom) pseudorapidity. The statistical uncertainty introduced by the limited sample size of the dataset is visible from extent of the error bars.

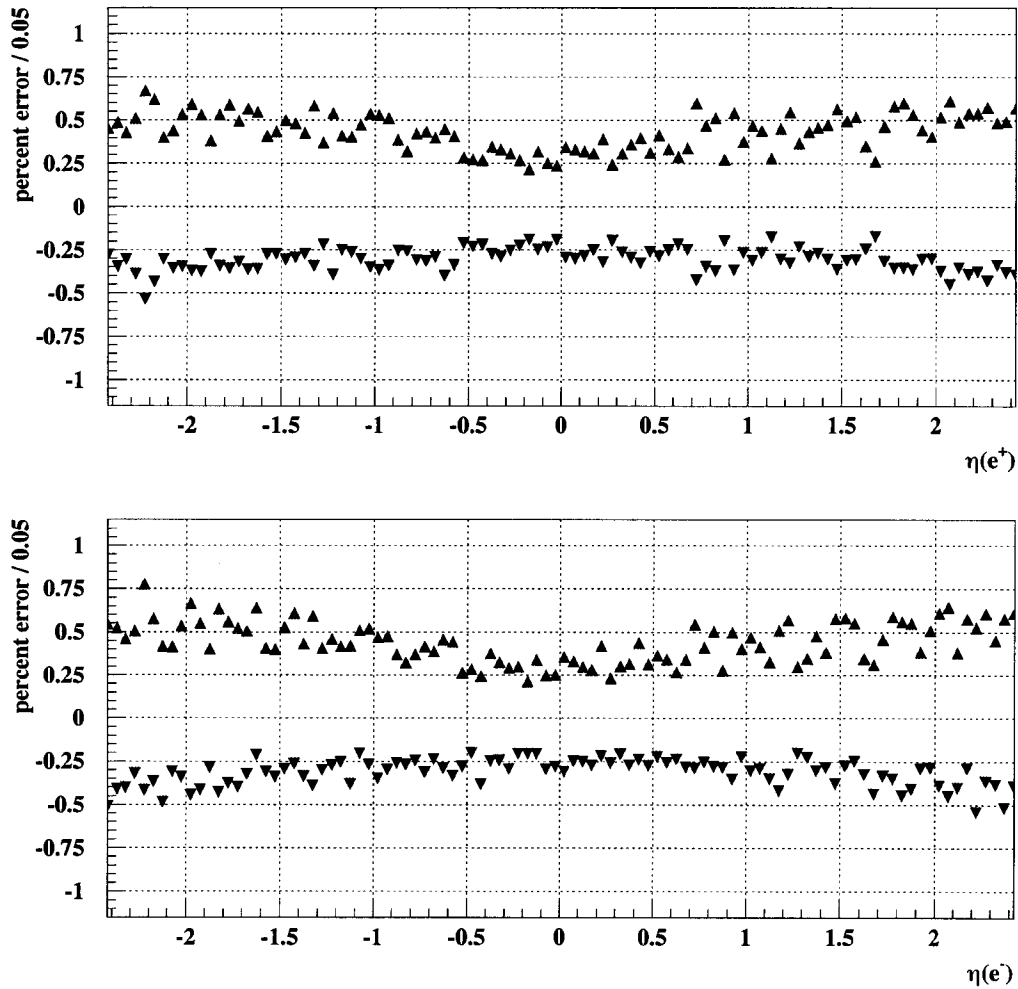


Figure 7.17: Calculated theoretical positive (up triangle) and negative (down triangle) percentage uncertainties due to PDF reweighting for the ATLAS Rome sample of $Z^0 \rightarrow e^+e^-$ as a function of the e^+ (top) and e^- (bottom) pseudorapidity η .

Chapter 8

Conclusion

Two physics processes for luminosity measurement and monitoring at the Large Hadron Collider and the ATLAS experiment have been presented.

The production of $\mu^+\mu^-$ pairs from the collision of virtual two photon exchange arising from the electromagnetic field of the counter-rotating proton beams of the LHC is discussed. Such events from the peripheral collision of the hadron beams are characterized by the near-zero acoplanarity angle and transverse momentum of the produced $\mu^+\mu^-$ system. In addition to selection criteria based upon these kinematic properties the application of vertex fit requirements aid in the rejection of $\mu^+\mu^-$ pairs from background processes of Drell-Yan as well as pile-up. Other backgrounds which cannot be easily differentiated from the signal include semi-inelastic, inelastic and rescattering variations of the two photon interaction. However, by requiring that the p_T of the produced di-lepton system be less than 50 MeV/c² the corrections to the overall cross section from each contribution are at the level of 1% or less when compared to the fully elastic $\gamma\gamma \rightarrow \mu^+\mu^-$ cross section of (0.775 ± 0.008) pb. The theoretical uncertainties associated with the QED process of two photon production of $\mu^+\mu^-$ pairs at the LHC is well understood to high accuracy (less than 1%), and therefore should be well suited as an offline method to measure the luminosity delivered to ATLAS at the level of approximately 2 to 3%.

Currently the Fermilab Tevatron is the highest energy hadron collider in operation and as such represents an ideal environment in which two photon production of lepton pairs via peripheral collisions can be studied prior to the

LHC startup in 2007. Therefore a search has been initiated for the observation of exclusive $\gamma\gamma \rightarrow \mu^+\mu^-$ events at the CDF Run II experiment at the Fermilab Tevatron. A large sample of diffractive physics events, requiring rapidity gaps in both the East and West Beam Shower Counters, was collected at CDF during 2004-5 and formed the basis of a data scan that searched for the presence of exclusive $\mu^+\mu^-$ events. Selection criteria designed for the elimination of background contamination from cosmic ray muons, as well as for $\mu^+\mu^-$ pairs from the decay of the nearby J/ψ peak, were applied along with cuts to the measured acoplanarity angle and transverse momentum of the $\mu^+\mu^-$ system. A series of preliminary candidate events have been identified and extracted from the CDF diffractive data sample. Detailed bin-by-bin comparisons of the data and simulation results were performed for the normalized distributions of acoplanarity angle ϕ , transverse momentum and invariant mass of the $\mu^+\mu^-$ pair. The simulation and recorded data samples were found to be in good agreement providing strong evidence for observation of $\gamma\gamma \rightarrow \mu^+\mu^-$ events at CDF, and the potential first such observation of this process at a hadron collider. Further investigations are required to fully verify these candidate events as coming from the exclusive production of $\mu^+\mu^-$ pairs. Confirmation of the event exclusivity is the next step toward public dissemination and publication of a full set of measurements which will first require blessing by the CDF collaboration. Further studies are also foreseen to extend the analysis so as to include non-exclusive events where the kinematic and vertex fit criteria as described in Chapter 5 for ATLAS can be applied.

To compliment the absolute luminosity measurement capability of the $\gamma\gamma \rightarrow \mu^+\mu^-$ process, the high rate of W and Z production at the LHC was shown to be well suited for the task of online luminosity monitoring. In this capacity the measurement of the W and Z production rates was demonstrated to vary from peak values of 12 and 2.0 Hz (at the beginning of an accelerator fill) down to 2.4 and 0.4 Hz (at the end of the LHC fill when the beams are dumped). The decrease in observed production rate follows according to the exponential decay lifetime of the proton beams τ_{lumi} during nominal operations at low luminosity ($2 \times 10^{33} \text{cm}^{-2}\text{s}^{-1}$).

For an accurate comparison between theoretical predictions and the current Tevatron and future LHC measurements for the production of W and Z , the calculations and simulation studies need to be extended so as to include higher order NLO and NNLO corrections. The results of such recent calculations and simulations including NLO effects have been evaluated and combined with the available CTEQ 6.1 error set to determine an accurate estimate of the PDF uncertainties upon W and Z production at NLO. Over the central rapidity ranges these cross section uncertainties were calculated to be between 5 and 7.5%.

Until recently studies which calculated the effects of PDF uncertainties based upon the PDF error sets were required to generate simulation samples for each of the error set members. In the case of the CTEQ 6.1 PDF error set this represented forty times the original amount of computational processing time and data storage resources required when compared to the single best-fit PDF member alone. PDF reweighting aims to provide a fast and accurate method of calculating the uncertainty of physically measurable quantities without requiring the generation of separate simulation samples for each of the PDF error set members. This is accomplished for all events such that the contributions of the up and down error sets of each PDF eigenvector are summed in quadrature relative to that of the best-fit PDF set member. The PDF reweighting procedure was specifically tested for the case of $Z^0 \rightarrow e^+e^-$ events as simulated for the ATLAS Rome Physics Workshop of 2005. For this event sample the measurable quantity considered was the event acceptance based upon the standard selection criteria for Z production at ATLAS. The resulting uncertainties in the acceptance due to the up (positive) and down (negative) PDF error sets were calculated to be +0.6% and -1.0%, respectively, averaged over the entire pseudorapidity range of acceptance. These results are in agreement with those from a recent study published by CDF for inclusive Z^0 production which analysed a separate simulation data sample for each of the 41 CTEQ6 PDF error set members compared to the single best-fit PDF necessary for the reweighting procedure. The uncertainty in acceptance due to the CTEQ 6.1 PDF errors was also studied in detail as a function of the

experimentally measured pseudorapidity η values of the electron and positron from the Z^0 decay. The percentage error on the acceptance was calculated to vary between 0.25% and 0.50% over the region $|\eta| < 2.5$, thereby indicating that the resulting uncertainty due to the PDF errors is much less than the 5 to 7.5% expected from the pure cross section calculation alone. Therefore, the overall uncertainty in the measured luminosity from the production of W and Z at the LHC is expected to be at the level of 3 to 4%, principally based upon the systematic errors associated with the reconstruction and identification of the decay leptons.

In conclusion, the processes of $\gamma\gamma \rightarrow \mu^+\mu^-$ and W/Z production have respectively been shown to be well suited to the tasks of luminosity measurement and monitoring, respectively, at the LHC. Given the described methods by which experimental backgrounds and theoretical uncertainties are taken into account, these processes will compliment the measurements provided by dedicate luminosity measurement devices to be installed within or around ATLAS.

A subset of the early results for luminosity measurement using two-photon production of $\mu^+\mu^-$ pairs and W/Z production have been published in [56]. Currently a number of internal ATLAS and CDF notes are in preparation by the author and collaborators directly based upon material presented in this thesis, and each of these internal documents are being written with the intention of full publication in refereed journals. The subjects of these notes include the following:

- Exclusive electron pairs in hadron-hadron collisions at CDF,
- Exclusive lepton pairs in hadron-hadron collisions at CDF,
- Luminosity Measurement at the LHC using Two-Photon Production of Lepton Pairs,
- Luminosity Monitoring at the LHC using W/Z Production,
- Studies of PDF Uncertainties upon W and Z Production at the LHC using the PDF Reweighting Method.

All results including simulations and data analysis presented were performed using the computational resources the Particle Physics Computing Centre and the THOR Linux Cluster of the Centre for Subatomic Research, University of Alberta [84]. Additional resources of the LHC Computing Grid [13] were also utilized in the production of the presented results.

Bibliography

- [1] S. L. Glashow. Partial symmetries of weak interactions. *Nucl. Phys.*, 22:579–588, 1961.
- [2] Steven Weinberg. A model of leptons. *Phys. Rev. Lett.*, 19:1264–1266, 1967.
- [3] Jeffrey Goldstone, Abdus Salam, and Steven Weinberg. Broken symmetries. *Phys. Rev.*, 127:965–970, 1962.
- [4] (ed.) Bruning, O. et al. LHC design report. vol. i: The LHC main ring. CERN-2004-003.
- [5] ATLAS inner detector: Technical design report. vol. 1. CERN-LHCC-97-16.
- [6] ATLAS inner detector: Technical design report. vol. 2. CERN-LHCC-97-17.
- [7] M. S. Alam et al. ATLAS pixel detector: Technical design report. CERN-LHCC-98-13.
- [8] ATLAS liquid argon calorimeter: Technical design report. CERN-LHCC-96-41.
- [9] ATLAS tile calorimeter: Technical design report. CERN-LHCC-96-42.
- [10] ATLAS muon spectrometer: Technical design report. CERN-LHCC-97-22.
- [11] ATLAS first-level trigger: Technical design report. CERN-LHCC-98-14.
- [12] ATLAS high-level trigger, data acquisition and controls: Technical design report. CERN-LHCC-2003-022.
- [13] (ed.) Bird, I. et al. LHC computing grid. technical design report. CERN-LHCC-2005-024.
- [14] R. Sturrock et al. A step towards a computing grid for the LHC experiments: ATLAS data challenge 1. CERN-PH-EP-2004-028.
- [15] S. Eidelman et al. Review of particle physics. *Phys. Lett.*, B592:1, 2004.
- [16] ATLAS detector and physics performance. technical design report. vol. 2. CERN-LHCC-99-15.

- [17] ATLAS: Detector and physics performance technical design report. volume 1. CERN-LHCC-99-14.
- [18] K. Potter. Luminosity measurements and calculations. In *Jyvaeskylae 1992, Proceedings, General accelerator physics, vol. 1* 117-129. CERN Geneva - CERN-94-01 (94/01,rec.Mar.) 117-129.
- [19] D. H. Perkins. Introduction to high-energy physics. Reading, USA: Addison-wesley (1982) 437p.
- [20] J. Bossler et al. LHC beam instrumentation: Conceptual design report. CERN-LHC-PROJECT-REPORT-370.
- [21] A. L. Perrot, G. Molinari, and A. Bay. A luminosity monitor for the large hadron collider. *Nucl. Instrum. Meth.*, A487:331–336, 2002.
- [22] D. Acosta et al. The CDF cherenkov luminosity monitor. *Nucl. Instrum. Meth.*, A461:540–544, 2001.
- [23] Chyi-Chang Miao. The D0 run II luminosity monitor. *Nucl. Phys. Proc. Suppl.*, 78:342–347, 1999.
- [24] Maarten Boonekamp. Luminosity measurement in ATLAS. Prepared for 12th International Workshop on Deep Inelastic Scattering (DIS 2004), Strbske Pleso, Slovakia, 14-18 Apr 2004.
- [25] V. M. Budnev, I. F. Ginzburg, G. V. Meledin, and V. G. Serbo. The possibility of applying the process $p p \rightarrow p p e^+ e^-$ for calibration of cross-sections in colliding $p p$ beams. *Phys. Lett.*, B39:526–530, 1972.
- [26] Gerhard Baur, Kai Hencken, Dirk Trautmann, Serguei Sadovsky, and Yuri Kharlov. Coherent gamma gamma and gamma a interactions in very peripheral collisions at relativistic ion colliders. *Phys. Rept.*, 364:359–450, 2002.
- [27] Valery A. Khoze, Alan D. Martin, R. Orava, and M. G. Ryskin. Luminosity monitors at the LHC. *Eur. Phys. J.*, C19:313–322, 2001.
- [28] Robert N. Cahn and J. D. Jackson. Realistic equivalent photon yields in heavy ion collisions. *Phys. Rev.*, D42:3690–3695, 1990.
- [29] Manuel Drees, John R. Ellis, and D. Zeppenfeld. Can one detect an intermediate mass higgs boson in heavy ion collisions? *Phys. Lett.*, B223:454, 1989.
- [30] J. A. M. Vermaseren. Two photon processes at very high-energies. *Nucl. Phys.*, B229:347, 1983.
- [31] S. P. Baranov, O. Duenger, H. Shooshtari, and J. A. M. Vermaseren. Lpair: A generator for lepton pair production. In *Hamburg 1991, Proceedings, Physics at HERA, vol. 3* 1478-1482. (see HIGH ENERGY PHYSICS INDEX 30 (1992) No. 12988).
- [32] K. Hencken, Yu. V. Kharlov, G. V. Khaustov, S. A. Sadovsky, and V. D. Samoylenko. TPHIC, event generator of two photon interactions in heavy ion collisions. IFVE-96-38.

- [33] R. Engel. Photoproduction within the two component dual parton model. 1. amplitudes and cross-sections. *Z. Phys.*, C66:203–214, 1995.
- [34] R. Engel and J. Ranft. Hadronic photon-photon interactions at high energies. *Phys. Rev.*, D54:4244–4262, 1996.
- [35] Maarten Boonekamp and Tibor Kucs. Pomwig v2.0: Updates for double diffraction. *Comput. Phys. Commun.*, 167:217, 2005.
- [36] M. Boonekamp, R. Peschanski, and C. Royon. Popping out the higgs boson off vacuum at Tevatron and LHC. *Nucl. Phys.*, B669:277–305, 2003.
- [37] Torbjorn Sjostrand, Leif Lonnblad, Stephen Mrenna, and Peter Skands. Pythia 6.3: Physics and manual. 2003.
- [38] S. D. Drell and Tung-Mow Yan. Partons and their applications at high energies. *Ann. Phys.*, 66:578, 1971.
- [39] S. Catani et al. QCD. 2000.
- [40] Hepdata the durham hep databases. <http://www-spires.dur.ac.uk/spires/hepdata/>.
- [41] J. Pumplin et al. New generation of parton distributions with uncertainties from global QCD analysis. *JHEP*, 07:012, 2002.
- [42] A. D. Martin, R. G. Roberts, W. J. Stirling, and R. S. Thorne. Uncertainties of predictions from parton distributions. i: Experimental errors. ((t)). *Eur. Phys. J.*, C28:455–473, 2003.
- [43] S. Alekhin. Parton distribution functions from the precise NNLO QCD fit. 2005.
- [44] S. Chekanov et al. An NLO QCD analysis of inclusive cross-section and jet- production data from the ZEUS experiment. *Eur. Phys. J.*, C42:1–16, 2005.
- [45] Amanda M. Cooper-Sarkar. Uncertainties on parton distribution functions from the ZEUS NLO QCD fit to data on deep inelastic scattering. *J. Phys.*, G28:2669–2678, 2002.
- [46] A. Abulencia et al. Measurements of inclusive W and Z cross sections in p anti- p collisions at $s^{**}(1/2) = 1.96\text{-tev}$. 2005.
- [47] S. Chekanov et al. A ZEUS next-to-leading-order QCD analysis of data on deep inelastic scattering. *Phys. Rev.*, D67:012007, 2003.
- [48] Claire Gwenlan, Amanda Cooper-Sarkar, and Christopher Targett-Adams. Impact of future HERA data on the determination of proton parton distribution functions. *J. Phys.*, G32:221–228, 2006.
- [49] G. Corcella et al. Herwig 6: An event generator for hadron emission reactions with interfering gluons (including supersymmetric processes). *JHEP*, 01:010, 2001.
- [50] G. Corcella et al. Herwig 6.5 release note. 2002.

- [51] Stefano Frixione and Bryan R. Webber. The mc@nlo 2.3 event generator. 2004.
- [52] C. Balazs and C. P. Yuan. Soft gluon effects on lepton pairs at hadron colliders. *Phys. Rev.*, D56:5558–5583, 1997.
- [53] Qing-Hong Cao and C. P. Yuan. Combined effect of QCD resummation and QED radiative correction to W boson observables at the Tevatron. *Phys. Rev. Lett.*, 93:042001, 2004.
- [54] Charalampos Anastasiou, Lance J. Dixon, Kirill Melnikov, and Frank Petriello. High-precision QCD at hadron colliders: Electroweak gauge boson rapidity distributions at NNLO. *Phys. Rev.*, D69:094008, 2004.
- [55] M. Biglietti et al. Muon event filter software for the ATLAS experiment at the LHC. ATL-DAQ-CONF-2005-008.
- [56] B. L. Caron and J. L. Pinfold. Experimental aspects of luminosity determination at the LHC: Lepton pair and single gauge boson production. Prepared for 1st Workshop on Forward Physics and Luminosity Determination at LHC, Helsinki, Finland, 31 Oct - 4 Nov 2000.
- [57] A. G. Shamov and Valery I. Telnov. Two-photon lepton pair production for luminosity determination at LHC. Prepared for 1st Workshop on Forward Physics and Luminosity Determination at LHC, Helsinki, Finland, 31 Oct - 4 Nov 2000.
- [58] A. G. Shamov and Valery I. Telnov. Precision luminosity measurement at LHC using two-photon production of $\mu^+ \mu^-$ pairs. *Nucl. Instrum. Meth.*, A494:51–56, 2002.
- [59] Calculations of track parameters and positions. <http://hepunix.rl.ac.uk/atlasuk/simulation/level2/doc/ctrigCVS/>.
- [60] Veikko Karimaki. Fast code to fit circular arcs. HU-SEFT-1991-10.
- [61] Torbjorn Sjostrand. Pythia 5.7 and jetset 7.4: Physics and manual. 1995.
- [62] V. M. Budnev, I. F. Ginzburg, G. V. Meledin, and V. G. Serbo. The two photon particle production mechanism. physical problems. applications. equivalent photon approximation. *Phys. Rept.*, 15:181–281, 1974.
- [63] D. Bocian and K. Piotrkowski. Very forward two-photon $e^+ e^-$ production and luminosity measurement for ion collisions at the LHC. *Acta Phys. Polon.*, B35:2417–2424, 2004.
- [64] D. Mohl, G. Petrucci, L. Thorndahl, and Simon Van Der Meer. Physics and technique of stochastic cooling. *Phys. Rept.*, 58:73–119, 1980.
- [65] R. Blair et al. The CDF-II detector: Technical design report. FERMILAB-PUB-96-390-E.
- [66] CDF web page. <http://www-cdf.fnal.gov/>.
- [67] E. Gerchtein and M. Paulini. CDF detector simulation framework and performance. *ECONF*, C0303241:TUMT005, 2003.

- [68] R. Brun, F. Bruyant, M. Maire, A. C. McPherson, and P. Zancarini. Geant3. CERN-DD/EE/84-1.
- [69] A. Wyatt. A search for exclusive $j/\psi + \gamma$ production. CDF/ANAL/MUON/CDFR/6646.
- [70] A. Wyatt. A search for exclusive $j/\psi + \gamma$ production in data taken with a diffractive j/ψ trigger. CDF/ANAL/MUON/CDFR/7369.
- [71] A. Taffard. Run II cosmic ray tagger. CDF/ANAL/MUON/CDFR/6100.
- [72] A. Hamilton et al. The first observation of exclusive electron pairs in hadron-hadron collisions. CDF/DOC/JET/CDFR/7930.
- [73] The future of forward physics at the LHC. <http://www.fp420.com/conference/dec2005/program.html>.
- [74] L. Poggioli E. Richter-Was, D. Froidevaux. Atfast 2.0 a fast simulation package for ATLAS. ATL-PHYS-98-131.
- [75] ATLAS fast simulation package. <http://www.hep.ucl.ac.uk/atlas/atlfast/>.
- [76] J. Haller and S. Tapprogge. Trigger operation in physics running. ATL-DAQ-INT-2005-001.
- [77] R. K. Ellis, W. James Stirling, and B. R. Webber. QCD and collider physics. *Camb. Monogr. Part. Phys. Nucl. Phys. Cosmol.*, 8:1–435, 1996.
- [78] Vrap software web page. <http://www.slac.stanford.edu/%7Elance/Vrap/>.
- [79] B. Melic, B. Nizic, and K. Passek. A note on the factorization scale independence of the PQCD predictions for exclusive processes. *Eur. Phys. J.*, C36:453–458, 2004.
- [80] S. Frixione and M. L. Mangano. How accurately can we measure the W cross section? *JHEP*, 05:056, 2004.
- [81] J. Pumplin, A. Belyaev, J. Huston, D. Stump, and W. K. Tung. Parton distributions and the strong coupling: Cteq6ab pdfs. 2005.
- [82] Alessandro Tricoli, Amanda M. Cooper-Sarkar, and Claire Gwenlan. Uncertainties on W and Z production at the LHC. 2005.
- [83] M. R. Whalley, D. Bourilkov, and R. C. Group. The les houches accord pdfs (lhpdf) and lhaglu. 2005.
- [84] CSR research computing website. <http://csr.phys.ualberta.ca/twiki/>.